

COMPLEX EOCENE-OLIGOCENE HYPABYSSAL INTRUSIVE SYSTEMS
ASSOCIATED WITH BASALTIC PHREATOMAGMATIC VENTS IN THE AREA EAST OF
PEÑA MOUNTAIN, BIG BEND NATIONAL PARK, WEST TEXAS

by

JENNIFER ANNE HILL

Bachelor of Science, 2011
Texas Christian University
Fort Worth, Texas

Submitted to the Graduate Faculty of the
College of Science and Engineering
Texas Christian University
In partial fulfillment of the requirements
for the degree of

MASTER OF SCIENCE IN GEOLOGY

August 2014

Acknowledgements

A project of this magnitude involves contributions from a great many people, all of whom I deeply appreciate. Of these people, a number must be mentioned here.

The biggest thank you goes to all of the teachers throughout my overlarge academic career. Everything my extreme curiosity reached for, you made attainable.

Dr. Richard Hanson was an invaluable thesis advisor and provided endless guidance and enthusiasm for a subject unknown to me 3 years ago. In the last two months of this thesis, he devoted large spans of time to this project, despite his overbooked schedule. His dry humor and interest in the birds and flowers of Big Bend provided welcome breaks on long field days.

And an especially large thank you to an especially lovely person- Dena, Dr. Hanson's wife.

Dr. Art Busbey helped me innumerable times with computer dilemmas and is the epitome of a Mac Guru. I will always miss (and vainly attempt to recreate) his eclectic taste in music and radio shows. He was also half of the best committee I could imagine.

Dr. Rhiannon Mayne was always willing to talk with me about anything, including bizarre solar-powered desk figures, and was instrumental in maintaining my positivity. She was also the other half of the best committee I could imagine.

Big Bend National Park allowed access and sample collection (with a research permit, of course), which made this study possible. Also, thank you to Roy Pitcock, who allowed the use of his Star House during field trips.

Urban Oil & Gas Group and the people there renewed my interest in all branches of geology and were willing to take on an intern who knew nothing about petroleum. Thank you for a truly phenomenal internship and for encouraging me to make graduating my number one priority.

Professor Milt Enderlin provided timely help and advice in the rock prep room, which saved me hours of irritation and wasted effort. You are truly the best man to call when anything mechanical goes awry.

Nathan Shea spent a shocking amount of time doing battle with software on my behalf, for which I am extremely grateful. Without the combined efforts of Dr. Art Busbey and Nathan Shea, I would have had to drive 160 miles on a regular basis to get to a drafting computer.

My friends and fellow students have my endless thanks because each and every one of them contributed to keeping my sanity intact: René, Amy (E.), Sarah (G.), Katelyn, Sarah (A.), Clark, Terri, Maryam, Ashley, Amy (W.), Peyton, Garrett, and many many others.

My ex-students gave me something to smile about and something to look forward to every day.

And last, but very definitely not least, my parents and other family members deserve a plethora of thanks. My parents put up with me, encouraged me, and provided indispensable support throughout this long process, and my family dealt with me avoiding get-togethers, and provided endless encouragement.

Table of Contents

Acknowledgements.....	ii
List of Figures.....	vi
List of Tables.....	xiii
Chapter 1: Introduction.....	1
Statement of Problem.....	1
Research Methods and Analytical Techniques.....	4
Field Mapping.....	4
Petrographic Analysis.....	4
Geochemical Analysis.....	5
Geochronology.....	6
Background to Phreatomagmatism.....	6
Chapter 2: Regional Geologic Setting.....	12
Geologic Setting.....	12
Marathon Orogeny.....	14
Breakup of Pangea.....	14
Laramide Orogeny and Arc-Related Magmatism.....	15
Transitional Tectonics.....	18
Basin and Range Faulting.....	20
Quaternary Erosion.....	21
Eocene Basaltic Phreatomagmatism within and near Big Bend National Park.....	22
Newly Discovered Eocene Phreatomagmatic Sites.....	27
Northwest of Tule Mountain.....	27
Dogie Mountain Dike.....	30
East of Peña Mountain.....	32
Black Peaks.....	32
East of Study Butte.....	34
Selecting a Study Area.....	36

Chapter 3: Geologic Setting of the Study Area	37
Stratigraphy.....	39
Aguja Formation.....	39
Javelina Formation.....	40
Black Peaks Formation	40
Chisos Formation	40
Chisos Formation Lava Members.....	41
Faults.....	42
Chapter 4: Basalt Lava, Phreatomagmatic Vents, and Hypabyssal Intrusions East of Peña Mountain.....	46
Introduction.....	46
Alamo Creek Basalt Lava	46
Phreatomagmatic Vents	61
Hypabyssal Intrusions.....	85
Type I.....	85
Type II.....	91
Type III	96
Chapter 5: Geochemistry and Geochronology.....	107
Introduction.....	107
Major Elements.....	110
Trace Elements.....	122
Normalized Multi-Element and REE Diagrams	122
Trace-Element Discrimination Diagrams	126
Geochemical Conclusions.....	133
Geochronology.....	133
Chapter 6: Conclusions.....	139

Appendix I	143
⁴⁰ Ar/ ³⁹ Ar Dating Techniques	143
⁴⁰ Ar/ ³⁹ Ar Data Tables	145
References.....	149

VITA

ABSTRACT

List of Figures

Figure 1. Setting of the study area within Big Bend National Park and the Trans-Pecos Magmatic Province. Figure modified from Befus et al. (2009).....	3
Figure 2. Diagram of a maar volcano, modified from Befus et al. (2009).	10
Figure 3. Traditional model of a maar, diatreme, and feeder dike, modified from Lorenz (2003).	11
Figure 4. Stratigraphic column showing major formations and large-scale tectonic episodes in the Big Bend region. Modified from Page et al. (2008).	13
Figure 5. Eocene basaltic phreatomagmatic vents in the Big Bend region. A- Northwest of Tule Mountain; B- Doggie Mountain dike; C- East of Peña Mountain; D- Black Peaks; E- East of Study Butte. Modified from a figure drafted by K. Befus.	25
Figure 6. Model for Study Butte magma plumbing system, modified from a diagram drafted by R. Hanson.	26
Figure 7. Pebble in vent fill. Pen for scale.	29
Figure 8. Billows on dike margin, with baked sediment still attached in places. Blue pencil for scale.	31
Figure 9. View of all three of the Black Peaks.	33
Figure 10. Fissure vent in dike-sill complex near Study Butte. Photo from R. Hanson.	35
Figure 11. Geologic context of study area. Mapping outside of study area is adapted from Turner et al. (2011).	38
Figure 12. Fault juxtaposing Alamo Creek Basalt on left with Chisos strata on right. Author for scale. View looking north at point 3 in Plate I.	44
Figure 13. Fault juxtaposing Chisos strata on left with Alamo Creek Basalt and Black Peaks strata on right. Hammers for scale, at base of outcrop against white Chisos strata.	45
Figure 14. Thickest part of northern Alamo Creek Basalt outcrop. Top part of this outcrop shows heavy spheroidal weathering; lower part of outcrops shows undulatory columnar jointing. Walking stick for scale.	51
Figure 15. Photomicrograph of thin section from northern Alamo Creek Basalt in plane light (left) and crossed polars (right). Vertical dimension is 5 mm. Note altered olivine between plagioclase microlites in left view. Ophitic titanite has pale purple color in left view and bright interference colors in right view.	52

- Figure 16. View of Alamo Creek Basalt filling paleochannel (blue arrows) with Black Peaks strata forming the paleochannel margin (arrowed) in foreground. Chisos conglomeratic sandstone (purple arrow) overlies Alamo Creek Basalt, and Type III diabase is present at top of the hill. For scale, plant to right of paleochannel is ~ 1 m wide. Image from point 6 in Plate I. 53
- Figure 17. Alamo Creek Basalt in the southern outcrop, filling a paleochannel. Basalt outcrop at the base of the hill on the left (blue arrow on left) and structurally higher basalt (blue arrow on right) overlying redish-purple Black Peaks strata (purple arrow). View looking north-northeast; arrowed plant is ~ 0.5 m across. Image of point 7 in Plate I..... 54
- Figure 18. Flow breccia at base of northern outcrop of Alamo Creek Basalt (overprinted by spheroidal weathering). Note baked margin of underlying Chisos mudstone in first few centimeters below contact. Hammer for scale (arrowed), against white Chisos strata at base of outcrop..... 55
- Figure 19. Peperite at base of northern outcrop of Alamo Creek Basalt. Sediment mixed with basalt is light yellow in color. Pencils for scale..... 56
- Figure 20. Chisos conglomeratic sandstone (yellow) overlying and filling cracks within flow breccia at the upper margin of the northern outcrop of Alamo Creek Basalt. Pencil for scale. 57
- Figure 21. View of part of spiracle within southern outcrop of Alamo Creek Basalt. Basalt clasts are mixed with lighter colored sediment. Chocolate-brown chalcedony is arrowed. Pencil for scale. 58
- Figure 22. Alamo Creek Basalt outcrop just south of the study area. Note undulatory columnar jointing of basalt. Silver and red walking stick for scale at base of foremost outcrop..... 59
- Figure 23. Photomicrograph of thin section from southern outcrop of Alamo Creek Basalt in plane light and crossed polars. Note lack of alteration seen in Figure 14. Ophitic titanite has pale purple color in left view and bright interference colors in right view. 60
- Figure 24. Vent-fill material with light colored sediment matrix. Note range in vesicularity and fluidal contacts between basalt clasts and sediment matrix. Image from outcrop C in Plate I. Pencil for scale..... 64
- Figure 25. Close up view of sample in Figure 24. Note small basalt clasts in sediment matrix. Image from outcrop C on Plate I. Pencil for scale..... 65

- Figure 26. Photomicrograph showing typical vent-fill material, with basalt clasts of varying vesicularity and grain size, mixed with sediment. Basalt (small blue circles) and sediment (larger purple circles) are identified for reference only in this photomicrograph. Sample from outcrop B on Plate I. Plane light; field of view is 22 mm across. 66
- Figure 27. Slab of vent fill. Note cream-colored chunks of tuffaceous material in contrast to pale grey chunks of mud. Also note fluidal margins and range in vesicularity of basalt clasts. Sample from outcrop B in Plate I. 67
- Figure 28. Photomicrograph showing fluid contacts between basalt and sediment. Note sediment filling vesicles in basalt clasts. Sample from outcrop E in Plate I. Plane light; field of view is 22 mm across. 68
- Figure 29. Photomicrograph showing sediment filling vesicles within and space between basalt clasts. Sediment is very fine-grained and is fragmented, possibly due to contraction during cooling and dewatering. Sample from outcrop D in Plate I. Plane light; field of view is 22 mm across. 69
- Figure 30. Slab of vent fill with basalt pyroclasts showing a range in vesicularity. Also note mud with contraction cracks in upper right portion of slab. Sample from outcrop B in Plate I. ... 70
- Figure 31. Range in vesicularity of basalt pyroclasts in vent-fill outcrop. Also note small size of some basalt clasts. Image from outcrop B in Plate I. Pencil for scale. 71
- Figure 32. Photomicrograph showing tachylite clasts (blue arrows) with a high degree of vesicularity within vent fill. Sample from outcrop B in Plate I. Plane light; view is 22 mm across. 72
- Figure 33. Angular clasts of basalt in vent-fill sample. Note range in vesicularity of basalt clasts. Image from outcrop E in Plate I. Pencil for scale. 73
- Figure 34. Jigsaw texture of basalt clast fragments (examples are arrowed). Also note lapillized basalt clast with high vesicularity. Image from outcrop G in Plate I. Pencil for scale. 74
- Figure 35. Photomicrograph showing armored (blue arrow) and accretionary ash-sized particles (purple arrow). Sample is from outcrop B in Plate I. Plane light; view is 22 mm across. 75
- Figure 36. Large basaltic bomb within vent-fill outcrop D. Carbonate-filled amygdules are visible in bomb. Less altered portions of this bomb were taken for geochemical sample JH-27. Pencil for scale. 76

- Figure 37. Slab of vent fill showing darker chilled margin (arrowed) of basaltic pyroclast in center of slab. Sample from outcrop B in Plate I..... 77
- Figure 38. Darker, fluidal outlines of grey basalt spatter within pale yellow sediment in vent fill. Image from outcrop G in Plate I. Pencil for scale. 78
- Figure 39. Photomicrograph showing indistinct margins between spatter pieces in mass of agglutinate. Blue arrow points to one margin, which is defined by tan sediment trapped between spatter pieces. Sample from outcrop D in Plate I. Plane light; field of view is 22 mm across. 79
- Figure 40. Basalt-rich debris jet in vent-fill outcrop D. Note fluidal shapes of many of the clasts. Image from outcrop D in Plate I. Pencil for scale. 80
- Figure 41. Agglutinate sample from basalt-rich debris jet. Different clasts are best distinguished by areas of different vesicularities. Sample from outcrop D in Plate I..... 81
- Figure 42. Sediment-rich debris jet in vent-fill outcrop D. Pencil for scale. Note bomb at tip of pencil..... 82
- Figure 43. Hand sample from sediment-rich debris jet. Note similarity to other vent-fill samples. Sample from outcrop D in Plate I. 83
- Figure 44. Contact (arrowed) between basalt-rich debris jet at base of outcrop (behind pencil) and sediment-rich debris jet at top of picture. Note irregular contact between the two jets, with protrusion of sediment-rich material into basalt-rich material. Image from outcrop D in Plate I. Pencil for scale. 84
- Figure 45. View of entire hypabyssal intrusive complex looking west-southwest from point 9 on Plate I. Note pale grey and white of Chisos strata surrounding dark brown diabase intrusions. Left arrow points to southernmost Type III exposure; right arrow points to northernmost Type III exposure. Santa Elena Canyon on horizon in center of image, with Peña Mountain in background on right side of image..... 87
- Figure 46. Photomicrographs of thin section from main Type I intrusion in plane light (left) and crossed polars (right). Vertical dimension is 5 mm. Note purple color of titanite in plane light and lack of any large phenocrysts. 88
- Figure 47. View looking down on billowed surface of Type I intrusive diabase exposed by erosion in base of stream channel. Note tan color of chilled margin. Host redish gray Black Peaks mudstone covers chilled margin of Type I in bottom right of view. Pencils for scale.89

- Figure 48. Vent fill material (outcrop D) at top of tower-like outcrop with Type I intrusion forming base of structure. Pen (blue and silver) for scale in location of Type I geochemical sample (JH-62)..... 90
- Figure 49. Contact between Type II intrusion (above) and Type III, which shows a distinct chilled margin against Type II. Note redish hue and peperite (to left of hammer and within arrows; pale yellow sediment mixed with basalt clasts) along margin of Type II. Hammer for scale. 93
- Figure 50. Photomicrographs of thin section from Type II intrusion in plane light (left) and crossed polars (right). Vertical dimension is 22 mm. Note large size of plagioclase phenocrysts in significantly wider view than other photomicrographs. Groundmass shows intergranular texture. Darker phenocrysts in left image are altered olivine. 94
- Figure 51. Another view of redish Type II contact with Type III. Note chilled margin of Type III against Type II. Hammer for scale. 95
- Figure 52. Billowed contact between dark brown Type III diabase and overlying pale grey and white Chisos strata. Type III is also in foreground, although with a different weathering pattern. Arrowed plant is ~ 0.5 m across. 98
- Figure 53. Contact between dark brown Type III intrusion and overlying pale gray-to-white Chisos mudstone. Note pipe vesicles filled with carbonate. Pen and hammer for scale. 99
- Figure 54. Photomicrographs of thin section from Type III intrusion in plane light (left) and crossed polars (right). Vertical dimension is 5 mm. Note plagioclase phenocryst is not as large as Type II phenocrysts, but low percentage. Olivine in groundmass and a few phenocrysts have been extensively altered to iddingsite (orange)..... 100
- Figure 55. Photomicrograph of thin section of Type III diabase in plane light. View is 5 mm wide. Note size and percentage of plagioclase phenocrysts and altered olivine phenocryst (arrowed)..... 101
- Figure 56. Billowed contact of Type III intrusion with Chisos strata. Note columns formed in baked Chisos mudstone at contact. Pencils for scale. Pencil on left rests on upper margin of baked Chisos mudstone where Type III has been eroded away. 102
- Figure 57. Irregular Type III intrusive rock within Chisos strata. Arrowed dike is ~ 0.5 m wide. 103

Figure 58. Highly irregular Type III intrusive sheet within Chisos strata. Margins are billowed with tan color on outermost chilled edge of Type III material. Hammer for scale (arrowed).	104
Figure 59. Cross-section of Type III sheet in previous figure. Note chilled margin, seen in thin section in next figure. Pencil for scale.....	105
Figure 60. Photomicrograph of chilled margin of Type III intrusion in previous figure, showing altered palagonite which still preserves orange tint. Note plagioclase phenocryst characteristic of Type III and slight increase in microlite size moving downward from chilled margin. Plane light; field of view is 5 mm across.	106
Figure 61. Legend for all geochemical diagrams. See text for sources of other data sets.	111
Figure 62. Igneous spectrum diagram of Hughes (1973).	112
Figure 63. Total alkalis versus silica diagram of LeBas et al. (1986).	113
Figure 64. Harker diagram for TiO_2	114
Figure 65. Harker diagram for Al_2O_3	115
Figure 66. Harker diagram for FeO	116
Figure 67. Harker diagram for MgO	117
Figure 68. Harker diagram for CaO	118
Figure 69. Harker diagram for Na_2O	119
Figure 70. Harker diagram for K_2O	120
Figure 71. Harker diagram for P_2O_5	121
Figure 72. Multi-element diagram for study area samples with fields of comparison data; normalization values from Sun and McDonough (1989). Green field is Alamo Creek Basalt data, red is Ash Spring Basalt, grey is Bee Mountain Basalt.	124
Figure 73. REE diagram for study area samples with fields of comparison data; normalization values from Sun and McDonough (1989). Green field is Alamo Creek Basalt data, red is Ash Spring Basalt, grey is Bee Mountain Basalt.....	125
Figure 74. Discrimination diagram of Winchester and Floyd (1977).....	127
Figure 75. Zr-Ti-Y discrimination diagram of Pearce and Cann (1973).	128
Figure 76. Zr/Y versus Zr discrimination diagram of Pearce and Norry (1979).	129
Figure 77. Zr/4-Nb*2-Y discrimination diagram of Meschede (1986).	130
Figure 78. Ti/Y vs Nb/Y discrimination diagram of Pearce (1982).	131

Figure 79. Nb/Y versus $Zr(P_2O_5 \cdot 10^4)$ discrimination diagram of Floyd and Winchester (1975).	132
Figure 80. $^{40}Ar/^{39}Ar$ age spectra for one plagioclase (purple lines) and three groundmass concentrates for sample JH-54. Cited errors for dates indicated are $\pm 2\sigma$	135
Figure 81. $^{40}Ar/^{39}Ar$ age spectra for three groundmass concentrates for sample JH-55. Cited errors for dates indicated are $\pm 2\sigma$	136
Figure 82. $^{40}Ar/^{39}Ar$ age spectra for one plagioclase (green lines) and two groundmass concentrates for sample JH-58. Cited errors for dates indicated are $\pm 2\sigma$	137
Figure 83. $^{40}Ar/^{39}Ar$ age spectra for three groundmass concentrates for sample JH-62. Cited errors for dates indicated are $\pm 2\sigma$	138
Plate I. Geologic map of area east of Peña Mountain	Inside Cover

List of Tables

Table. 1. Geochemical Data.....	109
Table. 2: $^{40}\text{Ar}/^{39}\text{Ar}$ incremental heating data for sample JH-54	145
Table. 3: $^{40}\text{Ar}/^{39}\text{Ar}$ incremental heating data for sample JH-55	146
Table. 4: $^{40}\text{Ar}/^{39}\text{Ar}$ incremental heating data for sample JH-58	147
Table. 5: $^{40}\text{Ar}/^{39}\text{Ar}$ incremental heating data for sample JH-62	148

Chapter 1: Introduction

Statement of Problem

The Trans-Pecos Magmatic Province in west Texas is a classic area of Cenozoic arc and Basin and Range magmatism. Recent work at TCU has revealed evidence for a previously unknown episode of Eocene phreatomagmatic basaltic volcanism within the province, inside and adjacent to Big Bend National Park (Befus et al., 2009; Winkler et al., 2009; Deitz et al., 2010; Hill et al., 2012). The work done thus far indicates the presence of a series of small basaltic vents exposed at a variety of levels, ranging from near the paleosurface to deeper into the magma plumbing system. These deeper exposures, unveiled by the dramatic topography of Big Bend, display the networks of hypabyssal intrusions which once fed the volcanic vents. The vents were created by explosive subsurface eruptions when basaltic magma came into contact with groundwater-rich sediment. Despite being the second most common volcano type on land (Wohletz and Heiken, 1992), the majority of the work on small phreatomagmatic volcanoes has been in modern environments, where only shallow levels of the system are available for study (e.g., Lorenz, 1986; Németh and White, 2003; White and Ross, 2011). My preliminary fieldwork in Big Bend has confirmed the opportunity to study the magma plumbing system in close proximity to the lower zones of the vents.

An area ~1.7 km by ~0.6 km was chosen for this study. It is in the western part of Big Bend National Park, just east of Peña Mountain (Fig. 1). This location was chosen for its complex network of hypabyssal intrusions which are associated with phreatomagmatic vent-fill material. This study area was first identified by Dr. Dan Miggins, formerly with the USGS and now at Oregon State University. He first recognized the possibility of phreatomagmatic vents in this and other areas in the park, and this was confirmed by mapping for this project.

The project has two main goals: 1) develop a coherent picture of the magma plumbing systems for the phreatomagmatic vents and how they interacted with the vent material during and after eruption processes; and 2) determine how the phreatomagmatic systems relate to local basaltic lavas. The more focused objectives of this project are as follows: a) map out the geometry of the magma plumbing systems, b) document outcrops showing magma billows and peperite as potential precursors to phreatomagmatic activity, and c) determine whether initial phreatomagmatic activity was an important factor in the eruption of basaltic lava flows of similar age in the region.

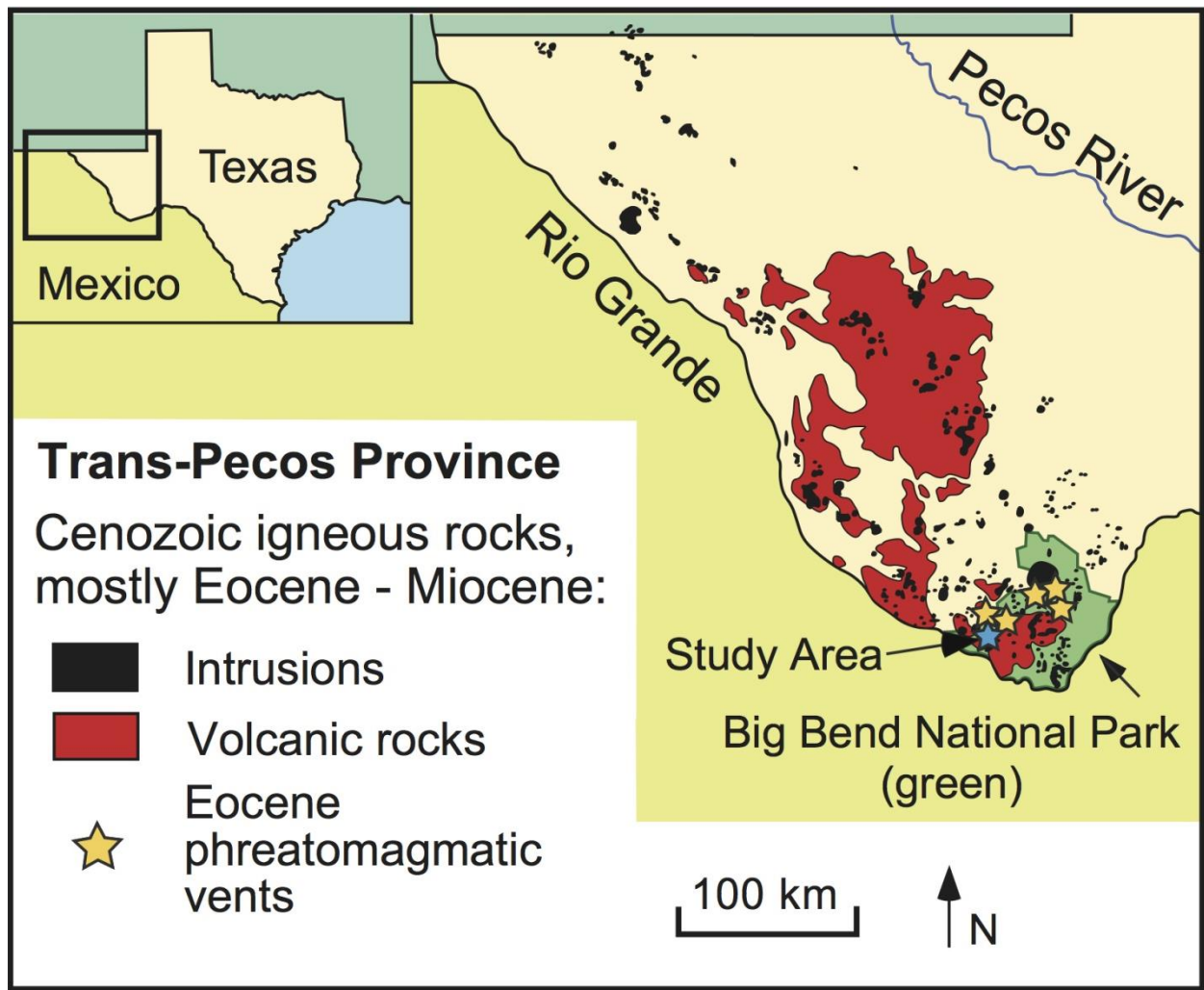


Figure 1. Setting of the study area within Big Bend National Park and the Trans-Pecos Magmatic Province. Figure modified from Befus et al. (2009).

Research Methods and Analytical Techniques

Field Mapping

The entire continuous outcrop of intrusive units and a large portion of local basaltic lava in the area east of Peña Mountain were mapped at a scale of 1:4,000. This was accomplished by taking Google Earth images into the field and mapping directly onto them. The area was covered in detail on foot during this process, and point locations were always located on the satellite images, although GPS coordinates were also taken at most points. Samples were taken throughout the study area, always in conjunction with GPS coordinates. Three distinct intrusive units and two outcrops lavas were identified in the field by a combination of field relations and phenocryst content. Hand samples, geochemical samples, and thin-section samples were acquired for each igneous unit identified in the field. Bedding attitudes were measured on host sedimentary units in select locations.

Petrographic Analysis

Fifty-three thin-section chips were prepared in the TCU rock preparation laboratory, then shipped to Spectrum Petrographics in Vancouver, Washington to be made into thin sections. Thin sections were made of each of the igneous units to corroborate hand-sample identification. With this in mind, thin-section observations of phenocryst percentages have been merged with hand-sample accounts of phenocryst populations to create profiles for each of the main units. Thin sections of each geochemical sample have also been examined for alteration to determine whether sample compositions have been affected by secondary processes. Vent-fill samples were also cut into slabs and thin sections for the dual purpose of comparing basalt in the vent fill to intrusions and lava found in the study area, and to study the phreatomagmatic interactions in

detail. Although all thin sections and slabs were studied, only the most representative or illustrative vent-fill samples are shown in this thesis.

Geochemical Analysis

Eleven bulk-rock samples were collected in the field for geochemical analysis. Each sample was broken into manageable pieces with a crack hammer, then run through a large steel jaw crusher. Afterward, an extra steel plate was inserted behind the removable crushing plate and the samples were run through the large jaw crusher a second time to produce chips ~ 1 cm or less across. Before each sample and between different runs, the jaw crusher was thoroughly cleaned, then pre-contaminated with a small amount of the sample to be processed and cleaned again. Between each of the crushing steps, each sample was rinsed thoroughly and dried, and weathered fragments and any amygdules were separated out by hand.

The processed samples were split into thoroughly homogenized portions of ~ 120 g by repeated use of the cone-and-quarter technique to produce these statistically representative samples. The samples were sent to the GeoAnalytical Laboratory at Washington State University, where they were pulverized into a fine powder with a tungsten carbide swing mill, and 3.5 g of the powder were taken for analysis. The samples were analyzed for major elements and some trace elements (Ni, Cr, V, Ga, Cu, Zn) using x-ray fluorescence (XRF). Details on the XRF procedure, precision, and accuracy may be found at: http://soe.wsu.edu/facilities/geolab/technotes/xrf_method.html. The remaining trace elements (La, Ce, Pr, Nd, Sm, Eu, Gd, Tb, Dy, Ho, Er, Tm, Yb, Lu, Ba, Th, Nb, Y, Hf, Ta, U, Pb, Rb, Cs, Sr, Sc, Zr) were measured with inductively coupled plasma-mass spectrometry (ICP-MS). Refer to http://soe.wsu.edu/facilities/geolab/technotes/icp-ms_method.html for information on sample preparation, precision, and accuracy of the ICP-MS analyses.

Geochronology

Four bulk-rock samples were taken in the field for $^{40}\text{Ar}/^{39}\text{Ar}$ dating of plagioclase phenocryst separates and groundmass concentrates. The samples were initially prepared in the same method as used for the geochemical samples. This work was done at the Oregon State University Argon Geochronology Laboratory by Dr. Dan Miggins and other laboratory workers.

See Appendix I for discussion of $^{40}\text{Ar}/^{39}\text{Ar}$ dating methods by Dr. Dan Miggins.

Background to Phreatomagmatism

A phreatomagmatic eruption is defined as an explosive volcanic eruption which is caused by the interaction between magma and external water, either groundwater or surface water (Cas and Wright, 1987; Lorenz, 1987; Wohletz and Heiken, 1992). In the study area for this thesis, groundwater is the most plausible source of the external water, and thus this type of phreatomagmatism will be the focus here. Commonly this type of interaction occurs when magma intrudes upward into a zone of sediment containing groundwater. If there is an overabundance of groundwater, the magma will quench against the water-rich sediment and undergo little or no explosive behavior. On the other hand, if there is very little groundwater compared to magma, the water is quickly converted into steam and a purely magma-driven eruption proceeds. However, when the water/magma mass ratio reaches a certain proportion (Sheridan and Wohletz, 1981; Wohletz and Sheridan, 1983), explosive phreatomagmatic activity occurs. Phreatomagmatism can develop with any magma composition (Cas and Wright, 1987; Lorenz, 1987), but we will focus on basaltic eruptions since the present study area involves only rocks of this composition. Although there are several types of phreatomagmatic volcanoes, maars (Fig. 2) are the type found in the study area and will therefore be the only type discussed here.

When magma initially intrudes into the groundwater-rich sediment, the heat from the magma vaporizes some of the water, which causes expansion of the water, creating a "steam-film" between the magma and water (Wohletz and Heiken, 1992). The expansion caused by this "steam-film" allows more water-magma interaction, which in turn creates more vaporization of water and more expansion (Cas and Wright, 1987). The cycle continues until enough pressure is generated by the expanding steam to overcome the downward pressure of the overburden, and the overlying sediment is blasted out, forming a small crater. This may lead to the formation of a characteristic type of phreatomagmatic volcano termed a maar. The initial explosions relieve pressure on the underlying material, allowing more wet sediment to mix with hot magma and create steam explosions at lower and lower depths, propagating the explosive level downward (Lorenz, 1986). Frequently, the release of pressure will allow dissolved volatiles in the magma to coalesce into bubbles, adding a magmatic explosive component to the ongoing steam explosions.

After the initial crater is created, the explosive activity continues deepening the crater, which is now called a diatreme (Lorenz, 1986). The material within the diatreme, a chaotic mixture of liquid water, steam, sediment, and magma, is tossed about by the steam and magmatic explosions, and is therefore commonly termed a phreatomagmatic slurry (Ross and White, 2012). As the crater is excavated, material from the slurry is ejected into the air, where it cools and some portion of the steam condenses and falls back into the crater, renewing the water supply. In some cases, a deeper level may experience enough steam expansion and/or volatile release to cause a portion of the phreatomagmatic material to jet upward into the vent fill, a phenomenon known as a "debris jet" (McClintock and White, 2006; Ross and White, 2006; Valentine and White, 2012). Eventually, the crater deepens enough to destabilize the rim, causing blocks of the crater rim to slump into the diatreme itself, and the crater is widened. In

some cases, heat from the magma is depleted before the groundwater is used up, causing explosivity to cease, leaving a wet mass of material in the diatreme. In other cases, the water supply is depleted before the magmatic heat is expended, leaving some amount of magma to continue to rise up. Thus, it is not uncommon to see tongues of magma intruded into vent-fill deposits. If there is enough magma left when explosive phreatomagmatism ceases, lava may pond in the crater or be extruded from it. In some cases, the explosive phreatomagmatism may give way to emplacement of larger scale basaltic lava fields (Hanson and Elliot, 1996; McClintock and White, 2006).

In order for the diatreme to deepen, material must be ejected, thereby creating characteristic maar rim deposits. When the magma is tossed about in the roiling phreatomagmatic slurry, smaller blobs of magma may quench against the water, forming a basaltic glass called sideromelane. These glassy pyroclasts are commonly shattered into angular shards and blocky remnants. The basalt globs that are not as rapidly quenched may have time for exsolution of dissolved volatiles, resulting in pyroclasts with varying degrees of vesicularity (Ross and White, 2012). In some cases, rapid growth of these vesicles causes the blob to shatter, creating pyroclasts with edges defined by broken bubble walls. Some of the basalt magma may also be ripped apart to form fluidal pyroclasts, which may be thrown up onto the rim of the maar to create spatter or basaltic bombs. If enough spatter is ejected onto the crater rim, agglutinate may form. Sediment may be present in various quantities throughout all of these types of deposits (Wohletz and Sheridan, 1983; White, 1996; Wohletz, 2002).

A large amount of the phreatomagmatic slurry may remain inside the diatreme after explosive activity has ceased. Some of the material in these vent-fill deposits remains much as it was in the active stages of the explosive eruptions, creating a window into the chaos of vent

formation. However, sideromelane within the vent fill is highly unstable and readily alters to a yellow to brown material called palagonite by hydration, oxidation, and other chemical changes. The distinct color of palagonite is often indicative of vent-fill outcrops because the alteration can take place quite rapidly (Cas and Wright, 1987).

In a great deal of the research on maars, the deepest part mentioned in the diatreme is the "root zone", which represents the very base of the diatreme, just above the "feeder dike" (Fig. 3) (Lorenz and Kurszlaukis, 2007; White and Ross, 2011). More extensive and complex plumbing systems to maars have generally received less attention (Németh and Martin, 2007; Keating et al., 2008; Valentine, 2012). This is quite logical, given that the only way to definitively tell that a series of intrusions is related to phreatomagmatism is the presence of characteristic phreatomagmatic deposits, which have generally been cleared away by the very erosion which reveals this intrusive plumbing system. The geometry of the magma plumbing systems may be any combination of dikes, sills, and transgressive sheets (Németh and Martin, 2007; Deitz et al., 2010). When the intrusive material is emplaced into wet sediment, a steam carapace will form (Kokelaar, 1982; Krynauw et al., 1994), insulating the magma from extreme quenching and allowing the magma to propagate further. When the magma is moving against the wet sediment, a variety of textures develop along the margins of the intrusions. Billows may form on the sides of the intrusions, and if enough magma pressure is available, may expand outward into pillows, or even continue on to form intrusive tongues (Befus et al., 2009). In other cases, the magma quenches and fragments against the wet sediment and mixes with it to form peperite (Hooten and Ort, 2002; Lorenz et al., 2002).

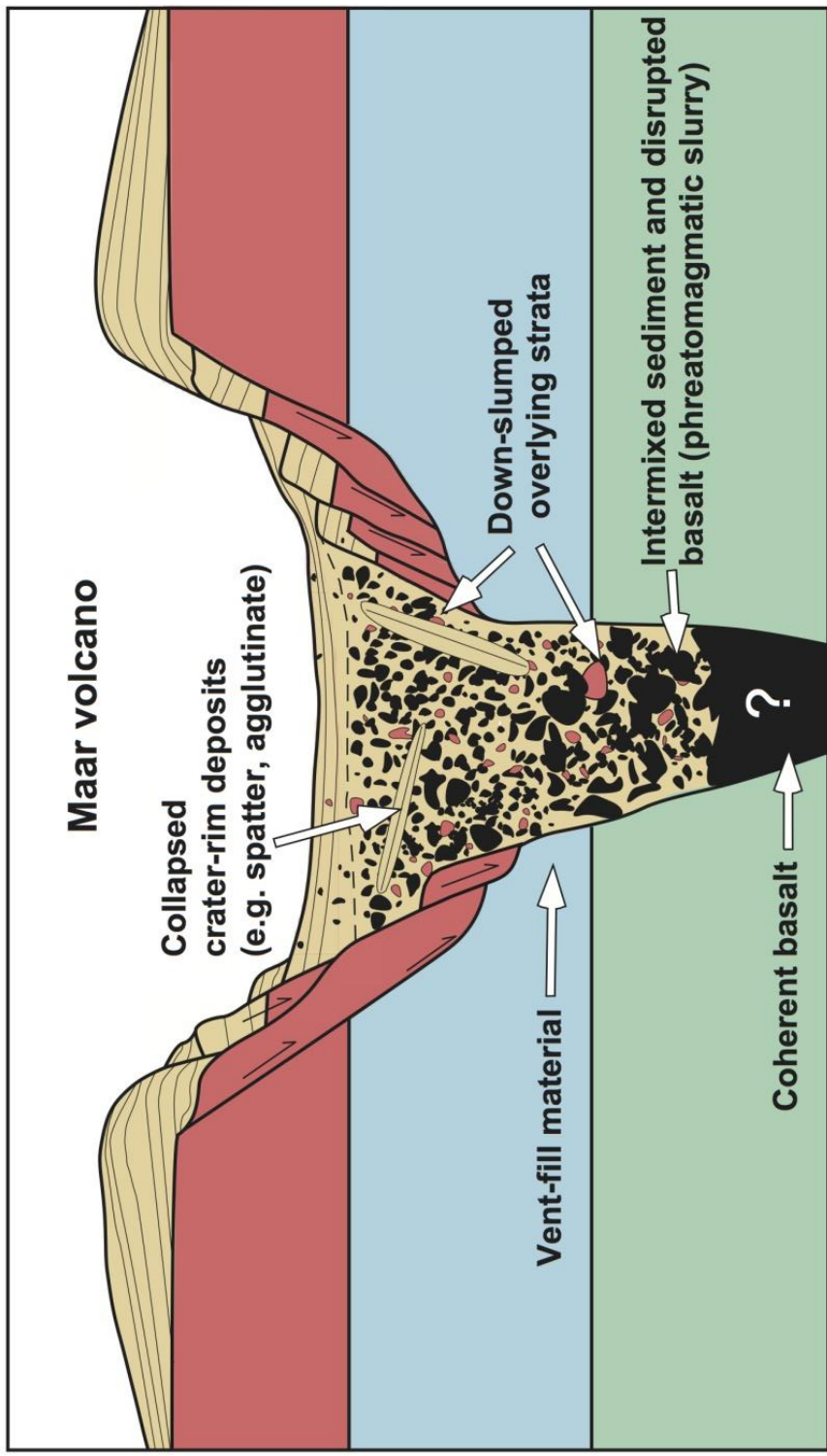


Figure 2. Diagram of a maar volcano, modified from Befus et al. (2009).

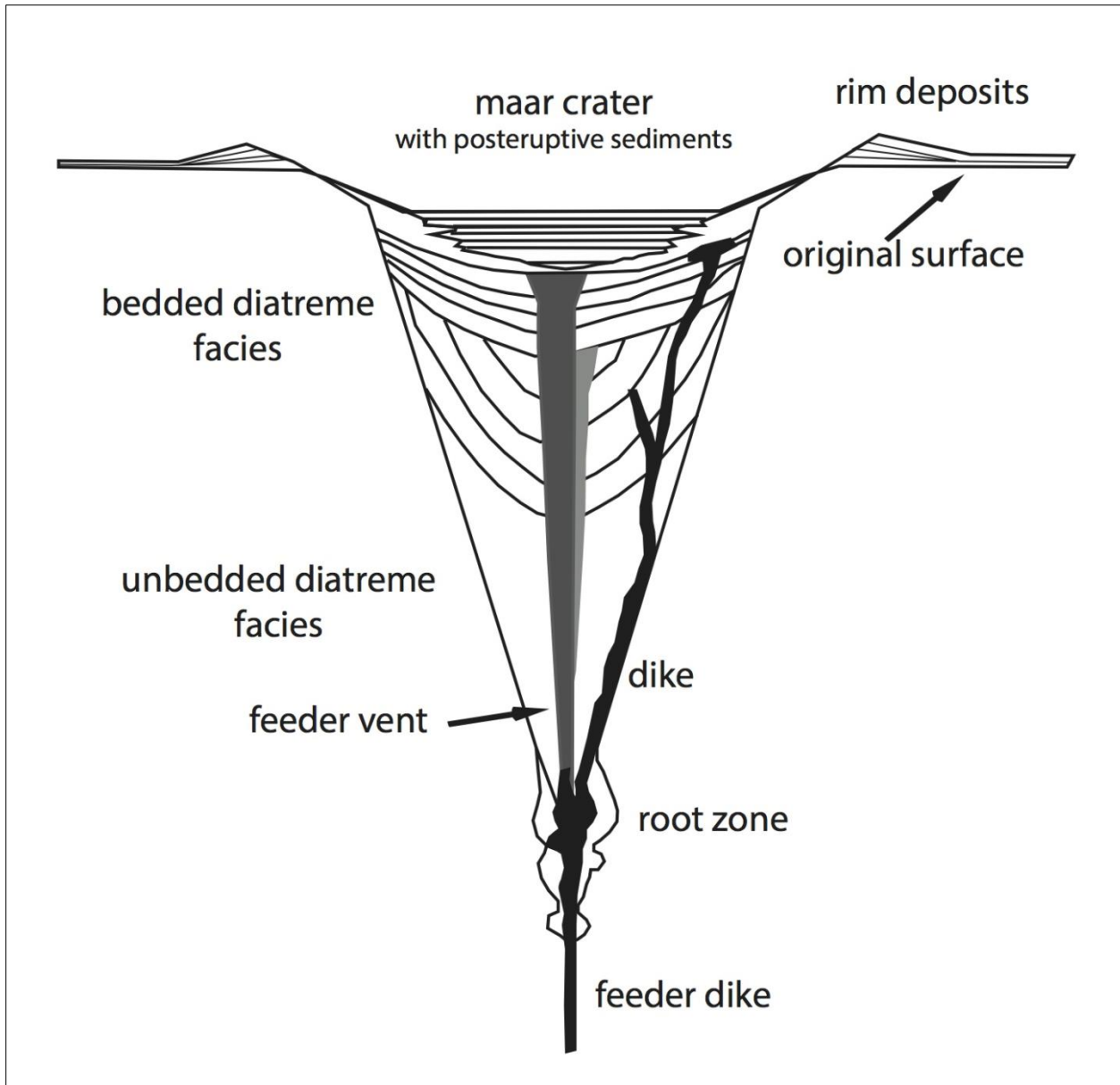


Figure 3. Traditional model of a maar, diatreme, and feeder dike, modified from Lorenz (2003).

Chapter 2: Regional Geologic Setting

Geologic Setting

The Trans-Pecos Magmatic Province is a major area of Tertiary (dominantly 48-17 Ma) igneous activity (Henry and McDowell, 1986). The province is delineated by the Pecos River in the east and the Rio Grande in the south and west and extends 12 km north into New Mexico (Fig. 1) (Barker, 1987). This magmatic province is only part of a diffuse belt of Cenozoic alkaline rocks which extends from Canada south to Mexico, along the eastern margin of the North American Cordillera (Barker, 1977). Since the Trans-Pecos Province is quite large and complex, the discussion will focus mostly on the rocks and events within Big Bend National Park, organized by major tectonic events over time (Fig 4).

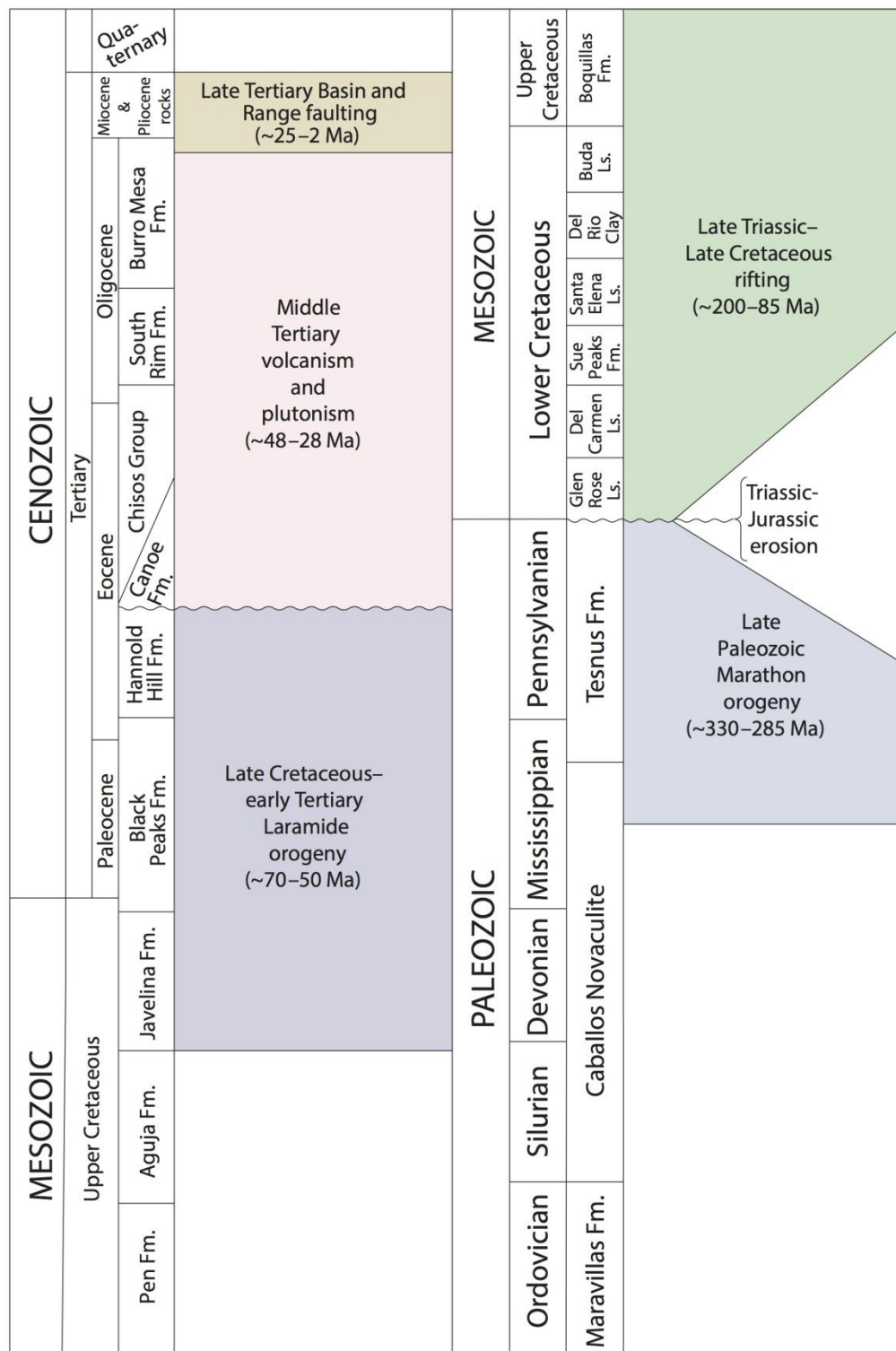


Figure 4. Stratigraphic column showing major formations and large-scale tectonic episodes in the Big Bend region. Modified from Page et al. (2008).

Marathon Orogeny

The oldest tectonic episode which is still preserved in Big Bend is the mountain building event which created the Marathon orogenic belt (Turner et al., 2011). This episode, which lasted from Middle Mississippian to Early Permian (~ 330-285 Ma) (Poole et al., 2005), thrust oceanic rocks onto the North American continent as it collided with South America (Muehlberger and Dickerson, 1989). The only outcrops remaining from this event are small belts of Paleozoic rocks overlying northwest-vergent thrust faults (Page et al., 2008).

Breakup of Pangea

During the Late Triassic until the Late Cretaceous (~ 200-85 Ma), the breakup of Pangea entailed the separation of the North and South American plates and the opening of the Gulf of Mexico (Shepard and Walper, 1982; Page et al., 2008). During much of this time, the majority of the Big Bend region was in a shallow marine depositional environment, until the Late Cretaceous when deposition shifted to a continental regime (Page et al., 2008). The Aguja Formation, made up of interbedded sandstone, calcareous and carbonaceous shale, and lignite, formed partly in coastal environments as the area shifted away from marine deposition (Turner et al., 2011).

An episode of Cretaceous (~ 76 Ma) basaltic phreatomagmatism in the region has recently been documented by Breyer et al. (2007) and Befus et al. (2008). The best examples of the deposits formed during this episode make up a sizable portion of Peña Mountain and record the construction of a maar, followed by collapse of the main vent and creation of one or more maars nearby (Befus et al., 2008). Breyer et al. (2007) and Befus et al. (2008) infer that this phreatomagmatic episode was a westerly extension of the Balcones igneous province, which is a Cretaceous phreatomagmatic volcanic province located along the older Ouachita orogenic belt (Befus et al., 2008).

Laramide Orogeny and Arc-Related Magmatism

The Laramide orogeny affected the Trans-Pecos region in the Late Cretaceous and Early Tertiary (70-50 Ma), when deformation and magmatism moved progressively inward across the North American plate (Henry et al., 1991). Historically, this shift of magmatism away from the trench has been explained by flat-slab subduction, where the oceanic slab does not descend directly into the asthenosphere a relatively short distance from the subduction zone, but remains near the base of the upper plate for a substantial distance before finally descending into the mantle (English et al., 2003). In a more typical convergent margin setting, the continental volcanic arc would be ~ 100-150 km from the subduction zone. However, during the Laramide event, because the subducting slab had to reach a certain depth before dewatering and partial melting of the overlying mantle wedge could occur, the associated continental volcanic arc spread quite far into the North American plate (Henry et al., 1991; White et al., 2006).

Laramide deformation in the Trans-Pecos area occurred in the early Eocene and ended at about 50 Ma (Price et al., 1987; Henry et al., 1991). This event generated compression directed east-northeast, creating faults and folds at a variety of scales as well as major basins and uplifts (Henry et al., 1991; Page et al., 2008). During this deformation, the Tornillo Basin was formed between the two massive monoclines which border the park as mountains on the east and west, the Sierra del Carmen-Santiago Mountains monocline and the Mesa de Anguila monocline, respectively (Page et al., 2008).

The Tornillo Basin was the depositional setting for the basin-fill deposits which occur in the study area. The Javelina Formation is a series of fluvial lenticular sandstones and flood-plain mudstones with evidence of paleosol development, and marks the beginning of Laramide deformation in the area (Page et al., 2008; Turner et al., 2011). The Black Peaks Formation

overlies the Javelina and was deposited in much the same environment, yielding similar sandstones and mudstones, as well as distinctive black mudstone layers and a sandstone rich in petrified wood (Turner et al., 2011). The Hannold Hill Formation, which is comprised of a conglomerate and a conglomeratic sandstone separated by mudstone layers, was the last formation to be deposited during Laramide deformation (Page et al., 2008; Turner et al., 2011). The overlying Canoe Formation, a mix of sandstone, tuffaceous mudstone, claystone, siltstone, tuffs, and basalt lavas, overlies the deformed Javelina, Black Peaks, and Hannold Hill Formations in the eastern part of Big Bend National Park, thus marking the end of Laramide deformation in the area (Page et al., 2008; Turner et al., 2011). The Chisos Formation, which is the major stratigraphic unit in my study area, is subdivided into two parts: older and younger (Turner et al., 2011). The older part, deposited within the same timeframe as the lower part of the Canoe, is only seen in the Chisos Mountains (Turner et al., 2011), and thus does not occur in my study area. The younger part of the Chisos Formation is quite distinctive in the field, owing to the presence of pale gray and white felsic tuff deposits, but the formation also contains tuffaceous sandstones and abundant claystone, mudstone, conglomerate, limestone, and lavas (Turner et al., 2011). The Chisos lava members are of interest to this study, and will be discussed in detail in Chapter 3.

Henry et al. (1991) placed Laramide-related magmatism in Arizona after ~ 70 Ma and in Texas after ~50 Ma. According to Gilmer et al. (2003), the porphyry copper deposits in Arizona and New Mexico are related to Laramide activity, and date between 75-54 Ma. About 300 km east of these copper deposits, a porphyry copper-molybdenum deposit associated with a felsic stock in the Red Hills was emplaced within the Trans-Pecos Magmatic Province between 64 and 60 Ma (Gilmer et al. 2003). This makes the Red Hills stock the oldest Tertiary igneous body in

the Trans-Pecos Province, suggesting an extension of Laramide magmatism further east at an earlier time than previously thought (Gilmer et al., 2003).

The main magmatism in the Trans-Pecos area is divided into four main episodes, as set forth by Price et al. (1987) and Henry et al. (1991): 48-39 Ma, 38-32 Ma, 31-27 Ma, and 24-17 Ma. The first episode of magmatism formed a segment of the continental arc which stretches from Canada to Mexico (Henry et al., 1991; Page et al., 2008). From ~ 47 Ma until 32 Ma, the maximum principal stress in the Trans-Pecos Province was directed towards the east-northeast, as it was during the main part of the Laramide orogeny, although the stress was likely at a lower magnitude because the convergence had slowed (Price et al. 1987; Henry et al., 1991). During the first stage of magmatism (48-39 Ma), numerous small intrusions were emplaced as well as both the Alamo Creek Basalt and the Ash Spring Basalt Members of the Chisos Formation, perhaps accounting for their similarities in composition (Carman et al., 2003; Turner et al., 2011). The second episode of magmatism, from 38-32 Ma, involved the greatest volume of magma out of all four episodes (Price et al., 1987; Henry et al., 1991). Rocks of this episode were emplaced in two geochemical belts, striking north-northwest, parallel to the trench 1,000 km away: an eastern alkalic belt and a western metaluminous/alkali-calcic belt, both of which were dominated by caldera eruptions (e.g. Barker, 1977; Price et al., 1987; Henry et al., 1991; White et al., 2006). This series of intrusions and extrusive units includes the Bee Mountain Basalt Member (~ 33-34 Ma), the Mule Ear Spring Tuff Member (~34 Ma), and the Tule Mountain Trachyandesite Member (~32-33 Ma), all within the Chisos Formation (Turner et al., 2011). Collectively, the magmas formed during this compressional period show geochemical patterns indicative of a subduction-related arc setting, according to James and Henry (1991), and

underwent a higher degree of differentiation than the magmas formed in the other episodes (Price et al., 1987).

These first two magmatic episodes may be explained by the model by Lawton and McMillan (1999), as applied to the Big Bend area by White et al. (2006). The first phase of the model is "normal subduction" magmatism, where primitive lavas from the dehydration and melting process are unable to rise through the crust as it experiences compression, or are trapped in more silica-rich magma chambers (Lawton and McMillan, 1999). The second phase is "early slab retreat" where the slab begins to retreat backwards ("foundering"), allowing asthenospheric upwelling into the space left by the slab (Lawton and McMillan, 1999; Parker et al., 2012). This causes partial melting of the subcontinental mantle lithosphere, and generates large crustal magma chambers which eventually produce caldera eruptions (Lawton and McMillan, 1999; Parker et al., 2012). Lawton and McMillan (1999) also proposed a third phase in their model, involving asthenospheric magmatism and basin subsidence, which is discussed below.

Transitional Tectonics

Evidence indicates that around possibly ~31 Ma and certainly by 28 Ma, regional stresses shifted from Laramide compression to Basin and Range extension, that is from maximum principal stress directed east-northeast to minimum principal stress directed east-northeast (Price et al., 1987; Henry et al., 1991). However, Basin and Range normal faulting did not commence until ~24 Ma (Price et al., 1987; Henry et al., 1991). Henry et al. (1991) classified magmatism before 32 Ma as continental-arc related, and magmatism after 24 Ma as being definitively related to within-plate extension. During this time of shifting stresses, Henry et al. (1991) delineated a third magmatic episode from 31-27 Ma.

According to Henry et al. (1991), the Trans-Pecos area experienced bimodal magmatism during this third episode of magmatism, as the area underwent a transition from an arc setting to a continental rift setting. The magmatism at this time consisted of two silicic calderas (at 30 and 28 Ma) and significant amounts of alkalic mafic to intermediate lavas (James and Henry, 1991). The rocks in this episode are more akin to a bimodal rhyolite-alkali basalt suite than to the compositions of the rocks during the previous two magmatic episodes (James and Henry, 1991). This compositional shift from the previous episodes of magmatism indicates a change in characteristics of the magma sources, and thus shifting tectonics.

While the Trans-Pecos area was beginning to exhibit a mixture of continental rift and continental arc magmatism, just west of the Trans-Pecos areas in northern Mexico, magmatism with arc-type trace element signatures continued (Henry et al., 1991). This lends credence to the plate foundering theory, and places the 31-27 Ma magmatic episode between the end of the second phase and the beginning of the third phase of the Lawton and McMillan (1999) model. The tectonic setting towards the end of the second phase, as discussed above, would explain the two calderas forming, and the continued influx of asthenosphere heating the mantle lithosphere that was previously affected by slab-dewatering processes explains the mixture of settings suggested by geochemical trends (Henry et al., 1991; Lawton and McMillan, 1999). The rising asthenosphere also heated the crust and caused extension, which explains the characterization of a "transitional period of early extension" by Price et al. (1987), and also explains the trace element signatures cited by Henry et al. (1991) as being indicative of intraplate rift environments. The third phase of the Lawton and McMillan (1999) model begins during this time (White et al., 2006), but will be discussed in the Basin and Range section, as this is when the phase is in full effect.

Basin and Range Faulting

Basin and Range faulting, which began around ~24 Ma (Henry et al., 1991; Page et al., 2008), is the most recent major tectonic episode to affect the Trans-Pecos Province. As discussed above, the stresses in the area shifted to Basin and Range extension with minimum principal stress directed east-northeast possibly by 31 Ma and definitely by 28 Ma (Henry et al., 1991). Basin and Range faulting, which was exclusively of the high-angle normal variety, did not begin until just before 24 Ma, as constrained by 24 Ma lavas which are interbedded with the lower basin-fill layers, but never occur at the base (Henry et al., 1991). The extension was originally accommodated by preexisting west-northwest zones of weakness associated with the Texas Lineament, but eventually a north-northwest fault system developed, as that orientation accommodated the extension more efficiently (Henry and Price, 1986; Price et al., 1987). Movement along the Basin and Range faults accounts for the current topography (Henry and Price, 1986).

After a hiatus of several million years, the fourth and final magmatic episode occurred from 24 to 17 Ma (Henry et al., 1991). Although this episode was quite widespread, it was the least voluminous (Price et al., 1987; Henry et al., 1991). These magmas were emplaced mostly as dikes with a few associated lavas, and are almost exclusively alkali basalts and hawaiites (Henry et al., 1991). North-northwest-striking fractures and faults tapped basalts from a mantle source by 24 Ma, which would account for the orientation of the dikes and is consistent with east-northeast extension in the area (Henry and Price, 1986; Henry et al., 1991). Collectively, these rocks show compositions indicative of intraplate mantle sources without any obvious trace of arc-related magmatism (James and Henry, 1991), and show little evidence of assimilation of

crustal material (White et al., 2006). Magmatism died out by ~17 Ma while faulting continued until the present (Henry and Price, 1986; Henry et al., 1991).

Since the magmatism shows characteristics suggesting an asthenospheric source with very little differentiation or assimilation (Price et al., 1987; White et al., 2006), the Basin and Range tectonism falls under the third and final phase of the Lawson and McMillan (1999) model, as discussed by White et al. (2006). During the third phase, the slab continues to founder, drawing back and allowing still more asthenosphere to well upwards, eventually creating a convection cell (Lawson and McMillan, 1999). The convection cell generates decompression melting of the asthenosphere, completely replacing lithospheric magmatism with melts supplied directly from asthenospheric material (Lawson and McMillan, 1999). At the conclusion of this process, the subduction zone is abandoned or retreats, removing pressure on the extending lithosphere and mafic magmatism continues in the extensional basins (Lawson and McMillan, 1999), explaining the geochemical signatures of the fourth episode of Trans-Pecos magmatism (White et al. 2006). Taking this theory to its logical conclusion, Basin and Range extension could represent crustal spreading solely due to asthenospheric upwelling. However, it seems more logical to attribute the driving mechanism of the extension to a combination of asthenospheric upwelling and the shift from subduction to a transform fault at the western margin of the North American plate.

Quaternary Erosion

The primary event during the Quaternary Period was erosion (Page et al., 2008). Massive amounts of erosion and down-cutting created the dramatic topography seen in the region today. This erosion also revealed more resistant rocks, allowing the opportunity to study the intrusive magmatism found in my study site and many other areas.

Eocene Basaltic Phreatomagmatism within and near Big Bend National Park

Recent studies by TCU workers on Eocene phreatomagmatic basaltic volcanism within and adjacent to Big Bend National Park have focused on three geographically separate locations (Fig. 5) (Befus et al., 2009; Winkler et al., 2009; Deitz et al., 2010). Befus et al. (2009) documented the first examples of Eocene basaltic phreatomagmatism to be discovered, which are located on the southern flank of the Rosillos Mountains. Two age groups of phreatomagmatism were found based on $^{40}\text{Ar}/^{39}\text{Ar}$ dating: ~47-46 Ma and ~42 Ma (Befus et al., 2009). The ~47-46 Ma group consists of two intrusive complexes that are made up of disrupted sediment from the surrounding formations; coherent basalt; basalt shot through with tendrils of sediment; peperite; basalt pillows; and large coherent masses derived from structurally higher formations. These intrusive complexes are inferred to represent horizontal cross-sections through the diatreme feeders to maar volcanoes (Fig. 2), containing rafts of rim material, remnants of the phreatomagmatic slurry, and coherent basalt which intruded the complex after explosions ceased (Befus et al., 2009). The 42 Ma intrusions are a complex of dikes and sills with quenched margins showing billows and intrusive pillows. In some areas, both blocky and fluidal peperite also developed along the intrusive contacts. Although the 42 Ma intrusions were emplaced into wet, unlithified sediment, the system was unable to generate explosive phreatomagmatism (Befus et al., 2009). Thus, this area offers views into the diatremes as well as insight into the products formed by non-explosive water/magma interactions.

The next site, a prominent hill located off the east side of the main park road in the northern portion of the park, was studied by Winkler et al. (2009). Two facies were distinguished within the hill, comprising a chaotic, igneous complex with a roughly elliptical outline up to ~300 m wide, that cuts strata of the Hannold Hill Formation and contains large masses of felsic

tuff from the stratigraphically higher Canoe Formation (Winkler et al., 2009). Facies A consists of both fluidal and angular pyroclasts of variable vesicularity, largely altered to palagonite, all mixed with sediment and disaggregated Canoe tuff. Facies B is a mixture of sediments and highly vesicular basaltic bombs and lapilli, deposited on blocks of Canoe tuff (Winkler et al., 2009). Facies A is interpreted to be the remains of the phreatomagmatic slurry filling a relatively large diatreme, while Facies B is the material which was ejected from the diatreme onto the rim of the crater, and then slumped back into the diatreme as the maar widened.

On the west side of Big Bend National Park, near the town of Study Butte, a third location was studied by Deitz et al. (2010). Two irregular, discordant masses of igneous material protrude from the surrounding Cretaceous strata and contain fluidal to angular basaltic pyroclasts of variable vesicularity and spatter mixed with clasts of vitric tuff, mudstone, and sandstone (up to 2.5 m long), all within a sediment-rich matrix. These masses are inferred to be the remnants of phreatomagmatic slurry filling two diatreme feeders to small maars. Zones of similar material are also exposed along some dikes in the area (discussed below) and are up to several meters wide. These are interpreted to be phreatomagmatic fissure vents which were later intruded by magma after explosive activity ceased (Deitz et al., 2010).

The Study Butte study area is quite illustrative because of the network of dikes and sills which surround and connect with the phreatomagmatic vents. These intrusions are considered to be the magma plumbing system to the vents (Deitz et al., 2010). The surfaces of the intrusive bodies show billowed surfaces and peperite, along with complex, intertonguing contacts with the surrounding material, demonstrating the wet, poorly lithified condition of the surrounding strata at the time of intrusion. These dikes (varying between 0.2 and 20 m wide) and sills (up to tens of meters thick) intrude the Aguja, Javelina, and Black Peaks Formations (Deitz et al., 2010). The

entire area dips to the southeast on the flank of the Terlingua monocline (Erdlac, 1990), and displays an approximately cross-sectional view of the plumbing system (Fig. 6).

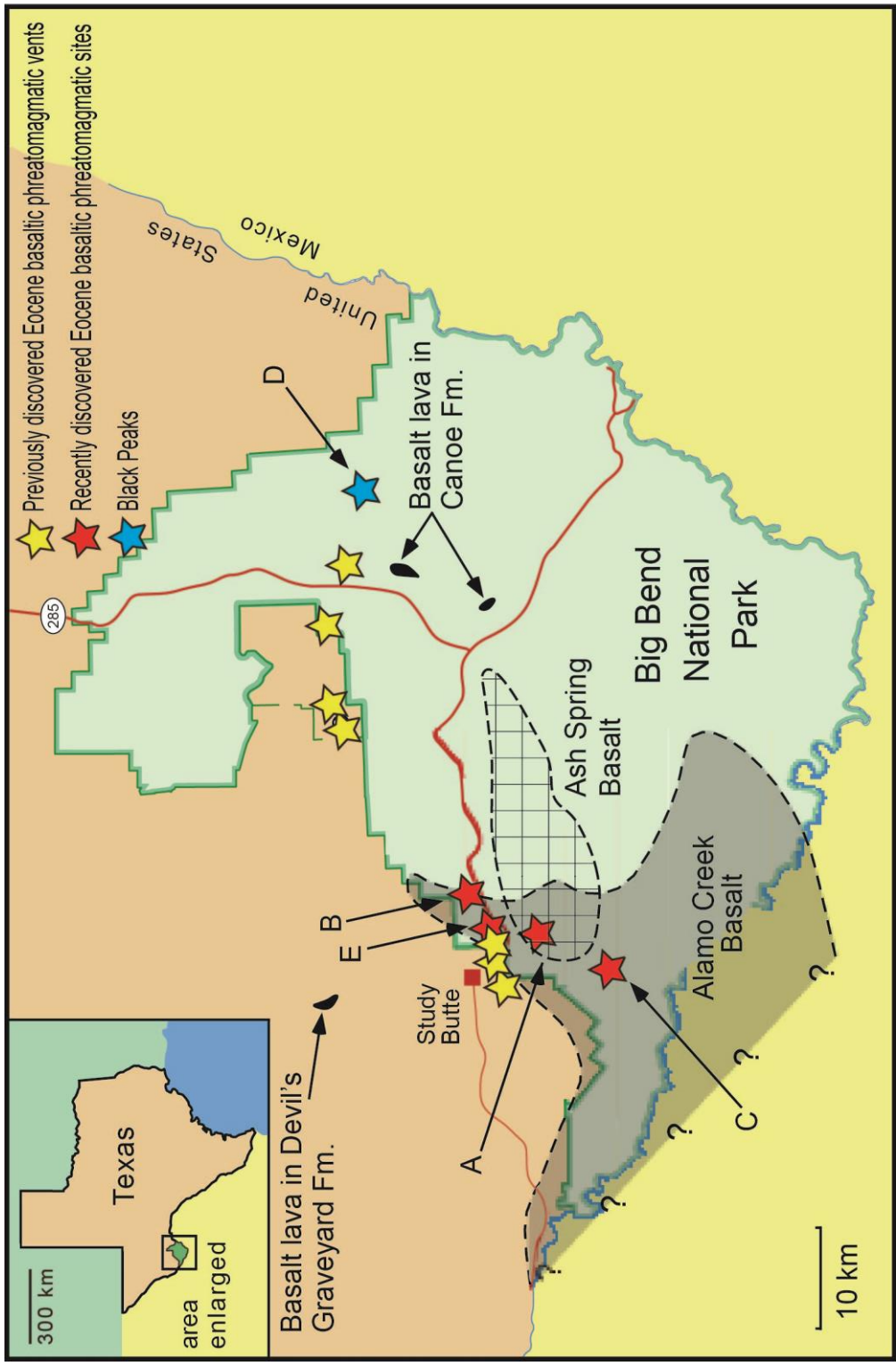


Figure 5. Eocene basaltic phreatomagmatic vents in the Big Bend region. A- Northwest of Tule Mountain; B- Doggie Mountain dike; C- East of Peña Mountain; D- Black Peaks; E- East of Study Butte. Modified from a figure drafted by K. Befus.

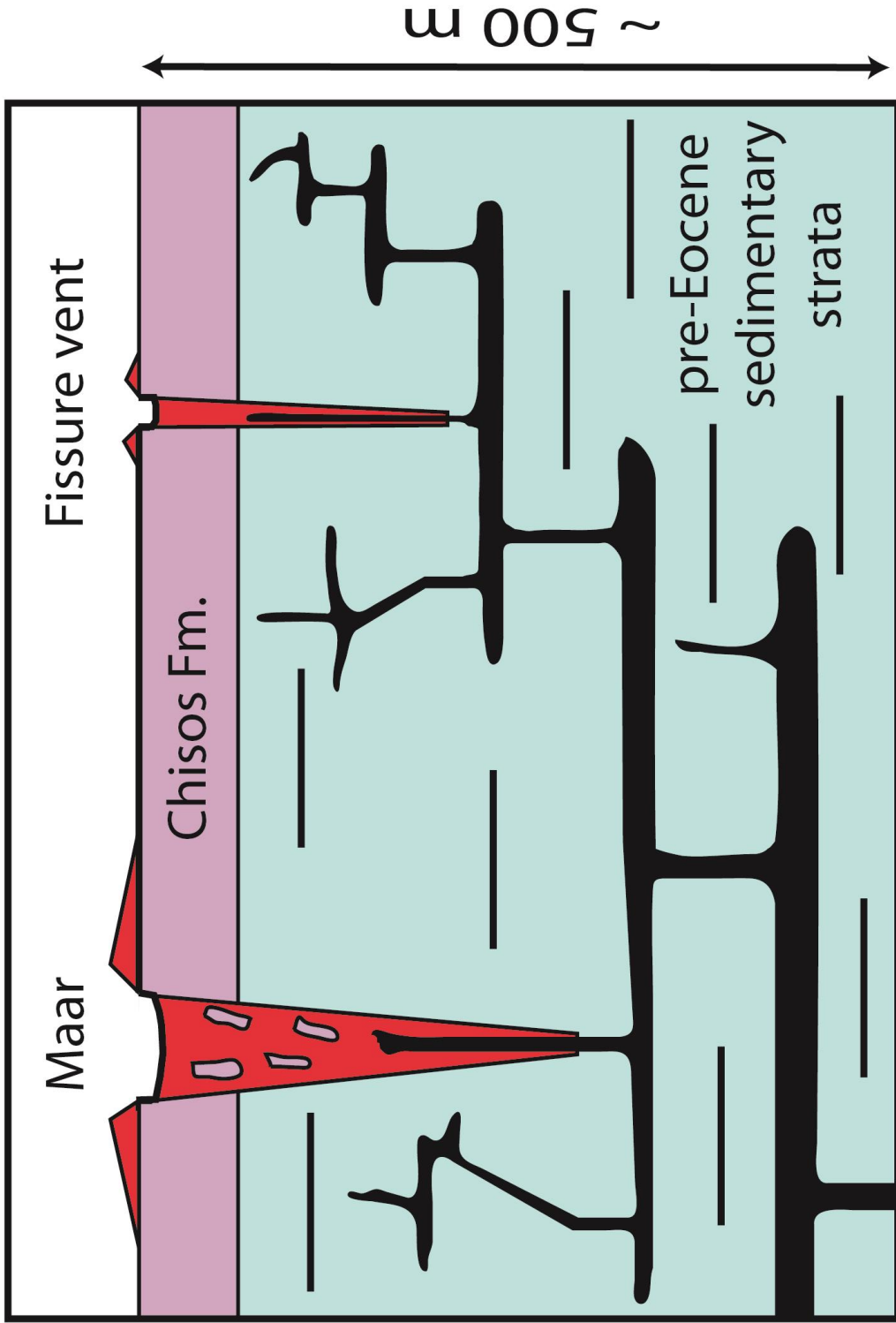


Figure 6. Model for Study Butte magma plumbing system, modified from a diagram drafted by R. Hanson.

Newly Discovered Eocene Phreatomagmatic Sites

A sizable amount of fieldwork has been done as part of this project, prior to the selection of a specific study area. Initially, Google Earth was used to identify a number of sites with possible vents in the Big Bend area. Many of these sites were originally noted by Dan Miggins. The intent was to conduct field reconnaissance to determine both the extent of the phreatomagmatic vents and to identify sites suited to detailed study. These sites are discussed below.

Northwest of Tule Mountain

In the area to the northwest of Tule Mountain in the western part of Big Bend Park (Fig. 5) we have found several adjoining small vents, which are filled with basaltic pyroclastic material and are intruded by coherent basalt. The vents form a ridge ~200 m in length, alongside a stream bed. On the western face of the ridge, the southernmost vent within this trend is well exposed and particularly complex. An undulating sheet of basalt intruding Chisos strata also intrudes into the vent-fill material. Underlying this coherent basalt is a body of pyroclastic material consisting of basalt lapilli and large amounts of calcareous mudstone, showing textures similar to vent-fill material. However, the material shows intrusive relations with the Chisos strata. Therefore we infer that this wedge of material was explosively injected laterally into unlithified sediment and never reached the surface. Similar material forms a vertical pipe-like mass on the southern face of the ridge, but here bombs of vesicular basalt up to 1 m in length are visible within lapillistone, suggesting that this material fills a vent which reached the surface. Coherent basalt intruding the sediment/basalt mix in the vents represents a later, less explosive stage of the event. Still another vent is exposed south of the main vent complex, but along the

same trend, and shows similar textures and sediment proportions to the vent-fill material in the main complex.

East of this main vent complex is a small but dramatic pipe-like exposure of vent-fill material, < 3 m wide and ~ 5 m tall. This outcrop shows a large proportion of sediment relative to basalt, suggesting a higher initial sediment-magma ratio. Blocks of agglutinate are present, which are inferred to have slumped down into the vent from the now-eroded ejecta rim. The presence of these agglutinate blocks is excellent evidence for vent widening and inward slumping of overlying material, showing that this pipe-like mass fed a small maar. Rounded pebbles within the vent-fill material (Fig. 7) appear to have originated from a conglomerate which the vent cut through and which crops out nearby. Coherent basalt intrudes all of the material, once again showing evidence of a later, less explosive episode of volcanism. Also, fine-scale peperite is visible where calcareous mud mingled with quenched intrusive basalt.



Figure 7. Pebble in vent fill. Pen for scale.

Dogie Mountain Dike

Dogie Mountain is a prominent feature in the western region of Big Bend National Park (Fig. 5). On the east side of Dogie Mountain, a basaltic dike intrudes strata of the Black Peaks and Chisos Formations. This dike is up to ~4 m wide and is exposed for ~4 km. In one place on the east side of the dike, a remnant of vent-fill material ~3 m across is present. Abundant spatter and basaltic clasts are mixed with a large amount of sediment, which consists of calcareous mudstone intermingled with terrigenous sand grains. Tongues of basalt intrude the sediment and appear to be connected in three dimensions to the dike. In one case a tongue has disaggregated into a zone of peperite. We infer that this vent records an initial episode of phreatomagmatism along the trend of the dike. Many other areas on the dike margins show billowed surfaces and sediment-filled invaginations between the more bulbous billows (Fig. 8), both of which point to intrusion of the dike into unlithified sediment (Befus et al., 2009). These features are inferred to occur along dynamic surfaces between wet, unlithified sediments and intruding magma (Befus et al., 2009).



Figure 8. Billows on dike margin, with baked sediment still attached in places. Blue pencil for scale.

East of Peña Mountain

The area east of Peña Mountain, in the western region of Big Bend Park (Fig. 5), provides a look into a more convoluted intrusive system associated with phreatomagmatic activity. Initial reconnaissance fieldwork in this area revealed bulbous or irregular masses of basalt and diabase up to tens of meters across which intrude the host Chisos strata in a highly complex manner. Three locations of vent-fill material were initially found in this area, each several meters across. The best example shows basalt clasts of varying vesicularity mixed with mudstone. Basaltic bombs up to ~1 m across were also found in the vent-fill material, as well as basalt pyroclasts from ~12 cm down to less than 1 mm in size finely mixed with the sediment. Fingers of coherent basalt also intrude the vent-fill.

Black Peaks

In the northeast portion of Big Bend (Fig. 5), three dark cone-shaped hills protrude from the flat plains and are termed the Black Peaks (Fig. 9). They occur in an area underlain by the Black Peaks Formation. Two of the peaks show two types of mafic rocks: vesicular basalt and nonvesicular diabase. At the tops of these two peaks, the basalt is intermingled with calcareous mudstone, forming mostly fluidal basalt clasts with a few small tongues of coherent basalt. This material may be remnants of vent fill, but more study is needed to confirm this interpretation. The smaller peak to the west shows nonvesicular basalt intruding conglomerate at the top of the hill. The basalt penetrates the conglomerate as tongues associated with peperite. More detailed study is needed to determine whether a vent conduit can be seen sourcing the magma-sediment mix present at the tops of the hills.

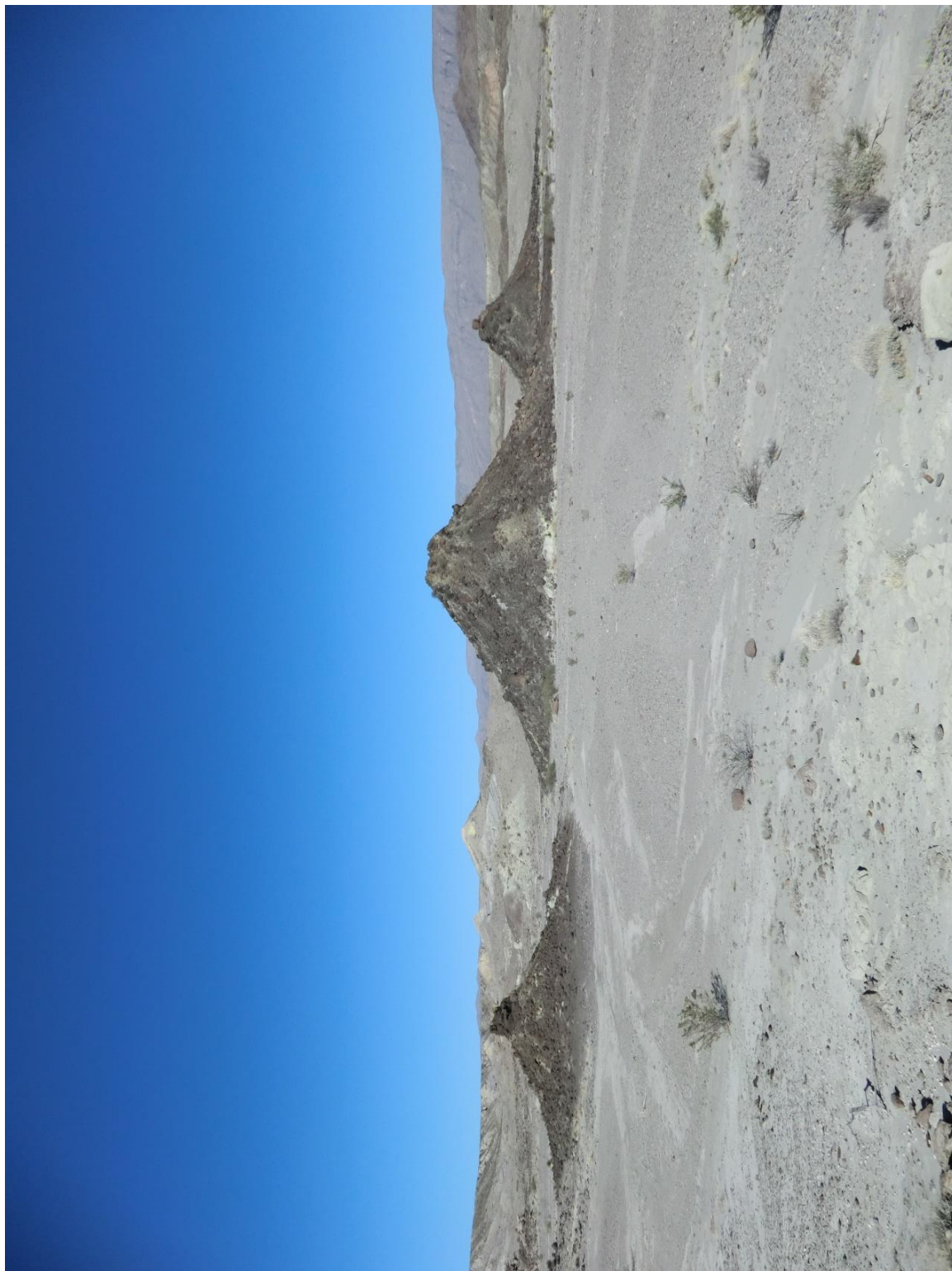


Figure 9. View of all three of the Black Peaks.

East of Study Butte

Approximately 1 km to the northeast of the area near Study Butte (Fig. 5) which was studied by Deitz et al. (2010), we discovered another vent connected to a dike, similar to the example shown in Figure 10. The dike intrudes Javelina sandstone, runs roughly north-south, and is ~60 m long and up to 5 m wide. Vent-fill material is exposed along part of the dike margin, and contains basalt clasts up to ~15 cm wide mixed with a moderate amount of calcareous mudstone. The discovery of this site shows that the dike-sill-vent complex previously studied by Deitz et al. (2010) extends farther to the east than previously thought.

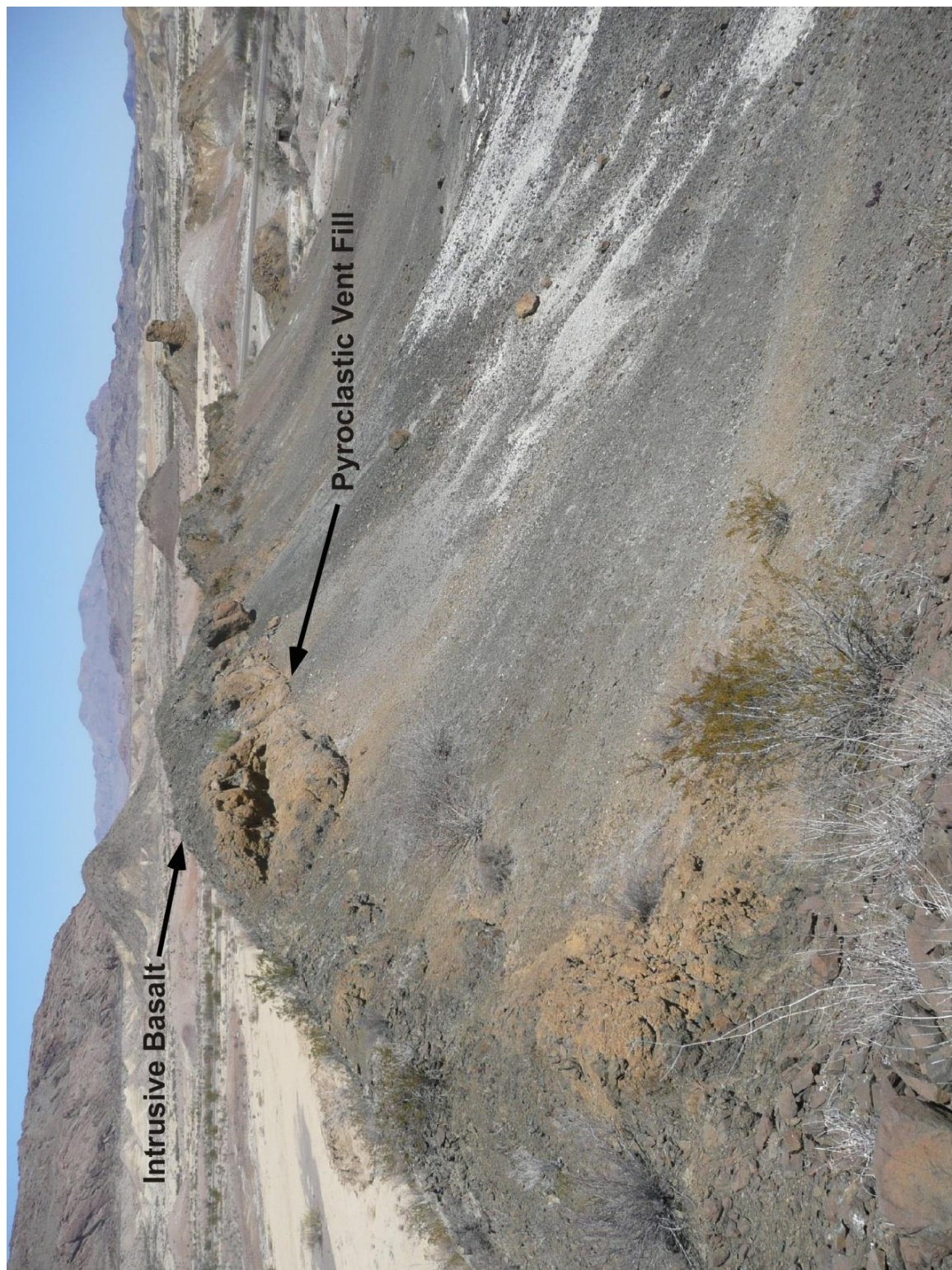


Figure 10. Fissure vent in dike-sill complex near Study Butte. Photo from R. Hanson.

Selecting a Study Area

Due to the detailed nature of the planned study and the interest in the magma plumbing systems which sourced the phreatomagmatic vents, only one of the five sites was investigated for this thesis project. Preference was given to the sites with both vent-fill material and coherent intrusive material. Areas where structural effects and topographic relief unveiled the magma plumbing system were also necessary for the purposes of this study. The Black Peaks area was discarded from future study because of the limited outcrop. In the Doggie Mountain dike area, only one small location of vent-fill material was found during an entire day of exploring, making this area unsuited to further study. The area east of Study Butte, while potentially complex, is a continuation of the area studied by Deitz et al. (2010), and thus is less promising than an unexplored area. The area northwest of Tule Mountain provides only limited exposure, and so was discarded despite the complexity of the main exposures. Finally, the reconnaissance in the area east of Peña Mountain revealed three vent zones in close proximity to large, complex exposures of basalt and diabase. Thus, Peña Mountain was deemed to be the best option for further study into the magma plumbing systems of maar vents in the Big Bend region and was therefore chosen as the main study area of this thesis.

Chapter 3: Geologic Setting of the Study Area

The study area east of Peña Mountain is set within a network of north-northwest trending faults, amidst mostly sedimentary formations. The igneous rocks in the area, aside from the intrusions which will be discussed in Chapter 4, are the Alamo Creek and Ash Spring Basalt Members of the Chisos Formation, and the Tertiary intrusion which caps Peña Mountain on the western edge of the map in Figure 11. The map shows extensive areas of pediment as well as extensive amounts of recent alluvium.

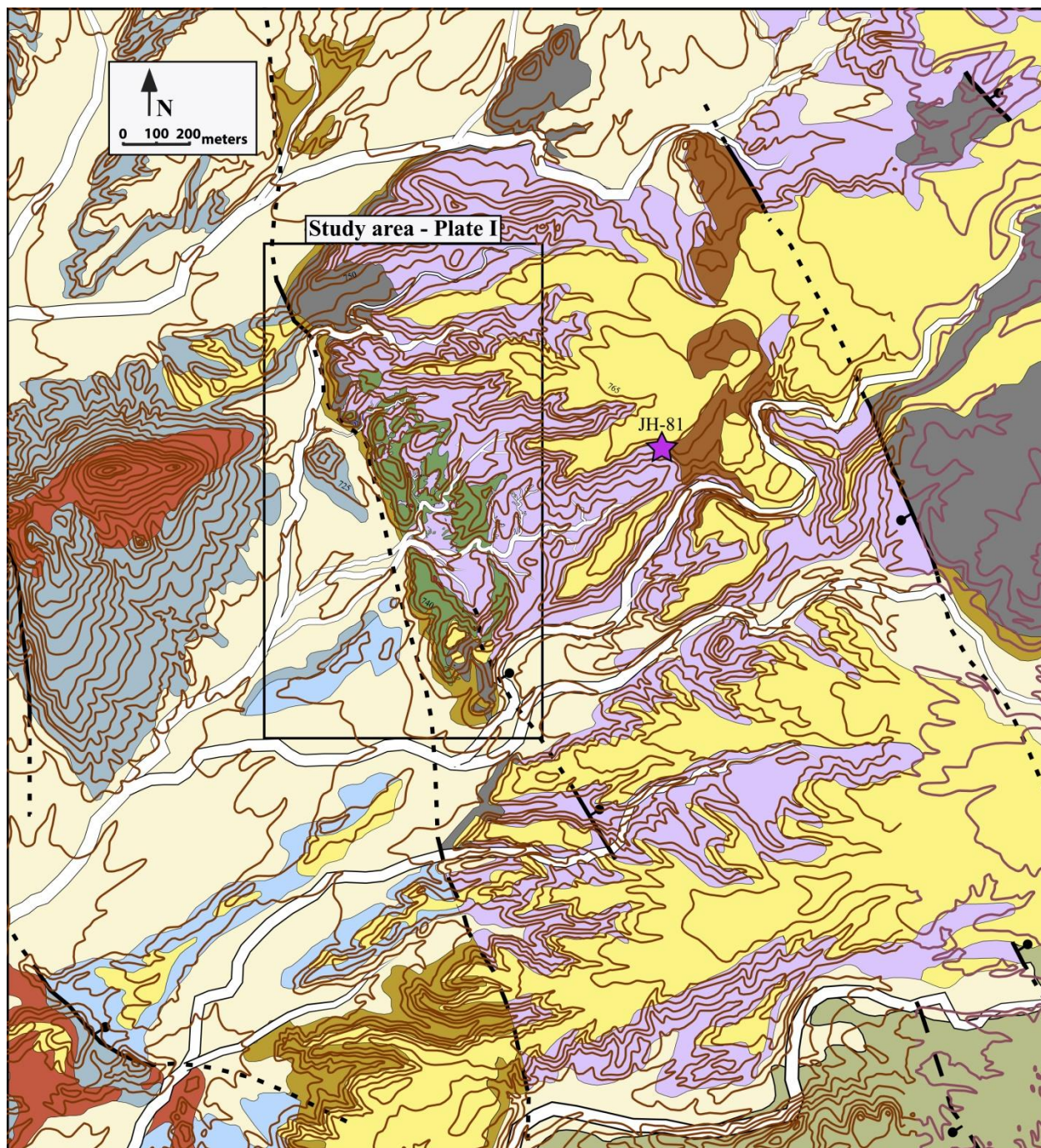


Figure 11. Geologic context of study area. Mapping outside of study area is adapted from Turner et al. (2011).

Stratigraphy

The Upper Cretaceous to Tertiary stratigraphic units which bear on this study (Fig. 4), mentioned briefly in their full geologic context in Chapter 2, will now be discussed in detail. The nomenclature of Turner et al. (2011) is followed; in the Chisos Formation, this stratigraphy is an amalgamation of the nomenclature of Maxwell et al. (1967) and Henry and Davis (1996). The general geologic setting is shown in Figure 11, with a box around the study area which is enlarged in Plate I.

Aguja Formation

As mentioned in Chapter 2, the Upper Cretaceous Aguja Formation marks the start of a change in the depositional setting in Big Bend, from a marine to a continental environment. Marine deposits of the Pen intertongue with marine sandstone and mudstone of the lower Aguja, forming a gradational and conformable contact between the two formations (Turner et al., 2011). The upper, littoral to terrestrial part of the formation is comprised mostly of mudstones which show a range in color. The hills of Aguja Formation along the western edge of the study area are pale grey to cream in color, which places the units in the uppermost portion of the terrestrial mudstones of the Aguja (Lehman, 1985). These deposits were formed in coastal plains, deltas, inland floodplains, and swamps (Lehman, 1985; Turner et al., 2011).

Peña Mountain forms a prominent ridge less than a kilometer to the west of the study site, within the southwest portion of Big Bend National Park (Fig. 11). The top of the ridge is an Oligocene syenodiorite intrusion which is likely a thick sill (Carman, 1994). The sill intrudes the Cretaceous Aguja Formation as well as pyroclastic deposits within the Aguja Formation (Befus et al., 2008). These pyroclastic deposits are interpreted to be remnants of maar volcanoes which were formed during the Cretaceous (~77 Ma) (Befus et al., 2008).

Javelina Formation

The Upper Cretaceous Javelina Formation conformably overlies the Aguja Formation (Turner et al., 2011). The Javelina Formation is composed primarily of mudstone, generally in hues of white, grey, maroon, and tan, and commonly occurring with calcareous nodules and other evidence of paleosol development (Lehman, 1985). Lenticular sandstones are also present in shades of tan and brown (Lehman, 1985). Together, these deposits indicate a floodplain environment which experienced overbank flooding and intervals of soil formation as well as deposition within meandering stream channels (Lehman, 1985; Turner et al., 2011).

Black Peaks Formation

The Upper Cretaceous-Paleocene Black Peaks Formation forms a gradational and conformable contact with the Javelina Formation (Turner et al., 2011). The Black Peaks Formation contains mudstones similar to the Javelina, with the exception of brighter maroon layers, wine-red layers, and distinctive black mudstones (Lehman, 1985). Black Peaks sandstone units are also quite similar to those in the Javelina Formation, although typically lighter in color than the sandstones of the Aguja (Maxwell et al., 1967). These deposits indicate a continuation of the depositional environment recorded by the Javelina Formation, although with slight differences in the formation of the paleosols, as indicated by the color changes (Lehman, 1985). The Black Peaks Formation forms the base of the hills on the western edge of the study area (Plate I).

Chisos Formation

The Eocene-Oligocene Chisos Formation unconformably overlies the Black Peaks Formation in the western part of Big Bend, with the Alamo Creek Basalt Member forming the base of the Chisos, as discussed below (Turner et al., 2011). The Chisos Formation in the study

area consists of lavas (discussed below), tuffaceous sandstone, claystone, mudstone, limestone, and tuff (Turner et al., 2011). All of the Chisos sedimentary rocks and tuff are generally pale grey to white. Most of the sedimentary units occur between the lower Alamo Creek Basalt and younger Bee Mountain Basalt Members, but some sedimentary units are found above the Bee Mountain Basalt (Turner et al., 2011). Another lava unit, the Ash Spring Basalt Member, also occurs between the aforementioned basalt members.

Chisos Formation Lava Members

In the western part of the Chisos Formation, where the study area is located, the Alamo Creek Basalt Member of the Chisos typically overlies eroded Black Peaks rocks (Turner et al., 2011). The Alamo Creek Basalt ranges in composition from basalt to trachyandesite, and has yielded isotopic dates of 47-46 Ma (Turner et al., 2011). Although Alamo Creek Basalt has been mapped over a large portion of the park, Carman et al. (2003) delineated eight flow units and show their "Unit F" cropping out in the present study area east of Peña Mountain. Carman et al. (2003) describe the majority of the Alamo Creek Basalt flows as being distinctly porphyritic with phenocrysts of plagioclase up to 7 mm long and a varied assortment of pyroxene, olivine, and opaque phenocrysts in a commonly intergranular groundmass. Unit F is an exception, in that it is an essentially aphyric basalt (Carman et al., 2003; Parker et al., 2012). Carman et al. (2003) also suggest that Unit F may be made of multiple lava flows, based on geochemical evidence, although they were unable to corroborate this in the field.

The Ash Spring Basalt Member of the Chisos Formation is composed of two or more lavas, is classified as basaltic trachyandesite to trachyandesite, and is considered to have an age of 42-41 Ma (Turner et al., 2011). During the course of this study, we collected a sample of Ash Spring Basalt from the westernmost outcrop of the basalt, near the study area (Fig. 11). Thin-

section and hand-sample study indicate that this rock is more leucocratic than a typical basalt. The sample shows phenocrysts of fresh plagioclase up to 3 mm in length that make up ~ 3% of the total rock and olivine altered to iddingsite up to 0.7 mm in length and occurring in amounts of < 1% olivine. The groundmass is mostly intergranular with sparse patches of intersertal texture. The geochemistry of the sample will be discussed in Chapter 5.

Although the Bee Mountain Basalt Member of the Chisos Formation is not exposed in the study area, it is also important to this study. It is comprised of multiple lava flows, ranges from basalt to basaltic trachyandesite in composition, and has yielded isotopic ages of 34-33 Ma (Turner et al. 2011). The Bee Mountain Basalt has been divided into an upper and lower group, based on stratigraphy and geochemistry (Turner et al., 2011). The different flows vary from nearly aphyric to highly porphyritic with phenocrysts of plagioclase, olivine, and magnetite (Parker et al., 2012).

Faults

The Trans-Pecos region has been transected by a series of faults, from faults related to the Texas Lineament which possibly follow Proterozoic basement trends, to the currently active Basin and Range fault assembly. In the immediate vicinity of the study area, faults generally strike north-northwest and exhibit offsets in a normal sense, due to Basin and Range extension.

Maxwell et al. (1967) originally mapped one normal fault through the study area for this thesis, between the Alamo Creek Basalt and the Chisos Formation. The recent Turner et al. (2011) map shows two faults in the present study area (Fig. 11), which will be referred to as the eastern and western faults. The eastern fault mapped by Turner et al. (2011) is approximately in the same location as the Maxwell et al. (1967) fault, but the former authors show the normal fault juxtaposing Alamo Creek Basalt and Black Peaks on the western block, and Chisos and

undivided mafic intrusive rocks on the downthrown eastern block (Turner et al., 2011). The western fault is partly concealed in the study area, and separates a western block of Aguja, Javelina, and Quaternary exposures from an eastern downthrown block of Black Peaks and Alamo Creek Basalt (Turner et al., 2011). This places a fault block containing Black Peaks and Alamo Creek Basalt between two normal faults (Fig. 11).

In the detailed field mapping conducted for this project, the western fault was confirmed in two locations, at points 1 and 2 in Plate I. At point 1 in Plate I, the northern Alamo Creek Basalt outcrop is deformed and likely truncated by the fault along its western margin (Fig. 13). Two outcrops at point 2 in Plate I show evidence of faulting: one outcrop juxtaposed intrusive diabase against Black Peaks purple mudstone without any chilled margin or baked contact, and the second outcrop shows a fault cutting the intrusive diabase itself. The only evidence found for the continuation of this fault to the south was the juxtaposition of Aguja and Javelina rocks against Black Peaks strata. Evidence for the eastern fault was found only in the southern portion of the study area (points 3 and 4 in Plate I). In the area of point 3 on Plate I, strata of the Chisos Formation and intrusive basalt on the east are placed against Alamo Creek Basalt, intrusive diabase, and Black Peaks on the west, without any baking of the sedimentary units or chilling of the igneous rocks. The outcrops around point 4 on Plate I show Chisos units against Black Peaks and Alamo Creek Basalt at a high angle with a similar lack of baking or a chilled margin (Fig. 12). A pediment cap obscures the fault between the two confirmed zones, and the fault is presumably covered by sediment north and south of this area.



Figure 12. Fault juxtaposing Alamo Creek Basalt on left with Chisos strata on right. Author for scale. View looking north at point 3 in Plate I.



Figure 13. Fault juxtaposing Chisos strata on left with Alamo Creek Basalt and Black Peaks strata on right. Hammers for scale, at base of outcrop against white Chisos strata.

Chapter 4: Basalt Lava, Phreatomagmatic Vents, and Hypabyssal Intrusions East of Peña Mountain

Introduction

This chapter provides detailed discussion on each of the igneous units found in the study area. The Alamo Creek Basalt lava, vent-fill outcrops, and hypabyssal mafic intrusions are discussed in terms of field relations, hand-sample identification, and thin-section observation. Field relations comprise the bulk of the observations, with details on mapped extent, contacts between units, and specific features found in each unit.

Alamo Creek Basalt Lava

Basalt lava of the Alamo Creek Basalt Member of the Chisos Formation crops out near the northern and southern edges of the study area (Plate I). The basalt varies in thickness from a maximum of ~6 m to areas where it thins out completely. The lava is largely homogeneous, with the exception of some areas with large (up to 1 cm) amygdules, generally filled with carbonate.

Most of the basalt outcrops have undergone spheroidal weathering and some have been weathered quite extensively (Fig. 14). Overall, the basalt is holocrystalline with a phaneritic groundmass (crystals < 0.2 mm) and contains plagioclase microlites (< 1 mm) and altered olivine phenocrysts (< 1.5 mm). The phenocrysts are sparse and make up < 2% of the total rock, with plagioclase and olivine occurring in roughly equal proportions. In thin section (Fig. 15), the groundmass is intergranular with abundant interstitial olivine, altered to smectitic clay, between randomly oriented plagioclase microlites. Titanite is common and shows groundmass-scale ophitic intergrowths with plagioclase in some places.

The northern outcrops of Alamo Creek Basalt appear to represent parts of a flow that filled a wide paleochannel. The western margin, although largely obscured by cover, is likely

truncated by a fault, as discussed above (Fig. 13). Also near the western margin, the edge of the paleochannel is present in the most southern outcrop of the basalt at point 5 in Plate I (Fig. 16). Moving eastward from this point towards the center of the basalt outcrop around sample site JH-63, the flow is up to ~ 5 m thick and displays undulatory columnar jointing (Fig. 14), then gradually thins eastward until it pinches out completely at the eastern margin (point 6 in Plate I). This eastern margin also shows flow breccia at the top of the basalt (discussed in full below). These two observations allow the inference that the eastern margin is the edge of the original lava flow, not an erosional margin. The northern margin of the outcrop exposes the base of the flow on the west and the top of the flow on the east (Plate I). Just south of sample site JH-63, the basalt appears to descend into the subsurface, below Chisos strata and Type III intrusive rock. Although the exact orientation of the axis of the large paleochannel filled by the lava is unknown due to limited exposure, the channel most likely runs approximately north-south.

The southern outcrops of Alamo Creek Basalt reinforce this idea of a large paleochannel. The eastern margin of the larger of the two southern basalt outcrop areas is bounded by the eastern fault (discussed in Chapter 3), has an erosional margin to the south, is truncated by Type III intrusive rock on the west, and runs into the subsurface to the north. But it is the profile of this larger outcrop area that is of interest for the paleochannel interpretation. Figure 17 looks north-northeast into a modern drainage channel from point 7 in Plate I, with basalt lower on the west than on the east. This is inferred to be a paleochannel, similar to the large paleochannel to the north: on the west, the base of the paleochannel is now the base of the hill on the left side of the figure; the sloping margin to the paleochannel has been eroded away by the current drainage channel; and to the east, on the right side of the figure, the structurally higher basalt outcrop is inferred to be a shallow portion of the paleochannel or perhaps the bank of the paleochannel. The

smaller of the two southern basalt outcrop areas is bounded solely by erosional contacts, and appears to be a continuation of the higher portions of the basalt lava exposed to the north. The simplest explanation of these two basalt-filled paleochannels is that they are two parts of the same ancient streambed, which may have meandered through the study area. Of course, this theory cannot be proven. In any case, the previously mentioned idea that the Alamo Creek Basalt Member of the Chisos Formation unconformably overlies eroded Black Peaks strata is borne out in the study area.

Flow breccia is found at the base and top of the lava (Fig. 18). The breccia at the base is typically 1 to 1.5 m thick and is highly irregular with fluidal to blocky lava clasts ranging from sparsely vesicular to scoriaceous. Like the rest of the lava, much of the flow breccia is overprinted with spheroidal weathering, which creates a deceiving appearance of pillows or pahoehoe toes in some places. Spaces between the breccia clasts are generally filled with calcite crystals and pale yellow to grey authigenic clay. A zone of high vesicularity up to ~1 m thick is present above the flow breccia. In some areas at the base of the flow, loading has generated slight undulations in the contact with the underlying mudstone. A chilled margin a few centimeters thick is seen where not obscured by weathering, and some degree of baking of the underlying mudstone is commonly seen (Fig. 18). The contact between the flow breccia and the underlying Black Peaks or Chisos strata is generally fairly sharp, with slight mixing of basalt fragments (< 1 cm in length) with only the first few centimeters of the underlying sediment. In some areas, the flow breccia grades into zones of peperite, where clasts of vesicular basalt, both fluid and angular, are mixed with baked-looking pale grey mudstone (Fig. 19). Flow breccia at the top of the flow is underlain in some places by a zone of basalt containing up to 50% vesicles. However, in some areas the top of the flow is devoid of breccia, and instead the zone of high

vesicularity is capped by ropy pahoehoe-like surface features, suggesting that the lava in this area was just beginning to develop flow breccia.

The top of the basalt lava in the northern outcrop area is overlain by a conglomeratic sandstone bed within the Chisos Formation (Fig. 16). This distinctive bed was important in distinguishing the Alamo Creek Basalt from Type III intrusive rocks during the initial fieldwork. In some places, clasts from this sedimentary unit occur within the flow breccia at the top of the lava (Fig. 20) and are interpreted to have fallen into the exposed cracks of the breccia when the conglomeratic sandstone was deposited.

A peculiar outcrop ~ 2 m across, which resembles vent-fill material, occurs within the Alamo Creek Basalt at point 8 in Plate I (Fig. 21). The breccia differs from the vent-fill material described below in several ways: the basalt clasts show a narrow range of vesicularity, display no obviously fluidal pyroclasts, and all of the clasts are lithologically identical to the adjacent lava. The matrix is yellow to grey disaggregated mudstone, and in some areas (Fig. 21) interstices between clasts are lined by chocolate-brown botryoidal chalcedony. We interpret this area of breccia to be a spiracle which formed as the lava flowed over a pocket of water, causing the water to flash to steam, puncturing the lava and producing a discordant mass of disaggregated basalt and sediment within the lava flow.

A large outcrop of Alamo Creek Basalt is exposed on the southern wall of a large modern drainage channel, just outside the southern margin of the study area (Fig. 22). This outcrop, in the cutbank of the large drainage, provides an excellent example of the columnar jointing which is generally obscured to various degrees by spheroidal weathering throughout the study area. The outcrop is also illustrative because it shows a less-weathered version of the basalt, with only minor amounts of green and brown smectitic clay altering the groundmass olivine (Fig. 23).

Interestingly, this outcrop is heavily weathered in the top 2-3 m, above a sharp contact. This contact is interpreted to mark an older weathering profile exposed by erosion.



Figure 14. Thickest part of northern Alamo Creek Basalt outcrop. Top part of this outcrop shows heavy spheroidal weathering; lower part of outcrops shows undulatory columnar jointing. Walking stick for scale.

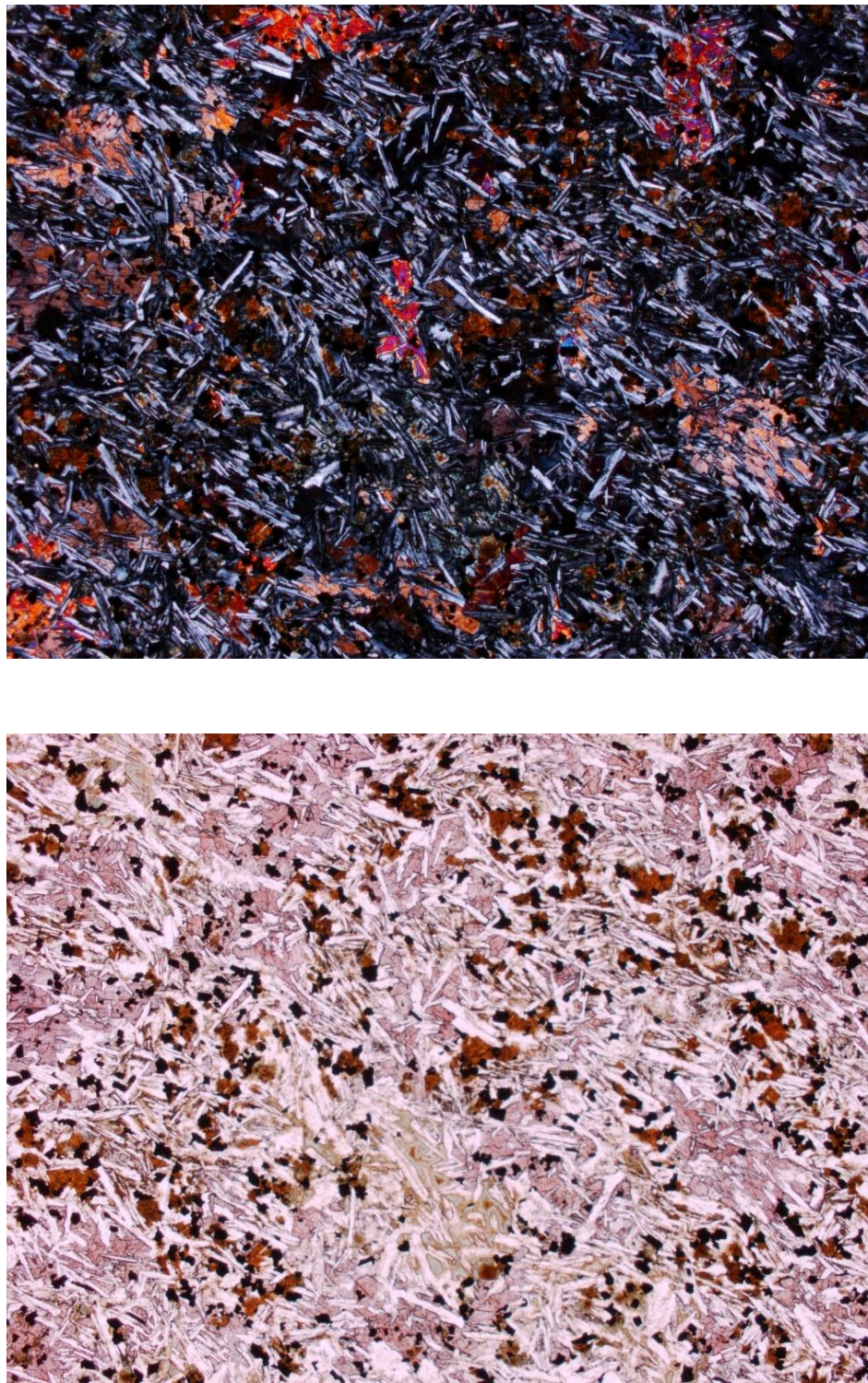


Figure 15. Photomicrograph of thin section from northern Alamo Creek Basalt in plane light (left) and crossed polars (right). Vertical dimension is 5 mm. Note altered olivine between plagioclase microlites in left view. Ophitic titanite has pale purple color in left view and bright interference colors in right view.

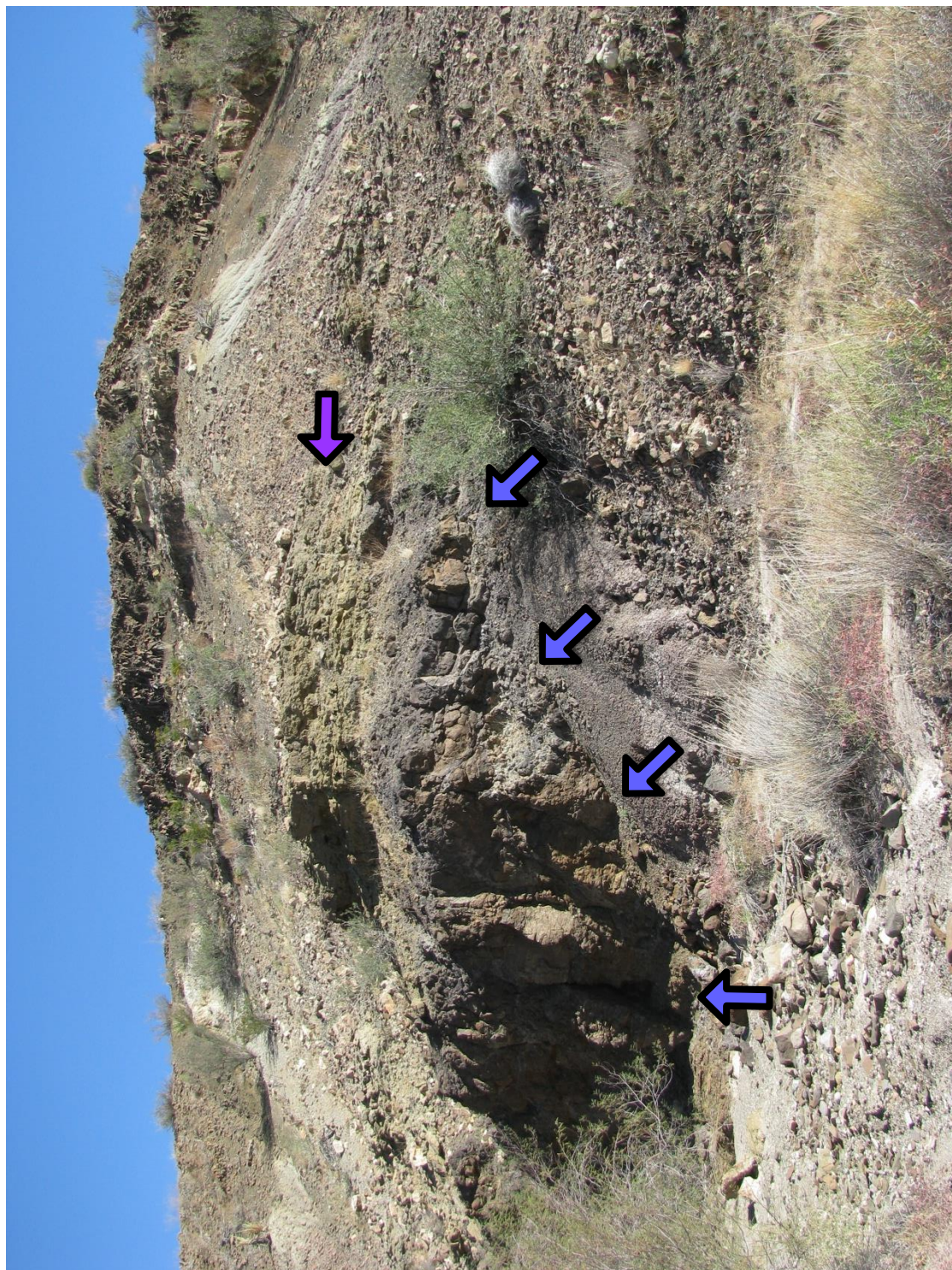


Figure 16. View of Alamo Creek Basalt filling paleochannel (blue arrows) with Black Peaks strata forming the paleochannel margin (arrowed) in foreground. Chisos conglomeratic sandstone (purple arrow) overlies Alamo Creek Basalt, and Type III diabase is present at top of the hill. For scale, plant to right of paleochannel is ~ 1 m wide. Image from point 6 in Plate I.

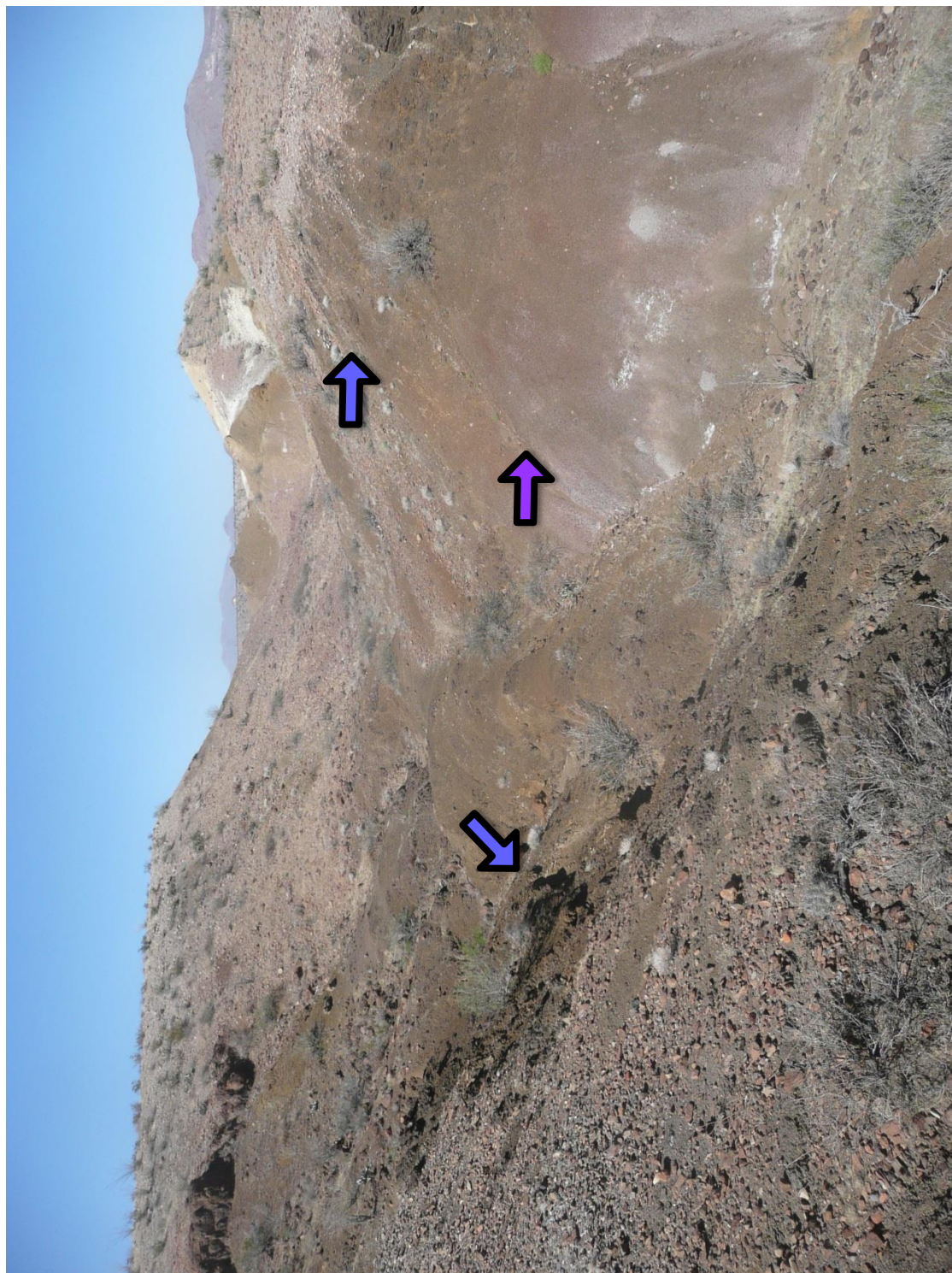


Figure 17. Alamo Creek Basalt in the southern outcrop, filling a paleochannel. Basalt outcrop at the base of the hill on the left (blue arrow on left) and structurally higher basalt (blue arrow on right) overlying reddish-purple Black Peaks strata (purple arrow). View looking north-northeast; arrowed plant is ~ 0.5 m across. Image of point 7 in Plate I.



Figure 18. Flow breccia at base of northern outcrop of Alamo Creek Basalt (overprinted by spheroidal weathering). Note baked margin of underlying Chisos mudstone in first few centimeters below contact. Hammer for scale (arrowed), against white Chisos strata at base of outcrop.



Figure 19. Peperite at base of northern outcrop of Alamo Creek Basalt. Sediment mixed with basalt is light yellow in color. Pencils for scale.



Figure 20. Chisos conglomeratic sandstone (yellow) overlying and filling cracks within flow breccia at the upper margin of the northern outcrop of Alamo Creek Basalt. Pencil for scale.



Figure 21. View of part of spiracle within southern outcrop of Alamo Creek Basalt. Basalt clasts are mixed with lighter colored sediment. Chocolate-brown chalcidony is arrowed. Pencil for scale.



Figure 22. Alamo Creek Basalt outcrop just south of the study area. Note undulatory columnar jointing of basalt. Silver and red walking stick for scale at base of foremost outcrop.

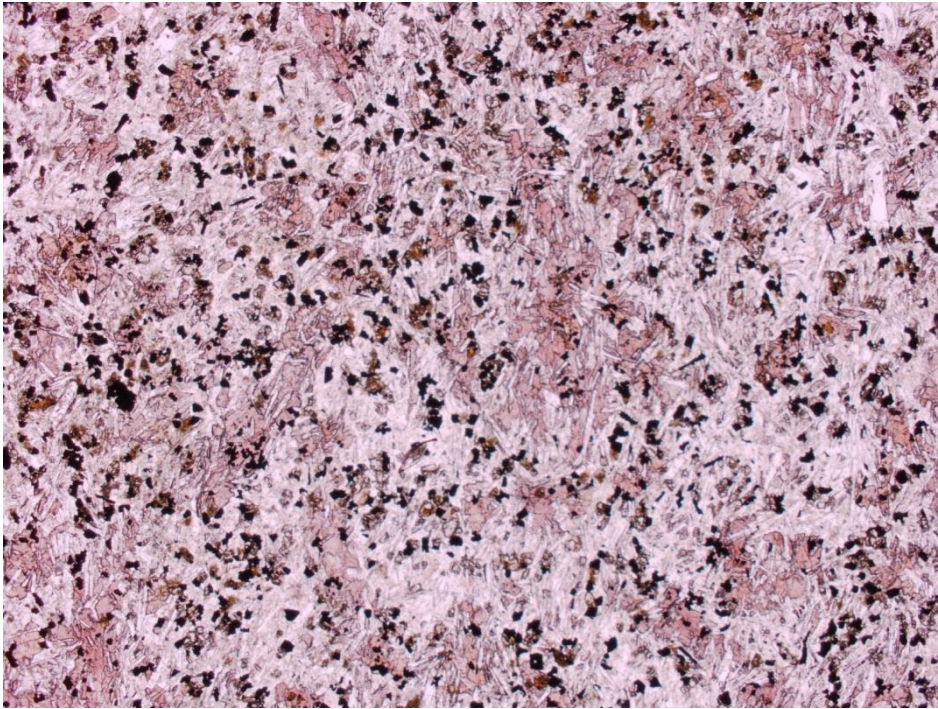


Figure 23. Photomicrograph of thin section from southern outcrop of Alamo Creek Basalt in plane light and crossed polars. Note lack of alteration seen in Figure 14. Ophitic titanaugite has pale purple color in left view and bright interference colors in right view.

Phreatomagmatic Vents

Vent-fill material was found in seven separate outcrops throughout the study area (labeled A through G on Plate I). The margins of the vent-fill outcrops are most commonly delineated by contacts with an intrusive body, although some outcrops disappear beneath recent colluviums (not depicted in Plate I). Across the study area, most of the vent-fill outcrops bear similar characteristics, and thus are discussed collectively. In a few cases, an outcrop displays a unique feature that is discussed separately.

A typical exposure of vent-fill material consists of a complex mixture of basalt and sediment (Fig. 24, 25, 26). The sediment is generally composed of Chisos mudstone and/or tuffaceous mudstone that is commonly white, grey, or yellow. The yellow hue in some outcrops is likely either an effect of alteration of the sediment during formation of the vents or reflects incorporation of sediment from strata other than those within the Chisos Formation exposed in the study area, which are only white and grey. The sediment has commonly undergone some degree of baking, and in some cases forms discrete chunks, although this feature is more commonly seen in tuff-rich or mud-rich areas of sediment (Fig. 27). In thin section, the sediment shows a range of textures, from highly fluidal interactions with the basalt clasts (Fig. 28), to smaller amounts of sediment which appears to have contracted as the slurry cooled (Fig. 29). The abundance of sediment within the vent-fill material suggests creation by subsurface explosions generated by the interactions of groundwater-rich sediment and intruding magma, rather than by extrusion of magma into a body of water, which would produce deposits with less sediment and more basalt showing quench fragmentation.

Basalt clasts in the vent-fill show a large variety of characteristics. Vesicularity ranges from nonvesicular to scoriaceous (Fig. 24, 25, 26, 27, 30, 31, 32). Margins of the basalt clasts

range from fluidal to angular (Fig. 24, 25, 27, 28, 33). Some exposures even show jigsaw texture, where a clast was frozen as it was breaking apart (Fig. 34). Accretionary ash particles are common, with structures similar to accretionary lapilli (Fig. 35). Ash-sized lithic clasts akin to armored lapilli are also common (Fig. 35). Clasts of tachylite are also seen in some vent-fill outcrops (Fig. 32) The basalt clasts vary in size from shards < 1 mm across (Fig. 25, 31, 33), to bombs that range up to 1 m but more are commonly 20 to 50 cm in length (Fig. 36). Some of these bombs have highly vesicular rims and nonvesicular cores, and some of the pyroclasts show a chilled margin (Fig. 37). In outcrops D and G, isolated pieces of spatter and clasts of agglutinate are found (Fig. 38, 39). Collectively, these observations indicate that the pyroclastic material filled vents that fed explosive eruptions. The features of the basalt pyroclasts, the abundance of intermixed sediment, and the presence of accretionary and armored particles indicate an origin by explosive phreatomagmatic processes.

The margins of the vent-fill outcrops are almost exclusively bordered by intrusive basalt or diabase. In most outcrops, the vent-fill material is surrounded on all sides by Type III intrusive rock, and in some cases tongues of Type III intrude the vent fill. At outcrops D, E, and G, the base of the exposed vent-fill material is intruded in places by Type I basalt or diabase. The significance of these intrusive relationships will be discussed in Chapter 6.

In vent-fill outcrop D, two distinct types of vent-fill material have been distinguished, one basalt-rich and one sediment-rich. The basalt-rich type (Fig. 40, 41) is composed almost entirely of basalt clasts, which range from nonvesicular to scoriaceous and are generally fluidal in shape, although some clasts appear to be shattered fragments of larger fluidal bombs. The largest basalt-rich mass is ~ 10 m across, but most are 0.5 to 1 m across. These basalt-rich masses are set within more sediment-rich material, which is comparable to the typical vent-fill

material found in the other vents in the study area, although it contains more bombs (Fig. 42, 43). The contacts between the two types of material, where exposed, are steeply inclined ($\sim 60^\circ$) to subvertical. The sediment-rich material penetrates up to 15 cm into the basalt-rich material as tendrils or blunt injections (Fig. 44). Following McClintock and White (2006) and Ross and White (2006), the basalt-rich masses are interpreted to be discrete debris jets that formed during repeated phreatomagmatic explosions in heterogeneous vent fill, as discussed in Chapter 1.



Figure 24. Vent-fill material with light colored sediment matrix. Note range in vesicularity and fluidal contacts between basalt clasts and sediment matrix. Image from outcrop C in Plate I. Pencil for scale.

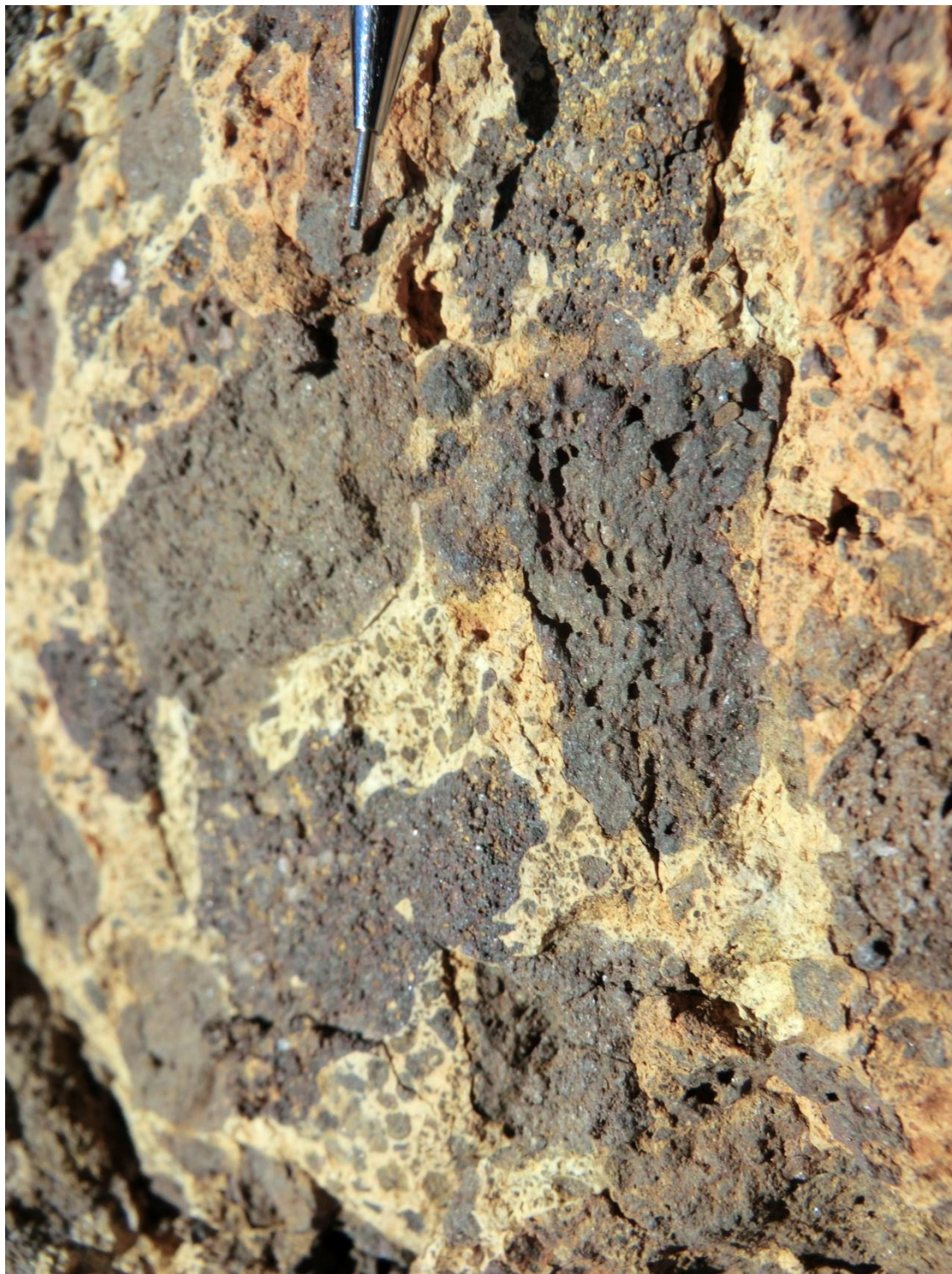


Figure 25. Close up view of sample in Figure 24. Note small basalt clasts in sediment matrix. Image from outcrop C on Plate I. Pencil for scale.

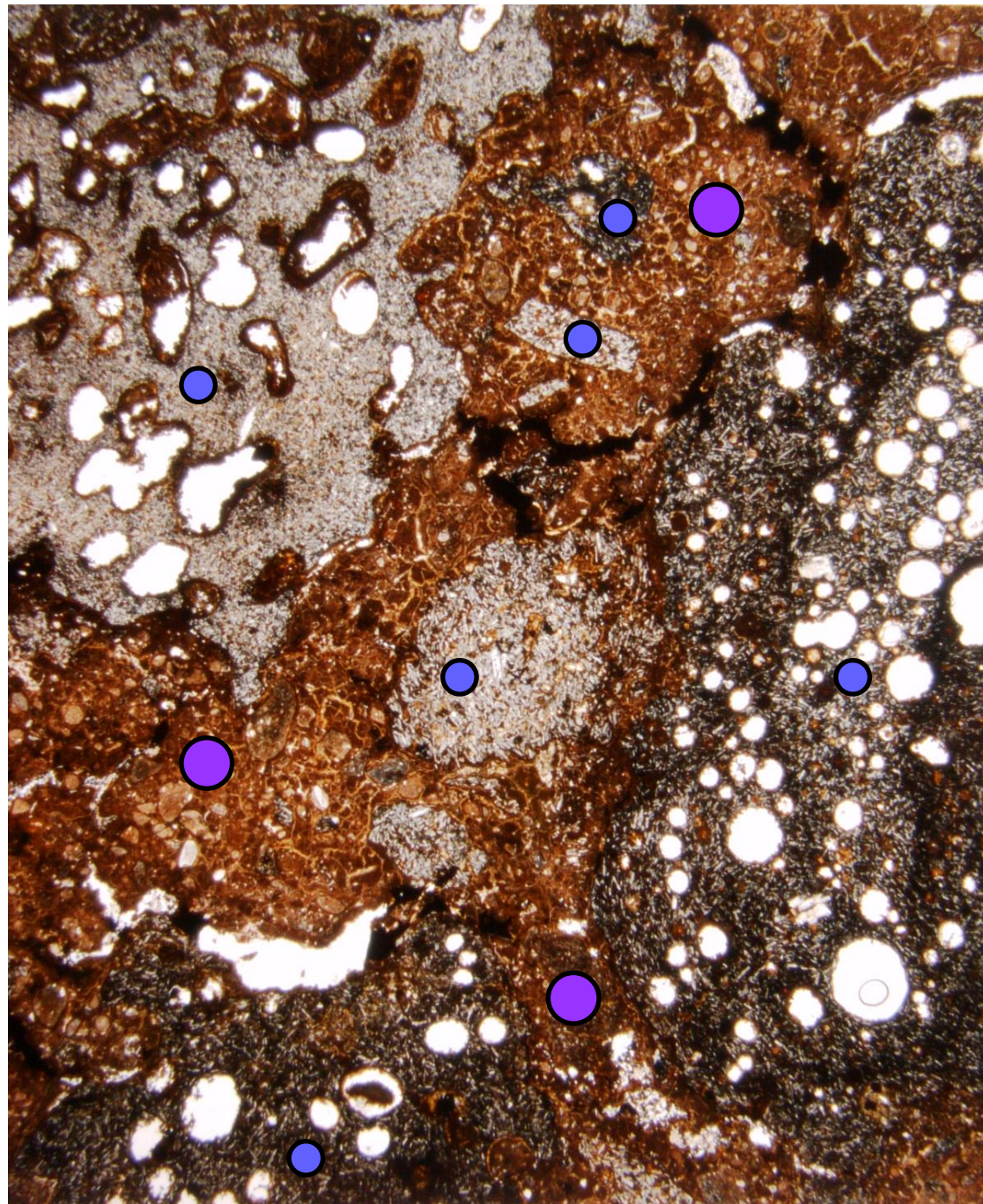


Figure 26. Photomicrograph showing typical vent-fill material, with basalt clasts of varying vesicularity and grain size, mixed with sediment. Basalt (small blue circles) and sediment (larger purple circles) are identified for reference only in this photomicrograph. Sample from outcrop B on Plate I. Plane light; field of view is 22 mm across.



Figure 27. Slab of vent fill. Note cream-colored chunks of tuffaceous material in contrast to pale grey chunks of mud. Also note fluidal margins and range in vesicularity of basalt clasts. Sample from outcrop B in Plate I.



Figure 28. Photomicrograph showing fluid contacts between basalt and sediment. Note sediment filling vesicles in basalt clasts. Sample from outcrop E in Plate I. Plane light; field of view is 22 mm across.



Figure 29. Photomicrograph showing sediment filling vesicles within and space between basalt clasts. Sediment is very fine-grained and is fragmented, possibly due to contraction during cooling and dewatering. Sample from outcrop D in Plate I. Plane light; field of view is 22 mm across.



Figure 30. Slab of vent fill with basalt pyroclasts showing a range in vesicularity. Also note mud with contraction cracks in upper right portion of slab. Sample from outcrop B in Plate I.



Figure 31. Range in vesicularity of basalt pyroclasts in vent-fill outcrop. Also note small size of some basalt clasts. Image from outcrop B in Plate I. Pencil for scale.

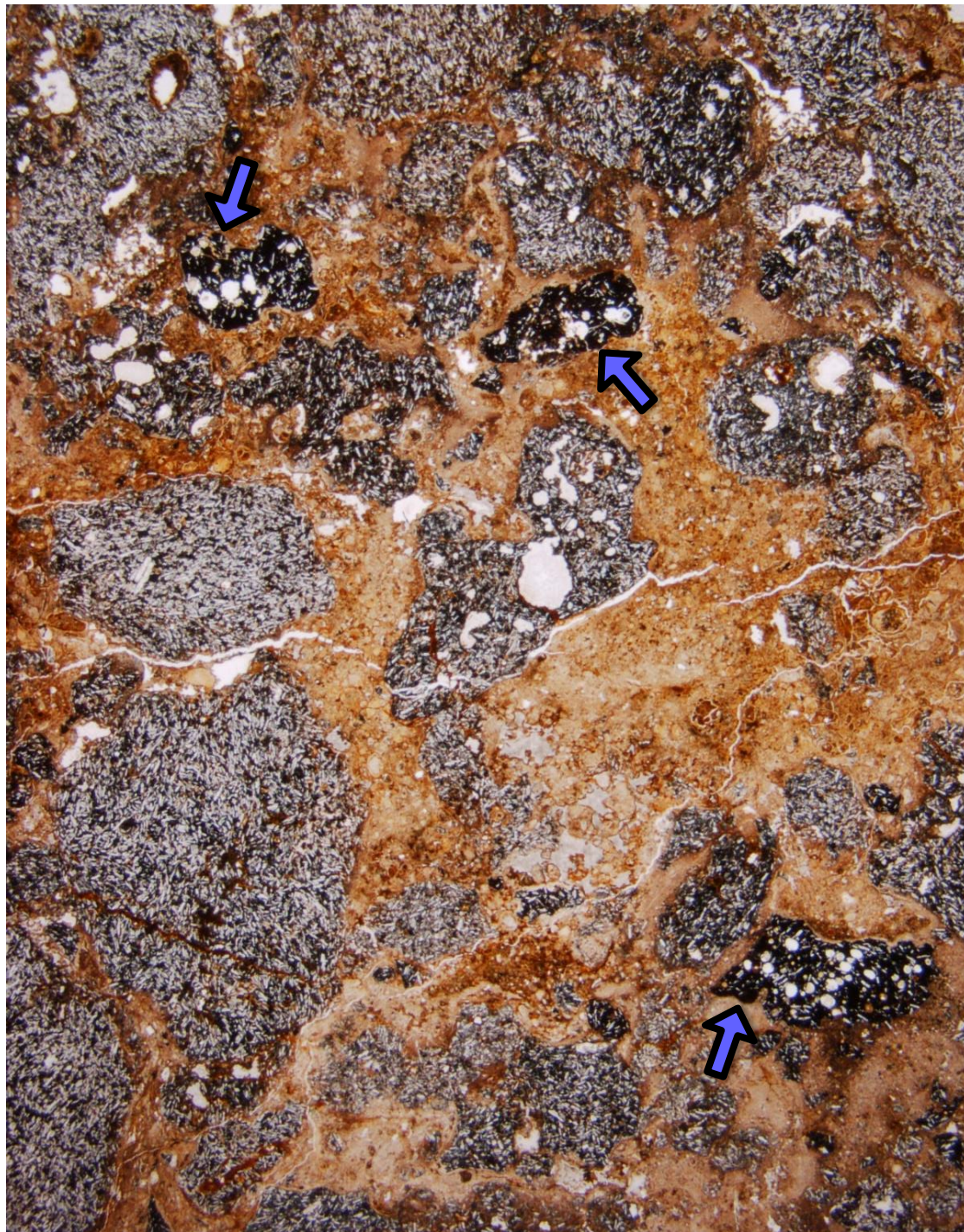


Figure 32. Photomicrograph showing tachylite clasts (blue arrows) with a high degree of vesicularity within vent fill. Sample from outcrop B in Plate I. Plane light; view is 22 mm across.



Figure 33. Angular clasts of basalt in vent-fill sample. Note range in vesicularity of basalt clasts. Image from outcrop E in Plate I. Pencil for scale.



Figure 34. Jigsaw texture of basalt clast fragments (examples are arrowed). Also note lapilli-sized basalt clast with high vesicularity. Image from outcrop G in Plate I. Pencil for scale.

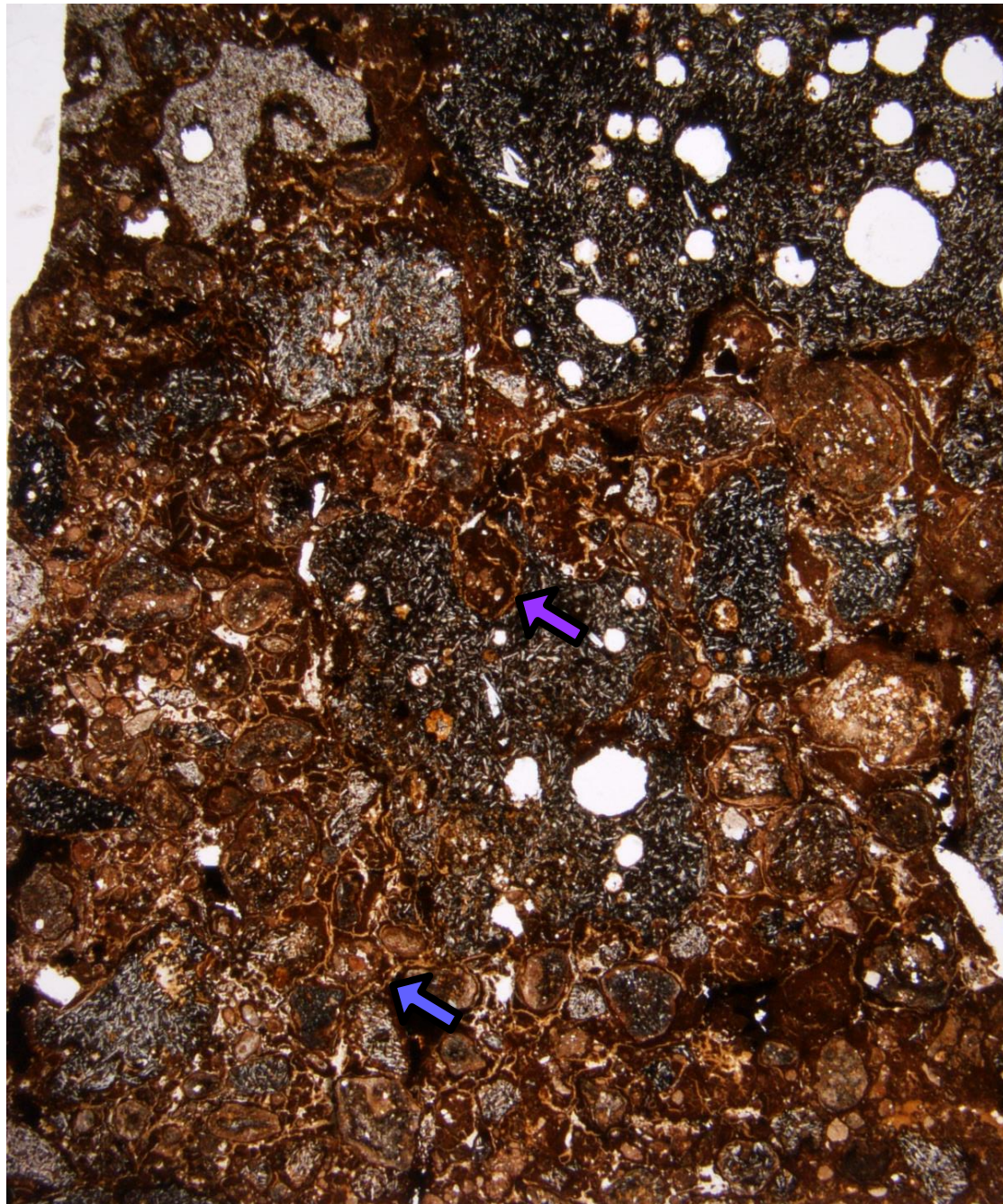


Figure 35. Photomicrograph showing armored (blue arrow) and accretionary ash-sized particles (purple arrow). Sample is from outcrop B in Plate I. Plane light; view is 22 mm across.



Figure 36. Large basaltic bomb within vent-fill outcrop D. Carbonate-filled amygdules are visible in bomb. Less altered portions of this bomb were taken for geochemical sample JH-27. Pencil for scale.



Figure 37. Slab of vent fill showing darker chilled margin (arrowed) of basaltic pyroclast in center of slab. Sample from outcrop B in Plate I.



Figure 38. Darker, fluidal outlines of grey basalt spatter within pale yellow sediment in vent fill. Image from outcrop G in Plate I. Pencil for scale.

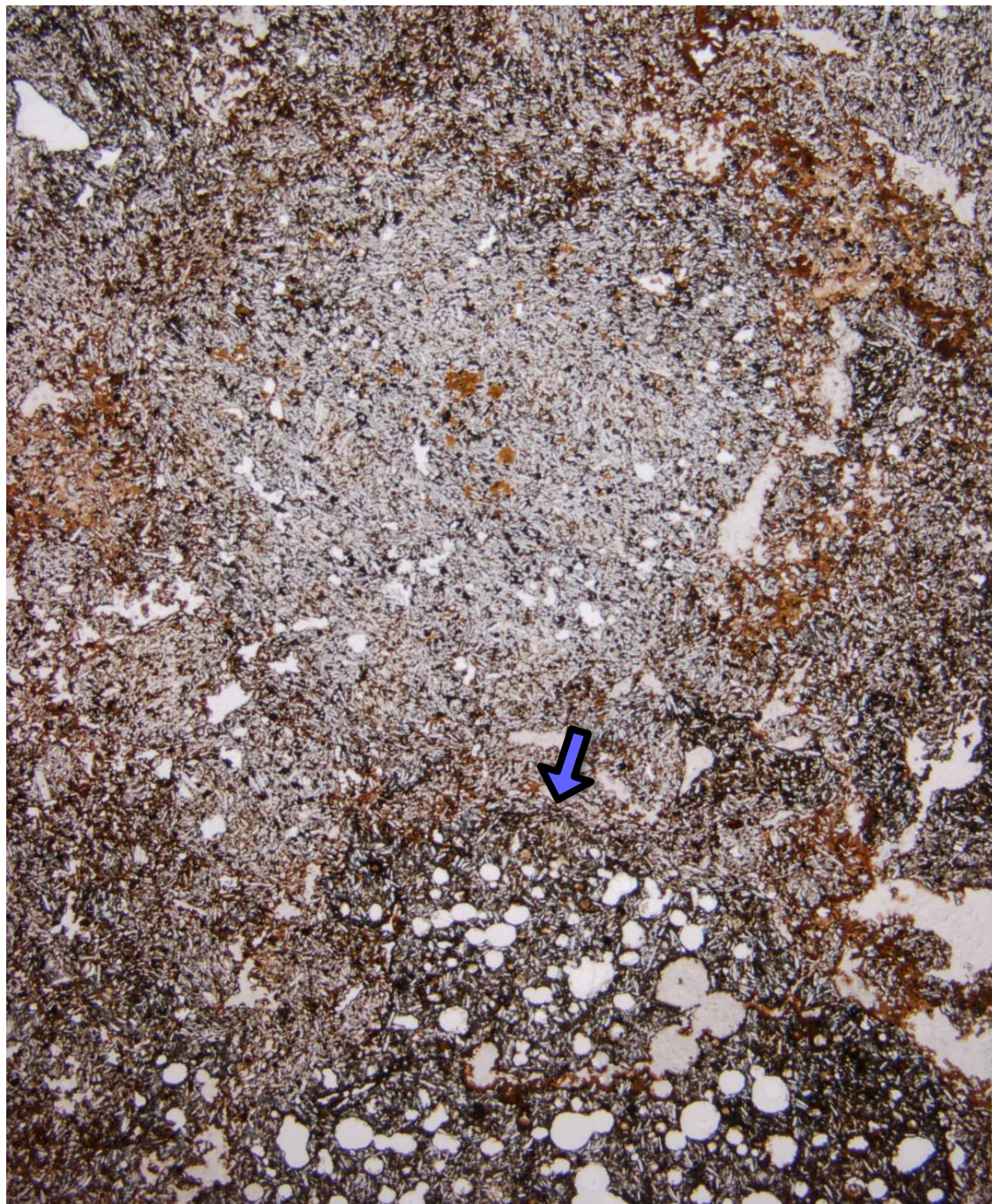


Figure 39. Photomicrograph showing indistinct margins between spatter pieces in mass of agglutinate. Blue arrow points to one margin, which is defined by tan sediment trapped between spatter pieces. Sample from outcrop D in Plate I. Plane light; field of view is 22 mm across.



Figure 40. Basalt-rich debris jet in vent-fill outcrop D. Note fluidal shapes of many of the clasts. Image from outcrop D in Plate I. Pencil for scale.



Figure 41. Agglutinate sample from basalt-rich debris jet. Different clasts are best distinguished by areas of different vesicularities. Sample from outcrop D in Plate I.



Figure 42. Sediment-rich debris jet in vent-fill outcrop D. Pencil for scale. Note bomb at tip of pencil.



Figure 43. Hand sample from sediment-rich debris jet. Note similarity to other vent-fill samples. Sample from outcrop D in Plate I.



Figure 44. Contact (arrowed) between basalt-rich debris jet at base of outcrop (behind pencil) and sediment-rich debris jet at top of picture. Note irregular contact between the two jets, with protrusion of sediment-rich material into basalt-rich material. Image from outcrop D in Plate I. Pencil for scale.

Hypabyssal Intrusions

The area east of Peña Mountain is dominated by hypabyssal mafic intrusions (Fig. 45). These intrusions have been divided into three types, based initially on study of phenocryst contents in hand sample in the field and later confirmed by petrographic examination and geochemistry. All three types are diabase which grades into basalt along intrusive margins or in small tongues which cooled more quickly. Each unit shows billowed margins against host sedimentary strata.

Type I

Only one Type I intrusion is shown in Plate I and occurs along the western margin of the intrusive complex, near vent-fill outcrop A. Type 1 intrusions were also found in three other locations (discussed below), but not in quantities large enough to be shown at the scale of Plate I. The eastern and upper margins of the main outcrop form intrusive contacts against Chisos strata. The northern and southern margins are presumed to be intrusive contacts against Type III, but lack of outcrop made it impossible to determine the exact nature and location of these contacts. The western margin is complicated by the regional fault in this part of the study area. Along most of the fault in this area, Black Peaks strata on the western block are juxtaposed against Type I on the eastern block. In some areas, Type I has intrusive contacts against Black Peaks strata. Along the fault, Type I shows fault breccia and slickenlines. However, in one location Type I is seen on both sides of the fault, although it is quite limited in extent in the western block (Plate I).

In the field, Type I is generally relatively massive diabase. In hand sample, fresh microphenocrysts of plagioclase (< 1 mm) are quite common. Altered olivine microphenocrysts of the same size and larger phenocrysts of plagioclase (~ 5 mm) occur in much smaller amounts. Sparse amygdules (< 5 mm) filled with carbonate are also present. In thin section (Fig. 46), slight

flow alignment of fresh plagioclase microlites is seen, olivine in the groundmass is altered to green smectitic clay, and fresh titanite is present. Thus, petrologically, Type I is virtually identical to the Alamo Creek Basalt.

The Type I diabase develops chilled margins and billows at its lower contact with Black Peaks strata on the western block of the fault, and along its upper margin with Chisos deposits on the east side of the fault. The chilled margin grades from diabase to a zone of aphanitic basalt several centimeters thick with common small vesicles. The intrusion baked the Chisos sediment at its upper contact, creating small-scale columnar jointing in the sediment, virtually identical to the baking of the same layer of Chisos sediment against the Type III intrusion a short way up the hill (see Fig. 56 in the section on Type III).

The three small outcrops of Type I occur in the area south of the main transecting drainage (Plate I). The southernmost outcrop is in a drainage at point 10 in Plate I. Here, Type I forms an intrusive basalt tongue ~ 2 m across, with a chilled margin (Fig. 47). The chilled, billowed margin is aphanitic, < 4 cm thick, nonvesicular, and has a yellowish tan surface that could represent altered palagonite. This chilled margin is in contact with both Alamo Creek Basalt and Black Peaks mudstone, indicating that the Type I intrusion is younger than the basalt lava.

The other two outcrops of Type I occur in the lower parts of vent-fill outcrops D and G (Fig. 48). In both areas, the contacts between the intrusions and vent-fill material lack any evidence of explosive activity, but still maintain fluidal margins against the vent fill. Thus, Type I is inferred to have been emplaced after explosivity ceased but before the vent-fill material lithified.



Figure 45. View of entire hypabyssal intrusive complex looking west-southwest from point 9 on Plate I. Note pale grey and white of Chisos strata surrounding dark brown diabase intrusions. Left arrow points to southernmost Type III exposure; right arrow points to northernmost Type III exposure. Santa Elena Canyon on horizon in center of image, with Peña Mountain in background on right side of image.

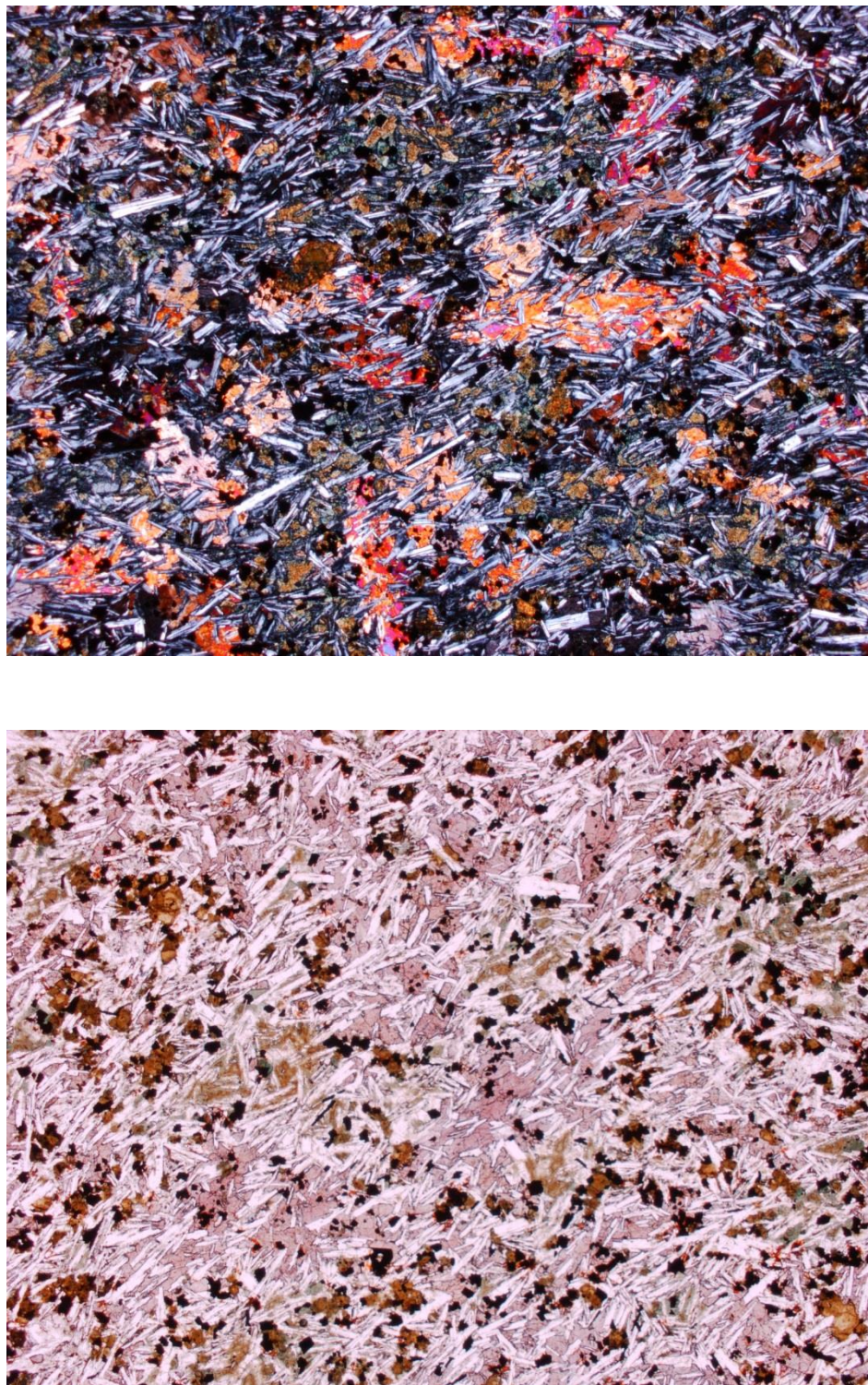


Figure 46. Photomicrographs of thin section from main Type I intrusion in plane light (left) and crossed polars (right). Vertical dimension is 5 mm. Note purple color of titanaugite in plane light and lack of any large phenocrysts.

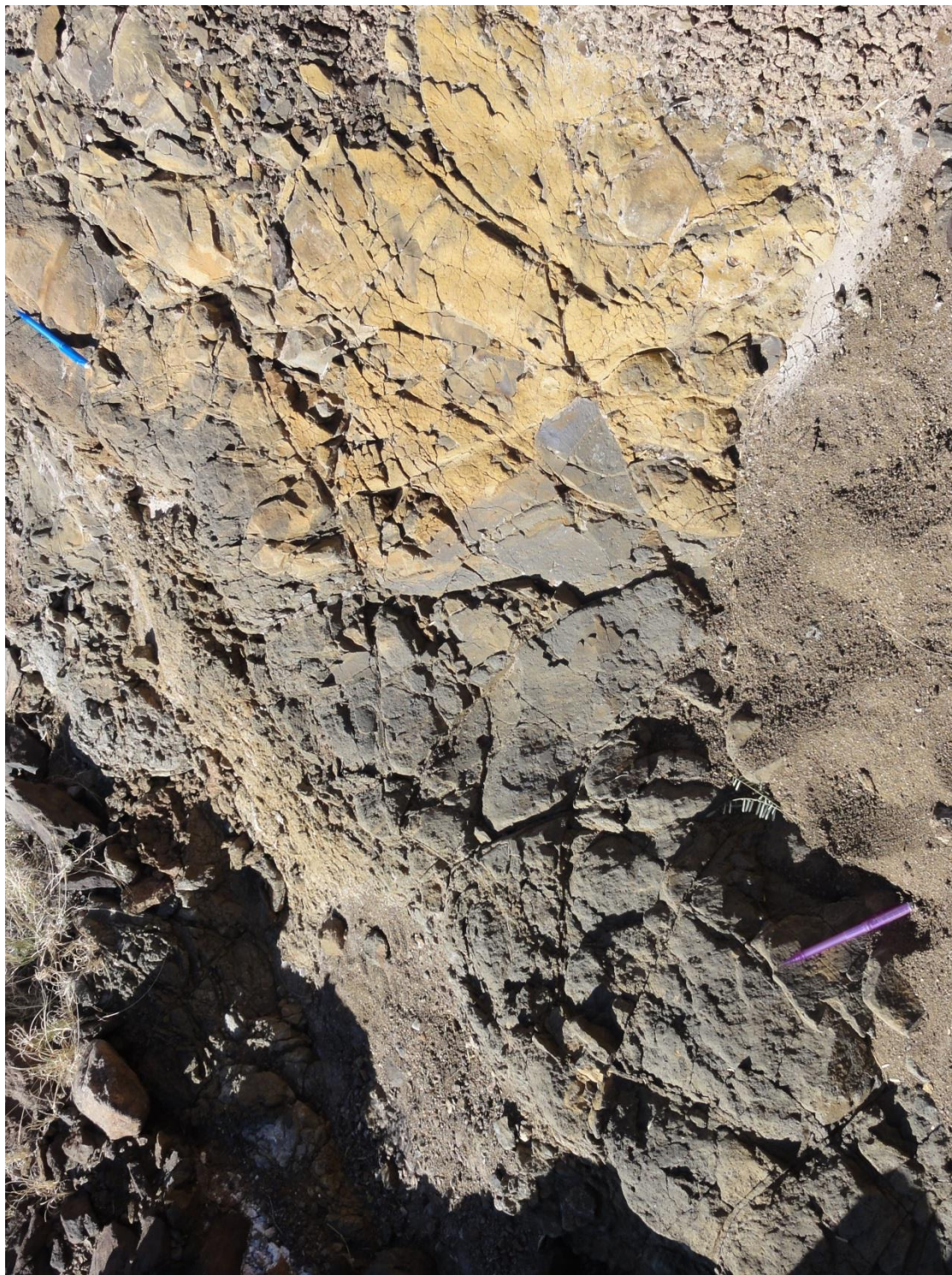


Figure 47. View looking down on billowed surface of Type I intrusive diabase exposed by erosion in base of stream channel. Note tan color of chilled margin. Host reddish gray Black Peaks mudstone covers chilled margin of Type I in bottom right of view. Pencils for scale.



Figure 48. Vent fill material (outcrop D) at top of tower-like outcrop with Type I intrusion forming base of structure. Pen (blue and silver) for scale in location of Type I geochemical sample (JH-62).

Type II

Type II intrusive material was mapped in three areas in the southern portion of the study area (Plate I). Its margins are intrusive along all the mapped contacts except where Pleistocene pediment gravels rest depositionally on top of Type II.

Type II is a massive diabase with a distinctive phenocryst content. Type II commonly weathers to a pinkish-red color, but other mafic units in the study area also weather similarly in a few places. Amygdules (< 1 cm) are common near the Type II intrusive margins. Type II shows abundant (~25%) plagioclase phenocrysts (up to 1 cm), typically with a pink tint (Fig. 49 and 50), and much less abundant olivine and pyroxene phenocrysts (< 5 mm). In thin section (Fig. 51), the groundmass is intergranular with fresh plagioclase, relatively fresh pyroxene, and olivine altered to pale green clay and iron oxide. Olivine phenocrysts are altered to carbonate and plagioclase is partly altered to zeolite.

The contact between Type II and Type III in the northern outcrop of Type II is quite illustrative of the relationship between the two units (Fig. 49 and 50). Peperite is present between two billows of the Type II margin (Fig. 49), showing interaction between the intrusion and wet, unconsolidated sediment. The Type III material in this outcrop shows an excellent chilled margin with amygdules increasing towards the contact and a marked decrease in grain size from phaneritic diabase to aphanitic basalt at the margin. The Type II material shows no decrease in grain size towards the contact, but does show amygdules near the contact. Therefore, I infer this outcrop to be close to the original lower intrusive margin of Type II against host sedimentary strata. After Type II was intruded and cooled, Type III intruded along and chilled against the lower margin of the Type II intrusion.

The area mapped as Type III between two outcrops of Type II (point 11 in Plate I) displays a purple tone quite similar to the chilled margin of Type III, seen in Figures 49 and 50. Although we were unable to confirm this in the field, it seems likely that the area between these two outcrops of Type II exposes the upper chilled margin of the Type III intrusion, meaning the area was once capped by a continuous mass of Type II.

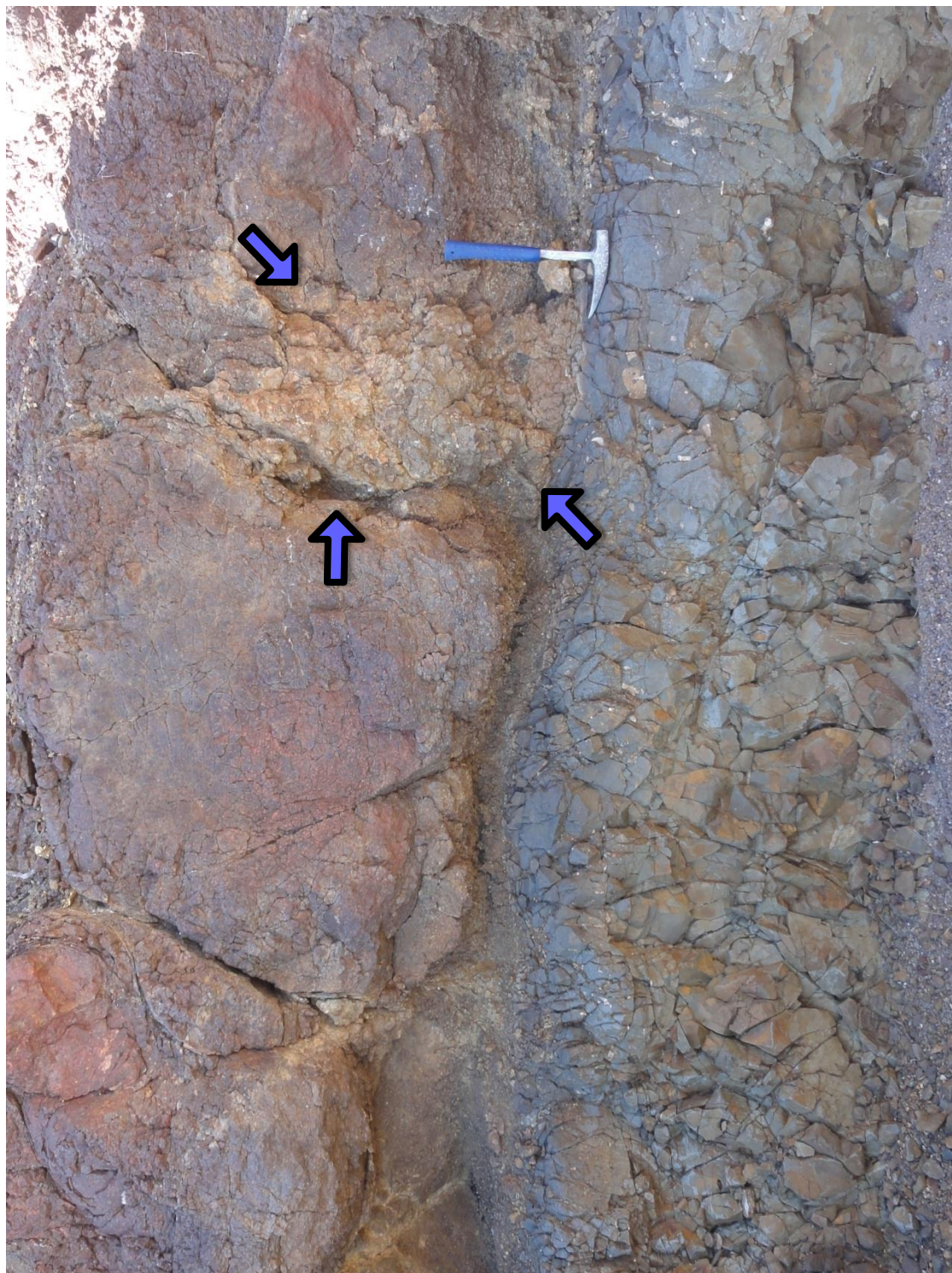


Figure 49. Contact between Type II intrusion (above) and Type III, which shows a distinct chilled margin against Type II. Note reddish hue and peperite (to left of hammer and within arrows; pale yellow sediment mixed with basalt clasts) along margin of Type II. Hammer for scale.

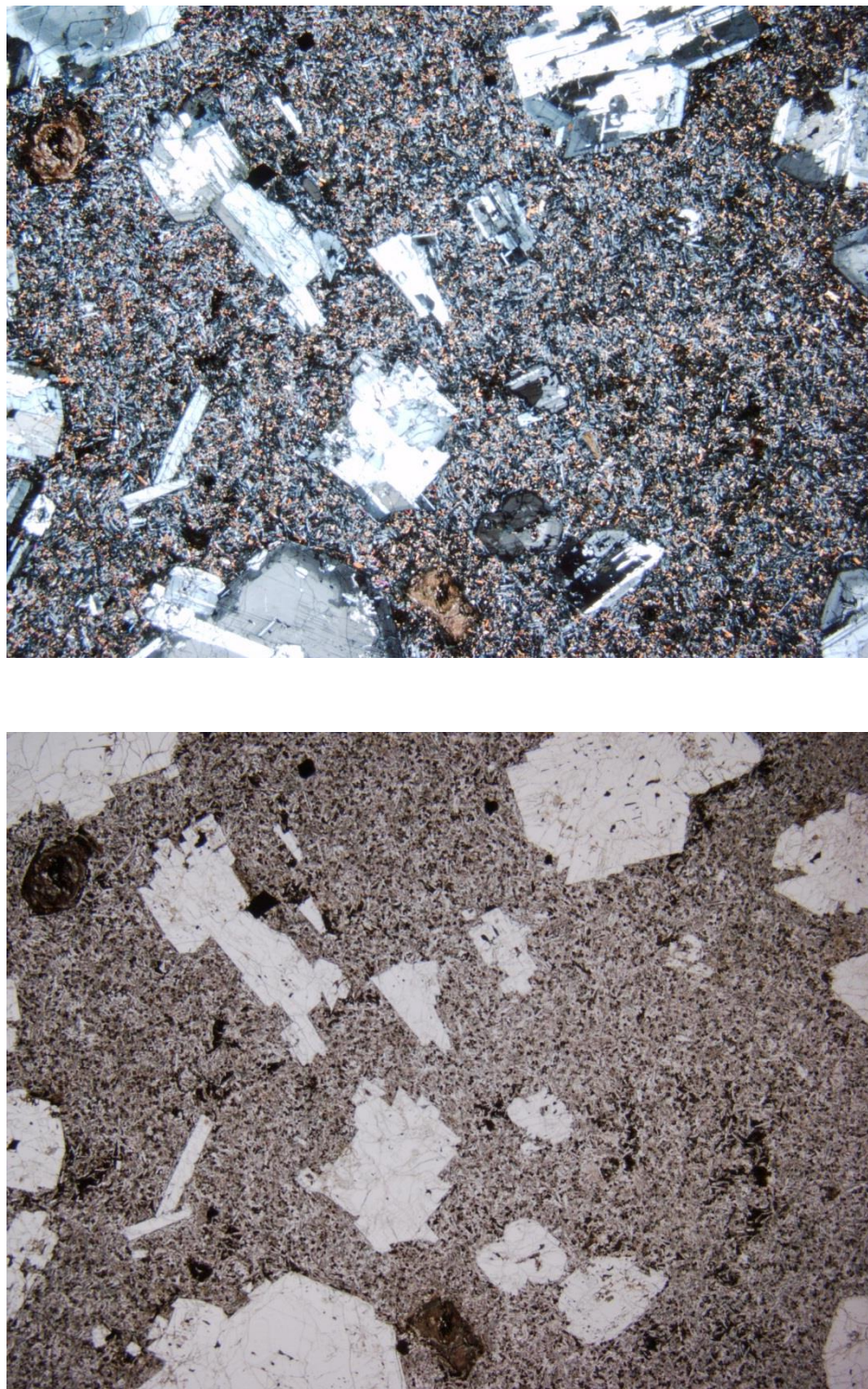


Figure 50. Photomicrographs of thin section from Type II intrusion in plane light (left) and crossed polars (right). Vertical dimension is 22 mm. Note large size of plagioclase phenocrysts in significantly wider view than other photomicrographs. Groundmass shows intergranular texture. Darker phenocrysts in left image are altered olivine.



Figure 51. Another view of reddish Type II contact with Type III. Note chilled margin of Type III against Type II. Hammer for scale.

Type III

Type III intrusive material has been mapped throughout the majority of the study area (Plate I). The margins of Type III are largely erosional and it typically crops out in the upper parts of the hills in the area. The contacts between Type III and all units except pediment gravel are intrusive, with Type III showing chilled margins against the other units (Fig. 52).

Type III is a relatively massive diabase with a distinct phenocryst content. The unit shows less abundant spheroidal weathering than Alamo Creek Basalt outcrops and in some outcrops shows platy jointing, spaced a few centimeters apart. Amygdules are relatively common, but are more typical near chilled margins, and pipe vesicles filled with carbonate occur in a few locations at the margins (Fig. 53). In hand sample, phenocrysts of fresh plagioclase (commonly < 3 mm, but in a few instances up to ~ 5 mm) occur in amounts of 5 to 7 %. Phenocrysts of fresh augite and olivine (~ 1.5 mm) commonly altered to iddingsite occur in amounts of ~ 1 %. Some outcrops show subophitic to ophitic texture, creating black spots < 5 mm across, and the ophitic texture shows up well in thin section (Fig. 54). Plagioclase phenocrysts in thin section show sieve texture with light alteration to calcite, olivine phenocrysts are generally altered to iddingsite or chlorophaeite with minor amounts of calcite, and minor alteration of groundmass olivine to iddingsite is present (Fig. 55). Away from the chilled margins, the groundmass is intergranular with magnetite, augite, and minor olivine altered to chlorophaeite in the interstices between plagioclase microlites.

Outcrops of Type III chilled margins are quite common and generally create dramatic contacts, as seen in Figure 53. The sediment against the contact is commonly baked, as seen in Chisos mudstone in Figure 56. The outermost edge of these margins is aphanitic and nonvesicular, and generally < 1 cm thick. Amygdules are fairly common just inside this

nonvesicular margin. One zone of peperite ~ 20 cm thick was found along a contact between Type III and Chisos mudstone, showing the sediment was locally wet enough to cause some quenching and disruption of the intruding magma. These chilled margins are especially distinct on the thinner Type III intrusive tongues, some of which are remarkably complex (Fig. 57, 58), and palagonite is present on the outer parts of some of the margins (Fig. 59, 60). The complexity of the intrusive relations, billowed margins, and formation of peperite and palagonite suggest that the Chisos Formation was poorly lithified and contained groundwater at the time that Type III was emplaced.

The contact between the Type II and Type III intrusions, as discussed previously, demonstrates that Type II is older than Type III. Type III is also found intruding into the Chisos conglomeratic sandstone which was deposited on top of the Alamo Creek Basalt. And finally, Type III is in direct contact with vent-fill material at outcrop A (Plate I). These relations indicate that Type III is the youngest unit in the study area, aside from Pleistocene pediment and Holocene alluvium.

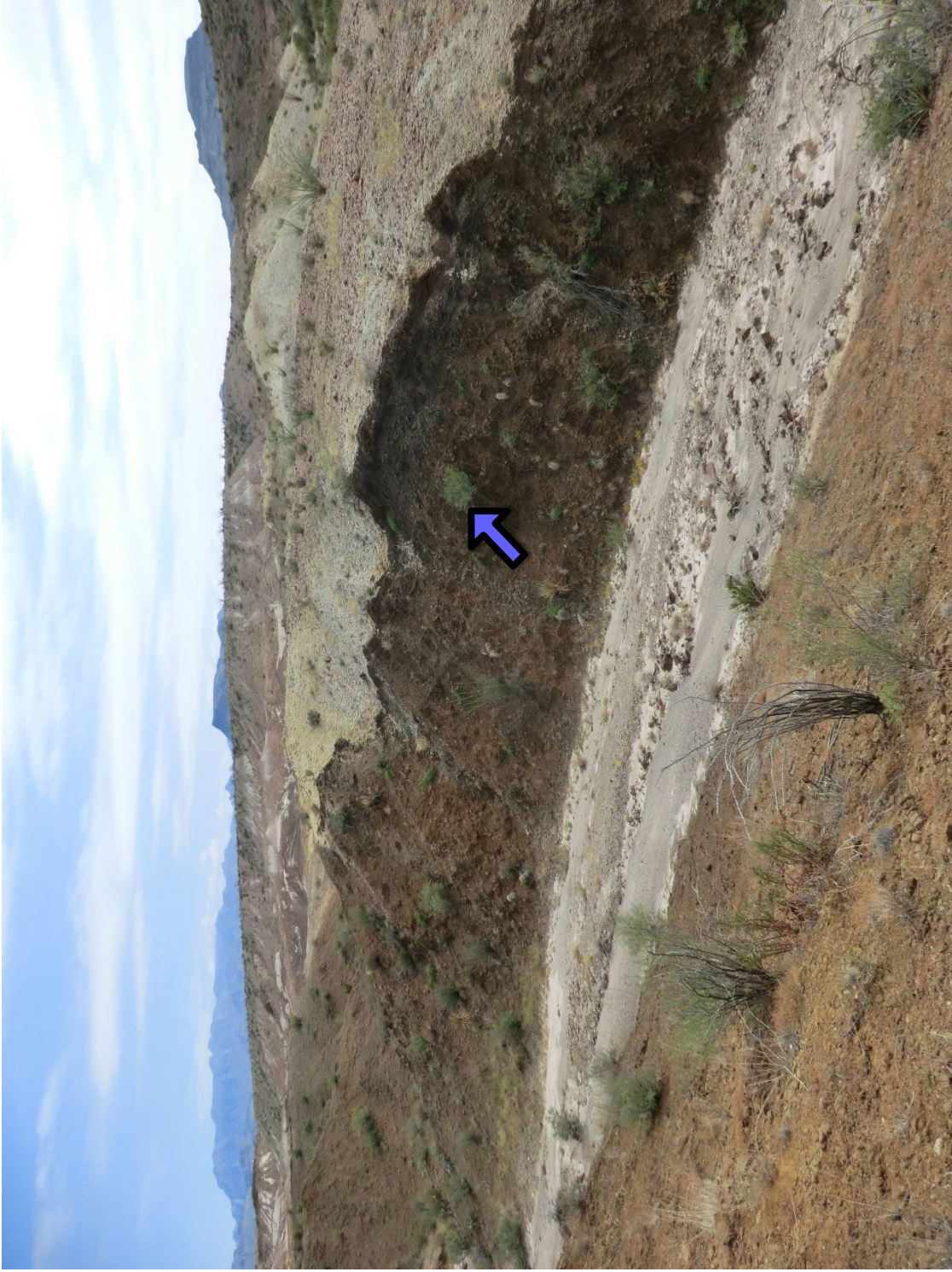


Figure 52. Billowed contact between dark brown Type III diabase and overlying pale grey and white Chisos strata. Type III is also in foreground, although with a different weathering pattern. Arrowed plant is ~ 0.5 m across.



Figure 53. Contact between dark brown Type III intrusion and overlying pale gray-to-white Chisos mudstone. Note pipe vesicles filled with carbonate. Pen and hammer for scale.

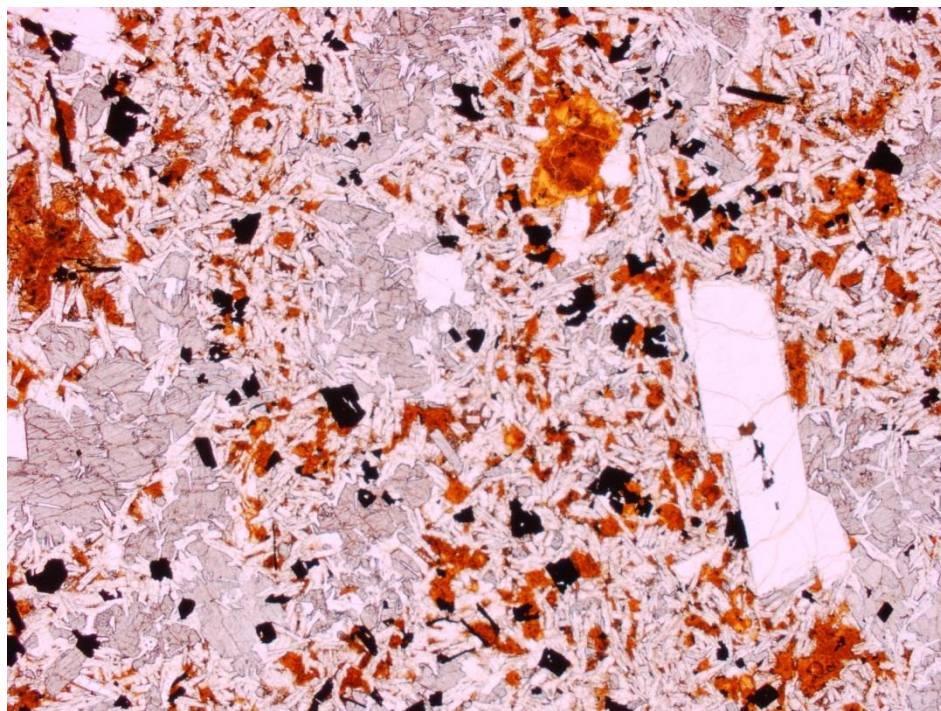
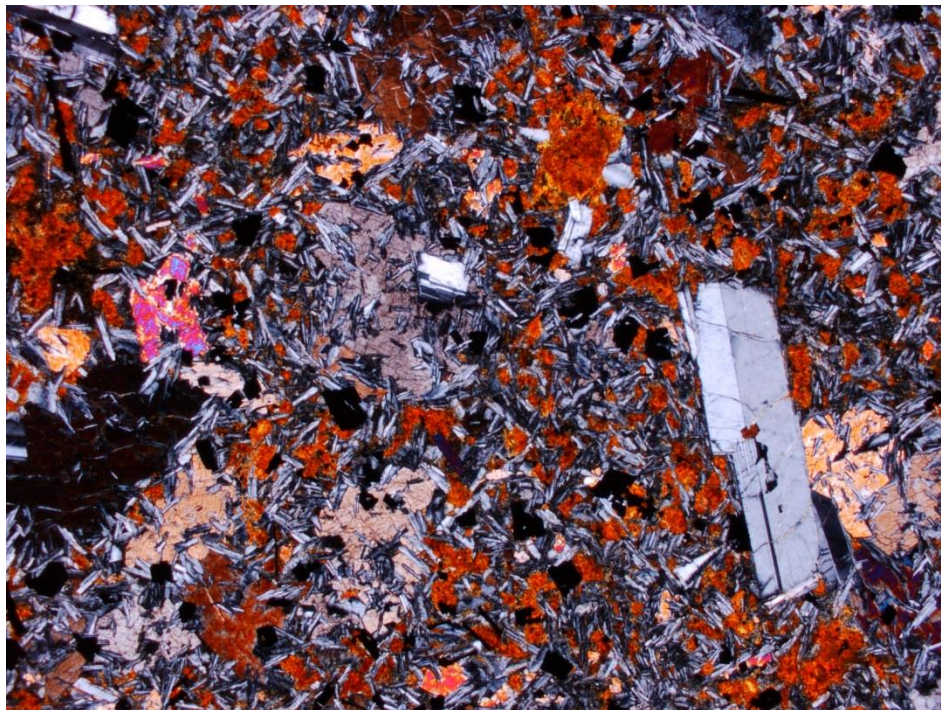


Figure 54. Photomicrographs of thin section from Type III intrusion in plane light (left) and crossed polars (right). Vertical dimension is 5 mm. Note plagioclase phenocryst is not as large as Type II phenocrysts, but low percentage. Olivine in groundmass and a few phenocrysts have been extensively altered to iddingsite (orange).

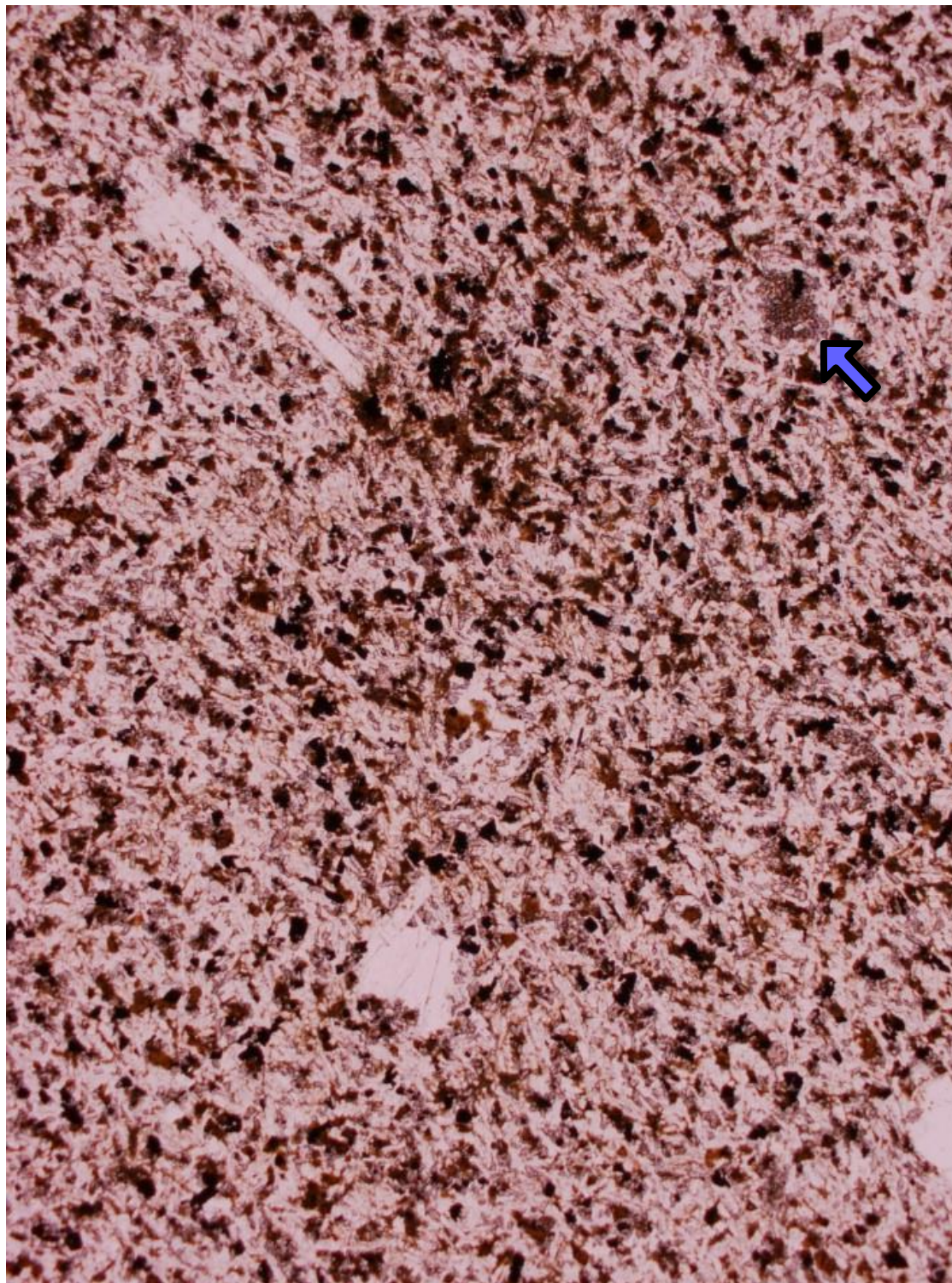


Figure 55. Photomicrograph of thin section of Type III diabase in plane light. View is 5 mm wide. Note size and percentage of plagioclase phenocrysts and altered olivine phenocryst (arrowed).



Figure 56. Billowed contact of Type III intrusion with Chisos strata. Note columns formed in baked Chisos mudstone at contact. Pencils for scale. Pencil on left rests on upper margin of baked Chisos mudstone where Type III has been eroded away.



Figure 57. Irregular Type III intrusive rock within Chisos strata. Arrowed dike is ~ 0.5 m wide.



Figure 58. Highly irregular Type III intrusive sheet within Chisos strata. Margins are billowed with tan color on outermost chilled edge of Type III material. Hammer for scale (arrowed).



Figure 59. Cross-section of Type III sheet in previous figure. Note chilled margin, seen in thin section in next figure. Pencil for scale.



Figure 60. Photomicrograph of chilled margin of Type III intrusion in previous figure, showing altered palagonite which still preserves orange tint. Note plagioclase phenocryst characteristic of Type III and slight increase in microcline size moving downward from chilled margin. Plane light; field of view is 5 mm across.

Chapter 5: Geochemistry and Geochronology

Introduction

Major- and trace-element analyses were carried out on eleven samples from the study area. Four samples were from Type III intrusive rocks, one each from Type I and Type II intrusions, two from Alamo Creek Basalt, two from vent-fill bombs, and one from a nearby outcrop of Ash Spring Basalt. Multiple samples were taken from Type III intrusive rocks to see if these rocks are compositionally uniform throughout the large outcrop, particularly in light of the lithological variations shown by this unit (e.g., the ophitic texture in some samples). Only one sample each was taken for the Type I and Type II intrusions because of their small lateral extent. Only two bomb samples were taken from vent-fill material because of the strong alteration of most of that material. Finally, the sample of Ash Spring Basalt was taken to compare material in the study area to the nearest lava flow younger than the Alamo Creek Basalt.

Analytical procedures have been described in Chapter 1. The geochemical data are presented in Table 1, and major oxides are reported on a volatile-free basis. The locations of the geochemical samples are shown in Plate I. As seen in this map, the Type III sample sites are spread throughout the study area. The Alamo Creek Basalt samples only came from the northern outcrop.

Petrographic analysis indicates that the geochemical samples are altered to varying degrees. Samples were generally taken from amygdule-free areas, but where that was impossible a great deal of care was taken to extract any secondary material before analysis. Secondary alteration of olivine, plagioclase, and pyroxene is visible in the thin sections of the geochemical samples, although the alteration is fairly light. Loss on ignition (LOI) values are less than 3.17 wt % for all intrusive and lava samples, which further indicates that the sampled rocks have not

undergone extreme alteration. The LOI values for the two bombs are higher, at 6.86 and 5.63 wt %, indicating that these samples are more heavily altered. Care must be taken when interpreting the geochemistry of the sample suite as a whole, particularly with respect to the mobile elements.

Geochemical data have been acquired from several sources for comparison with the new data from the study area. Data for the Alamo Creek, Ash Spring, and Bee Mountain Basalts are from Miggins (2009) and Parker et al. (2012). Data from Befus et al. (2009) and unpublished data from Hanson for samples collected during the studies by Winkler et al. (2009) and Deitz et al. (2010) are from intrusive hypabyssal mafic rocks generally associated with phreatomagmatic vents and having $^{40}\text{Ar}/^{39}\text{Ar}$ dates of 47-46 and 43-42 Ma, which correspond to timeframes for extrusion of the Alamo Creek and Ash Spring Basalts. In the Harker and discrimination diagrams presented below, the data from other sources have been plotted as points, but have been converted into fields for the multi-element and REE diagrams.

Table 1. Geochemical Data

	JH-54	JH-55	JH-56	JH-57	JH-58	JH-61	JH-62	JH-63	JH-72	JH-76	JH-81
	Type III	ACB	Bomb	Bomb	Type III	Type III	Type I	ACB	Type III	Type II	AS sample
Normalized Major Elements (Weight %)*											
SiO ₂	50.53	45.34	52.11	47.07	50.49	50.10	45.11	45.40	50.26	48.37	53.30
TiO ₂	3.030	3.934	3.654	4.481	2.953	3.021	3.941	3.910	3.022	3.094	2.338
Al ₂ O ₃	15.20	16.54	16.04	18.61	14.89	14.91	16.54	16.61	14.93	17.38	16.44
FeO*	12.24	13.75	13.38	14.54	12.55	12.60	13.92	13.92	12.61	11.18	10.81
MnO	0.178	0.227	0.179	0.163	0.191	0.195	0.188	0.221	0.178	0.212	0.127
MgO	4.46	5.70	1.90	1.52	4.81	4.86	5.57	5.05	4.79	3.00	1.63
CaO	8.71	9.45	7.40	7.71	8.57	8.76	9.94	9.92	8.54	10.04	5.84
Na ₂ O	3.45	3.01	2.26	3.33	3.38	3.42	2.74	2.91	3.55	4.20	4.15
K ₂ O	1.68	1.18	2.33	1.55	1.66	1.63	1.21	1.22	1.61	1.76	4.28
P ₂ O ₅	0.519	0.843	0.751	1.022	0.504	0.508	0.846	0.844	0.513	0.752	1.085
LOI**	1.34	3.05	6.86	5.63	0.94	1.86	2.65	2.81	2.07	1.89	3.17
Total***	98.25	96.38	92.88	93.79	98.47	97.97	97.43	96.84	98.05	97.35	96.30
Trace Elements (ppm)											
Ni	17.20	17.20	12.50	14.60	19.00	17.40	18.70	17.10	16.30	12.80	5.50
Cr	9.10	0.00	0.20	0.00	8.40	9.60	0.00	0.00	9.40	4.90	1.10
Sc	27.40	16.67	14.98	16.88	27.39	26.86	17.05	16.90	27.00	20.99	14.40
V	350.20	270.00	257.60	298.20	347.50	343.90	279.60	271.00	334.40	233.40	68.00
Ba	519.74	923.88	436.44	386.57	505.30	504.25	405.14	344.32	490.31	472.53	875.79
Rb	34.95	17.27	54.01	28.55	35.51	33.79	18.56	19.35	32.78	32.71	81.48
Sr	538.42	839.05	645.99	989.98	527.18	543.79	943.58	891.27	532.98	734.59	521.63
Zr	247.68	211.09	196.28	214.25	242.50	236.23	212.65	212.66	237.51	312.45	513.08
Y	33.99	27.18	28.24	27.64	33.36	32.93	27.74	27.56	33.16	32.89	49.24
Nb	19.34	31.70	28.63	32.98	18.87	18.71	31.95	31.71	18.74	38.15	74.02
Ga	22.10	20.80	17.20	21.00	22.60	20.90	21.20	20.80	22.00	22.80	23.60
Cu	12.80	16.50	15.80	26.60	12.80	12.40	16.70	16.30	12.70	47.20	29.60
Zn	119.20	112.50	74.40	127.20	117.50	116.50	111.90	108.90	116.40	113.30	125.30
Pb	6.34	2.55	3.49	2.97	6.38	5.69	3.08	2.72	7.43	4.26	7.28
La	31.88	34.50	32.93	36.42	31.26	30.44	34.41	34.26	30.61	40.19	72.73
Ce	69.05	73.65	68.77	76.48	67.64	65.84	73.78	74.02	65.81	85.11	150.24
Th	4.28	3.34	3.50	3.56	4.25	3.94	3.36	3.37	3.95	4.15	9.05
Nd	37.13	39.70	37.17	40.73	35.83	35.36	39.78	39.84	35.14	44.18	72.53
U	1.24	1.09	2.52	1.71	1.22	1.13	1.09	1.07	1.12	1.40	2.98
Pr	8.84	9.44	8.84	9.77	8.64	8.48	9.47	9.45	8.46	10.71	18.28
Sm	8.40	8.62	8.06	8.66	8.01	7.80	8.76	8.65	7.93	9.47	15.00
Eu	2.54	2.83	2.67	2.93	2.47	2.45	2.84	2.86	2.47	2.93	4.15
Gd	7.74	7.75	7.40	7.90	7.69	7.58	7.74	7.66	7.56	8.45	12.72
Tb	1.21	1.12	1.08	1.13	1.20	1.18	1.13	1.12	1.17	1.27	1.90
Dy	7.16	6.17	5.97	6.17	6.98	7.01	6.20	6.13	6.84	7.25	10.76
Ho	1.38	1.12	1.08	1.11	1.35	1.32	1.11	1.12	1.31	1.31	1.97
Er	3.62	2.74	2.77	2.70	3.55	3.45	2.76	2.73	3.46	3.32	5.01
Tm	0.51	0.36	0.36	0.36	0.50	0.49	0.36	0.36	0.48	0.45	0.70
Yb	2.99	2.07	2.07	2.10	2.95	2.88	2.07	2.07	2.87	2.67	4.11
Lu	0.47	0.31	0.31	0.31	0.46	0.45	0.31	0.30	0.43	0.39	0.63
Hf	5.96	4.92	4.62	5.04	5.87	5.60	4.90	4.93	5.68	7.07	11.54
Ta	1.33	2.20	1.99	2.26	1.31	1.29	2.18	2.16	1.28	2.58	4.85
Cs	0.31	0.69	1.20	0.82	0.35	0.59	0.23	0.40	0.30	8.82	1.59

*Normalized to 100% on volatile-free basis; ** Loss on Ignition; *** Total before normalization;
ACB = Alamo Creek Basalt; AS Sample = Ash Spring Sample

Major Elements

A legend for the symbols used in the diagrams for this section and the next is shown in Figure 61. In the diagram of Hughes (1973) (Fig. 62), which is useful in examining the degree of alteration of samples, only one sample plots outside of the normal igneous spectrum, indicating disturbance of the alkalis in this sample. Unsurprisingly, this sample is one of the bombs. It is noteworthy that this is the bomb which plots furthest away from the Alamo Creek Basalt/Type I grouping throughout the majority of the geochemical diagrams.

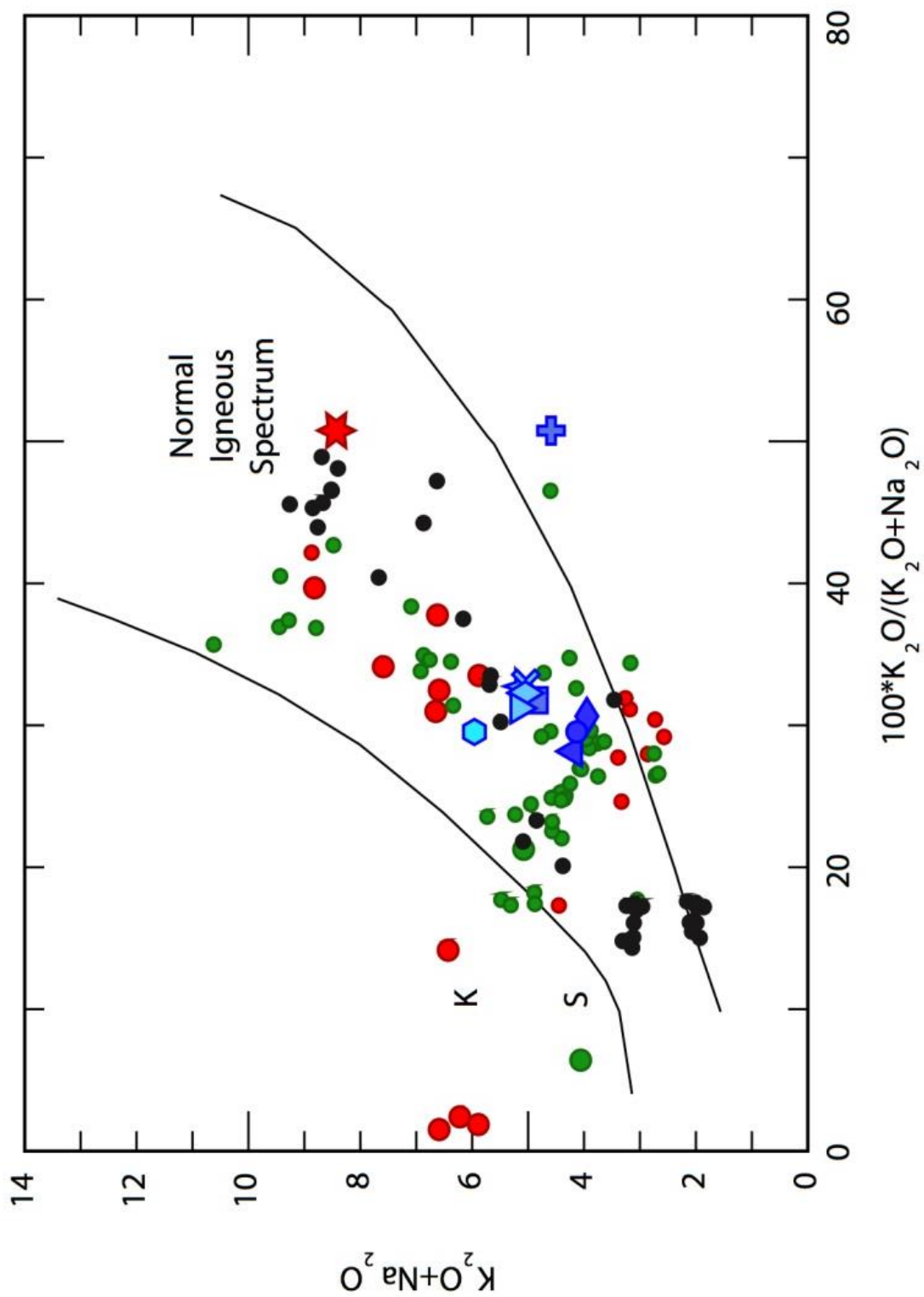
The total alkalis versus silica plot of LeBas et al. (1986) in Figure 63 shows most of the samples to fall in the basalt field or on the boundary between that field and the trachybasalt field. Type II plots well within the trachybasalt field, while the sample from the Ash Spring Basalt is plots as a basaltic trachyandesite.

Harker variation diagrams for the major elements in the samples are shown in Figures 64-71. Silica values for the samples from the study area range from 45.11-53.30 wt%. Values for the Type III intrusive rocks are tightly clustered, showing almost no variation, as are the grouping of Alamo Creek Basalt and Type I samples. The two bombs, in contrast, show significant variation in silica and also are much lower in MgO than the intrusive units, probably reflecting greater alteration of these samples. The Ash Spring sample is also low in MgO and significantly higher in K₂O, but these values are considered to be primary and reflect the more evolved composition of this sample.

Legend

	JH-61	Type III
	JH-58	Type III
	JH-54	Type III
	JH-72	Type III
	JH-76	Type II
	JH-62	Type I
	JH-63	Alamo Creek Basalt
	JH-55	Alamo Creek Basalt
	JH-56	Bomb
	JH-57	Bomb
	JH-81	Ash Spring Basalt
	47-46 Ma basaltic intrusions	
	43-42 Ma basaltic intrusions	
	Alamo Creek Basalt	
	Ash Spring Basalt	
	Bee Mountain Basalt	

Figure 61. Legend for all geochemical diagrams. See text for sources of other data sets.



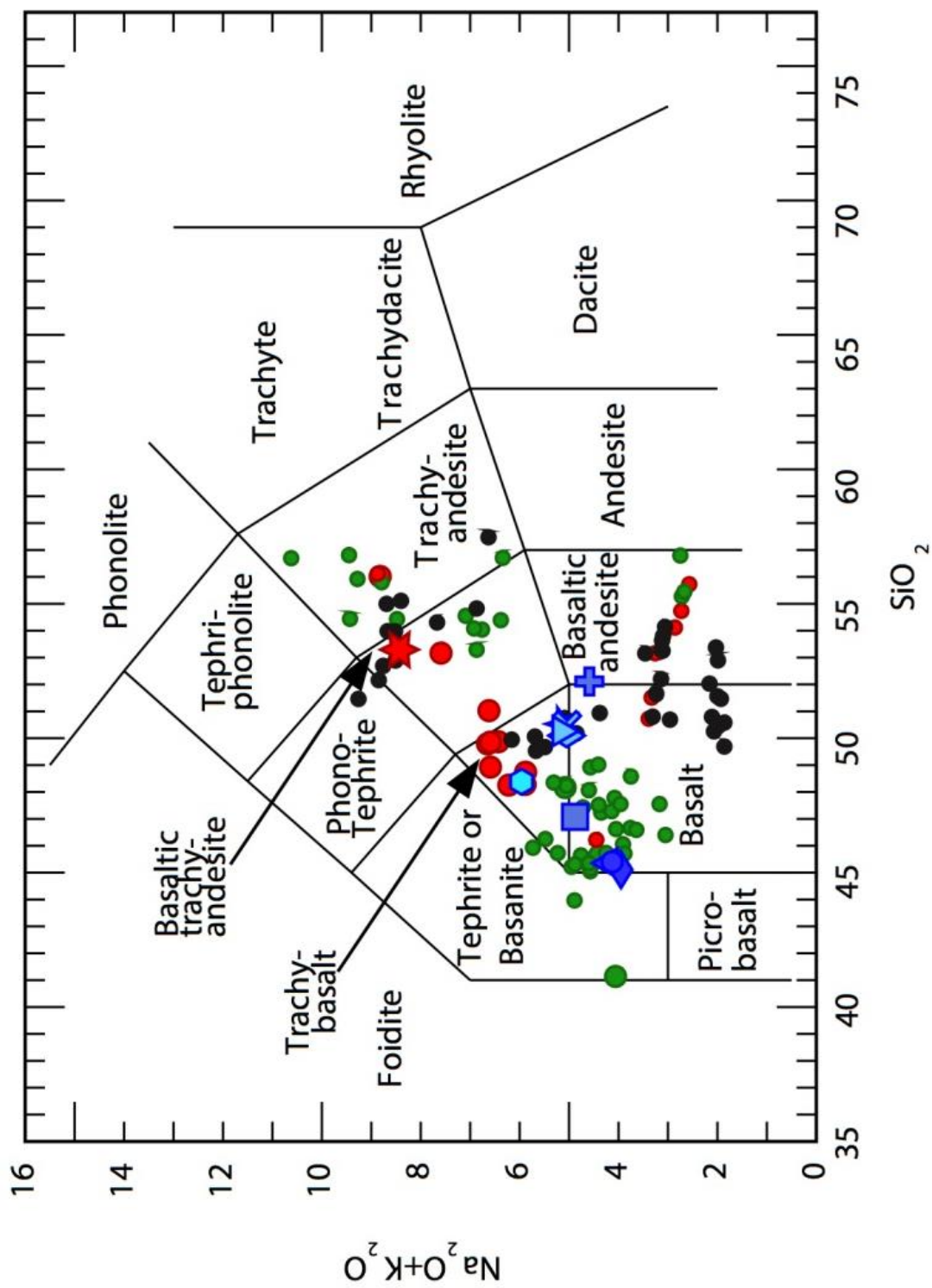


Figure 63. Total alkalis versus silica diagram of LeBas et al. (1986).

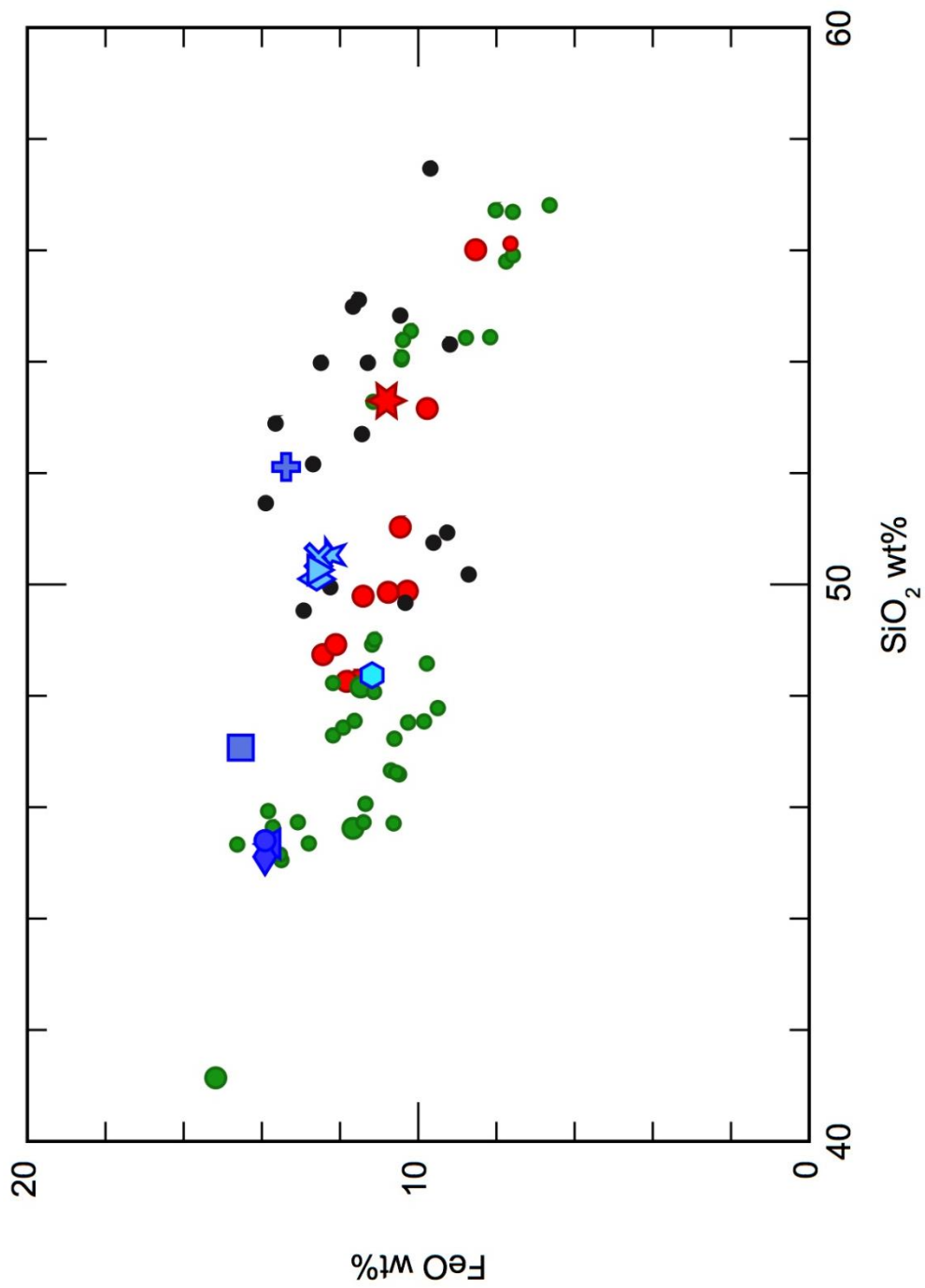


Figure 66. Harker diagram for FeO.

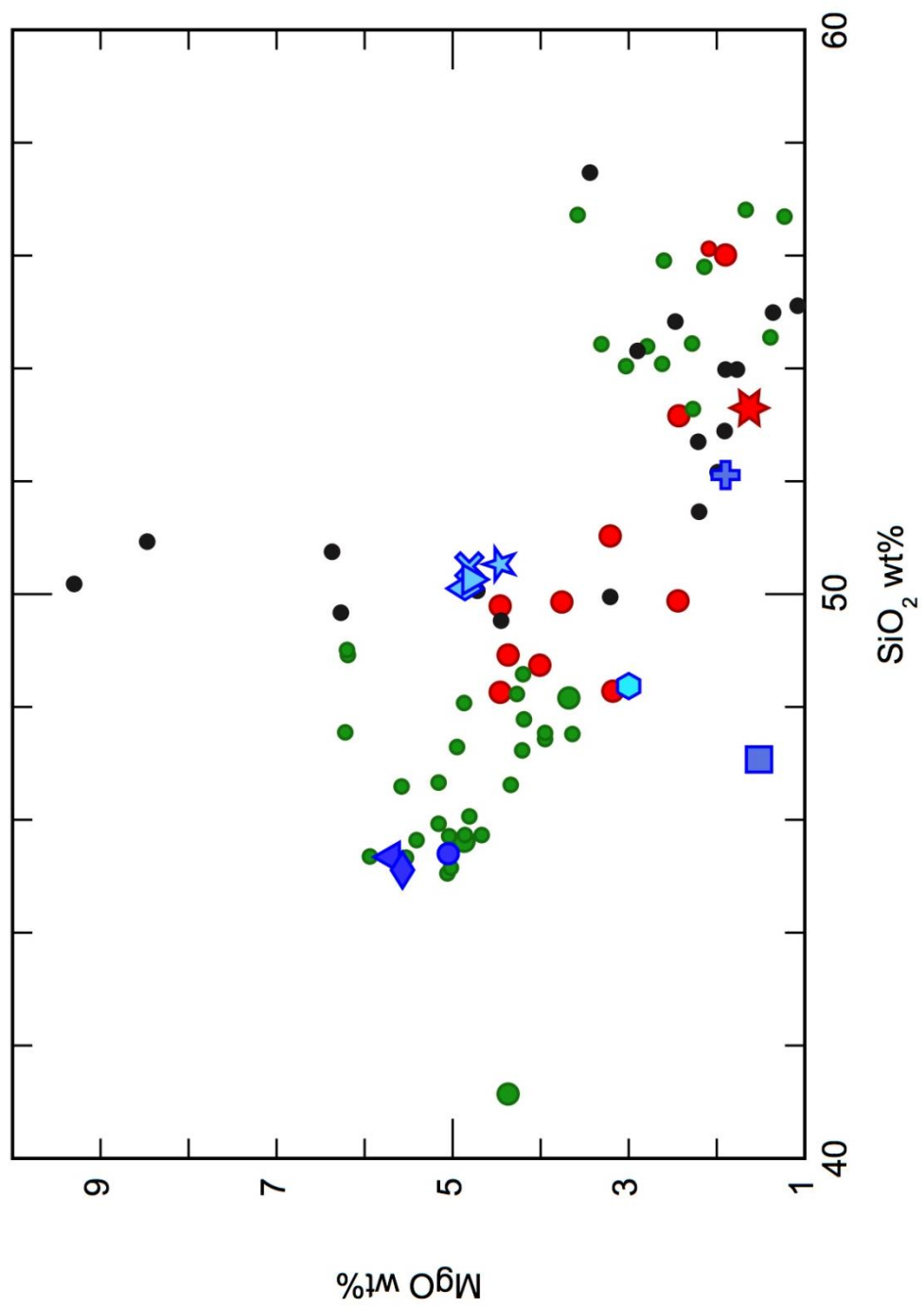


Figure 67. Harker diagram for MgO.

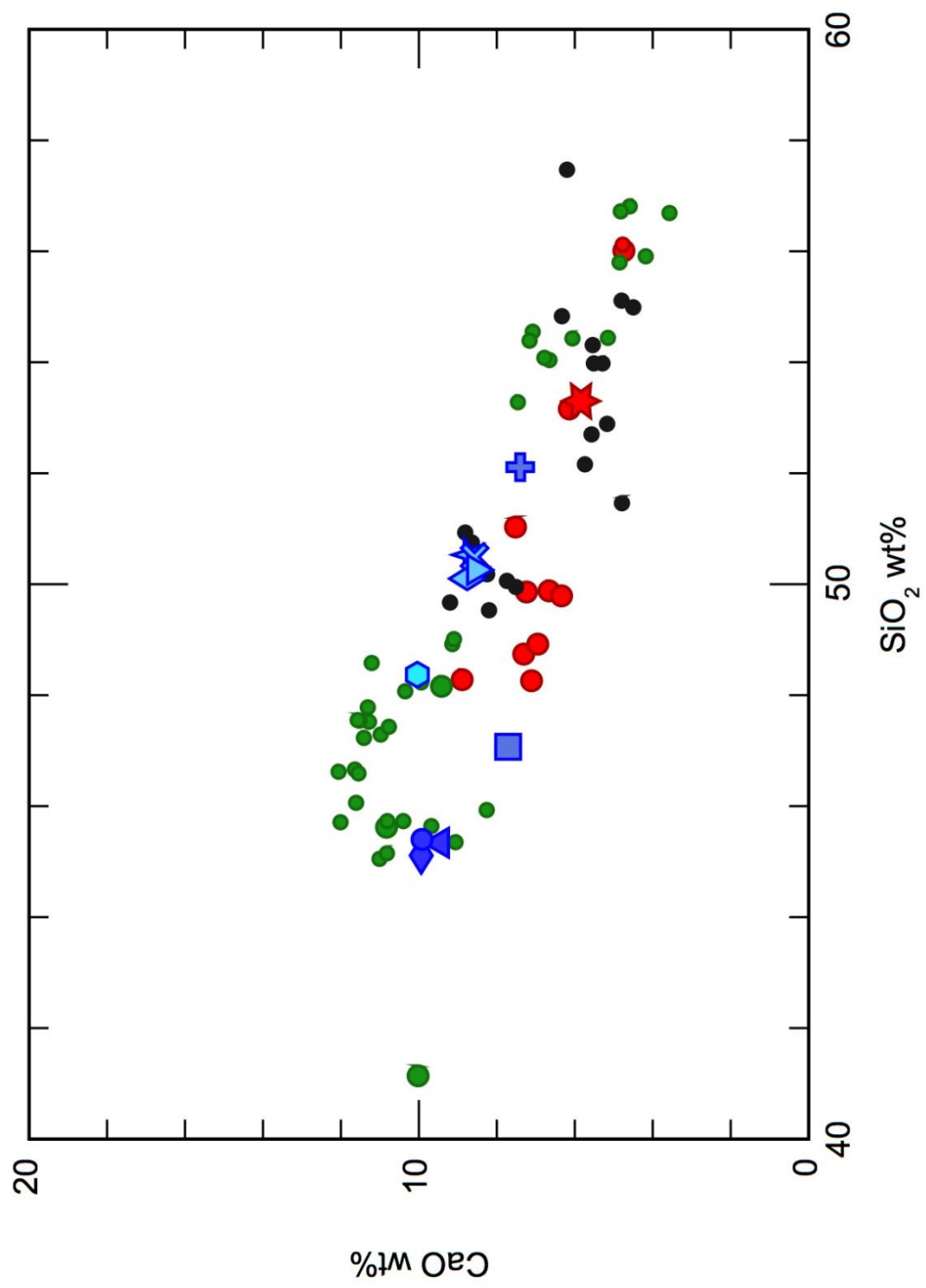
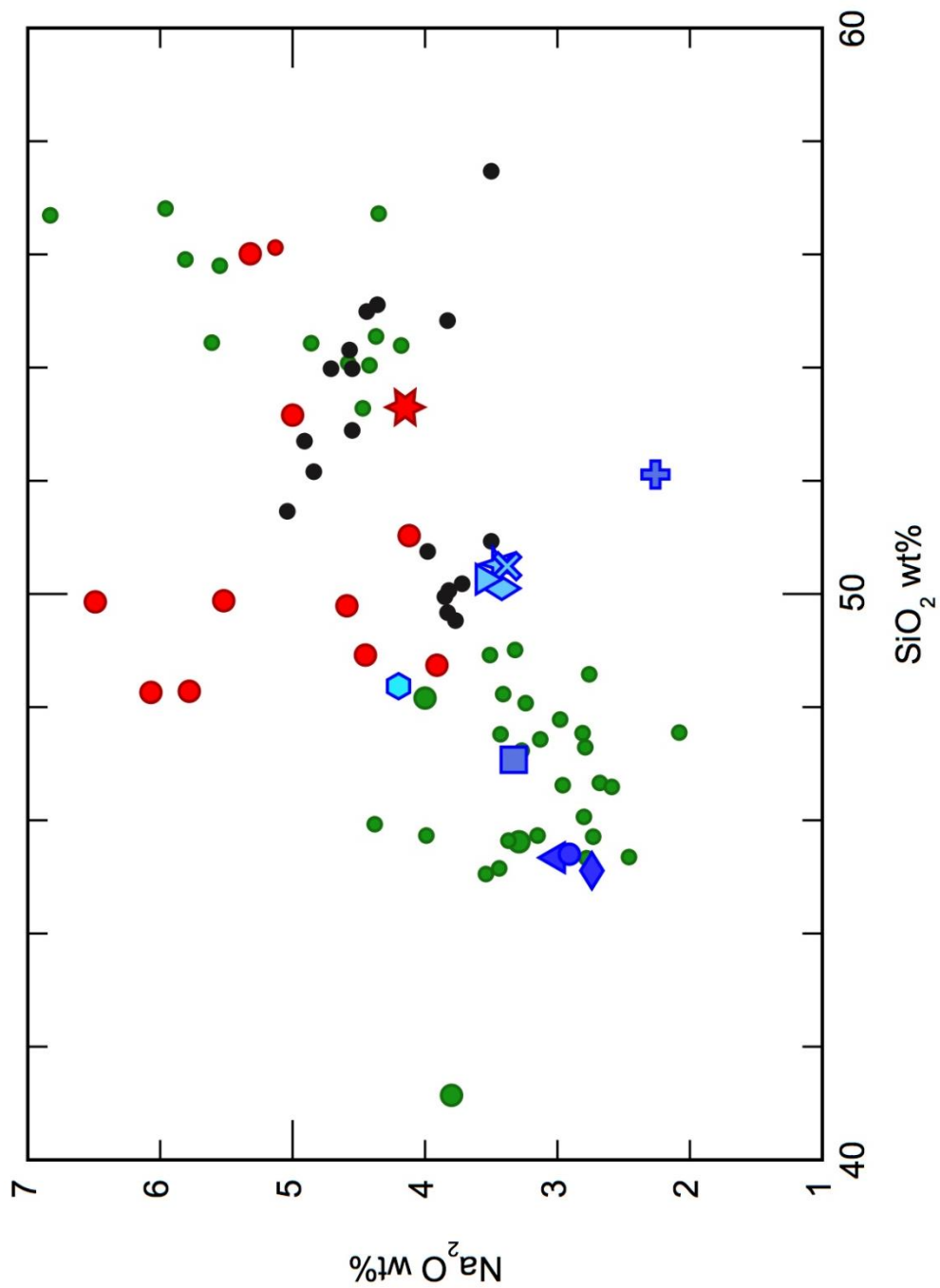
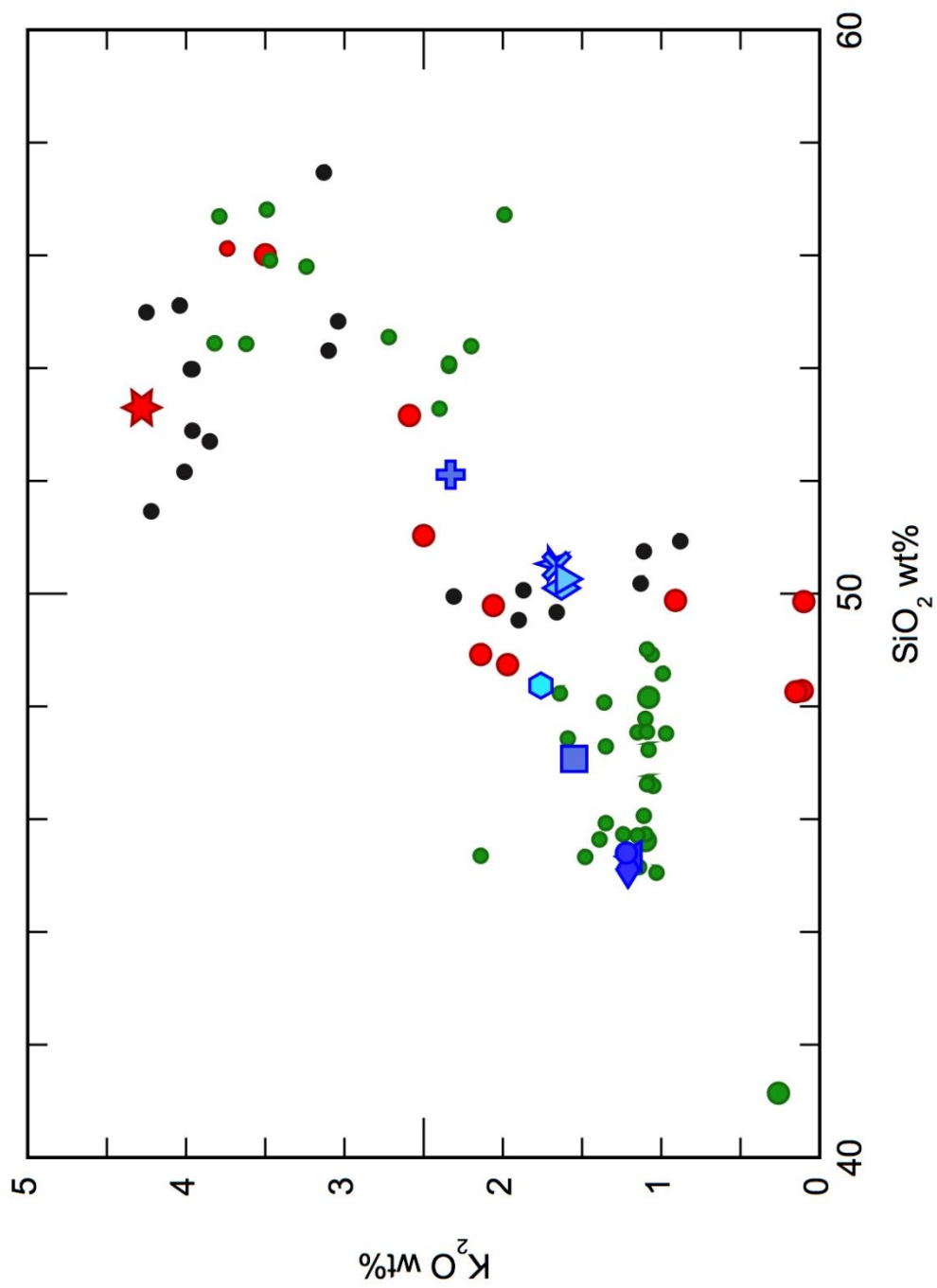
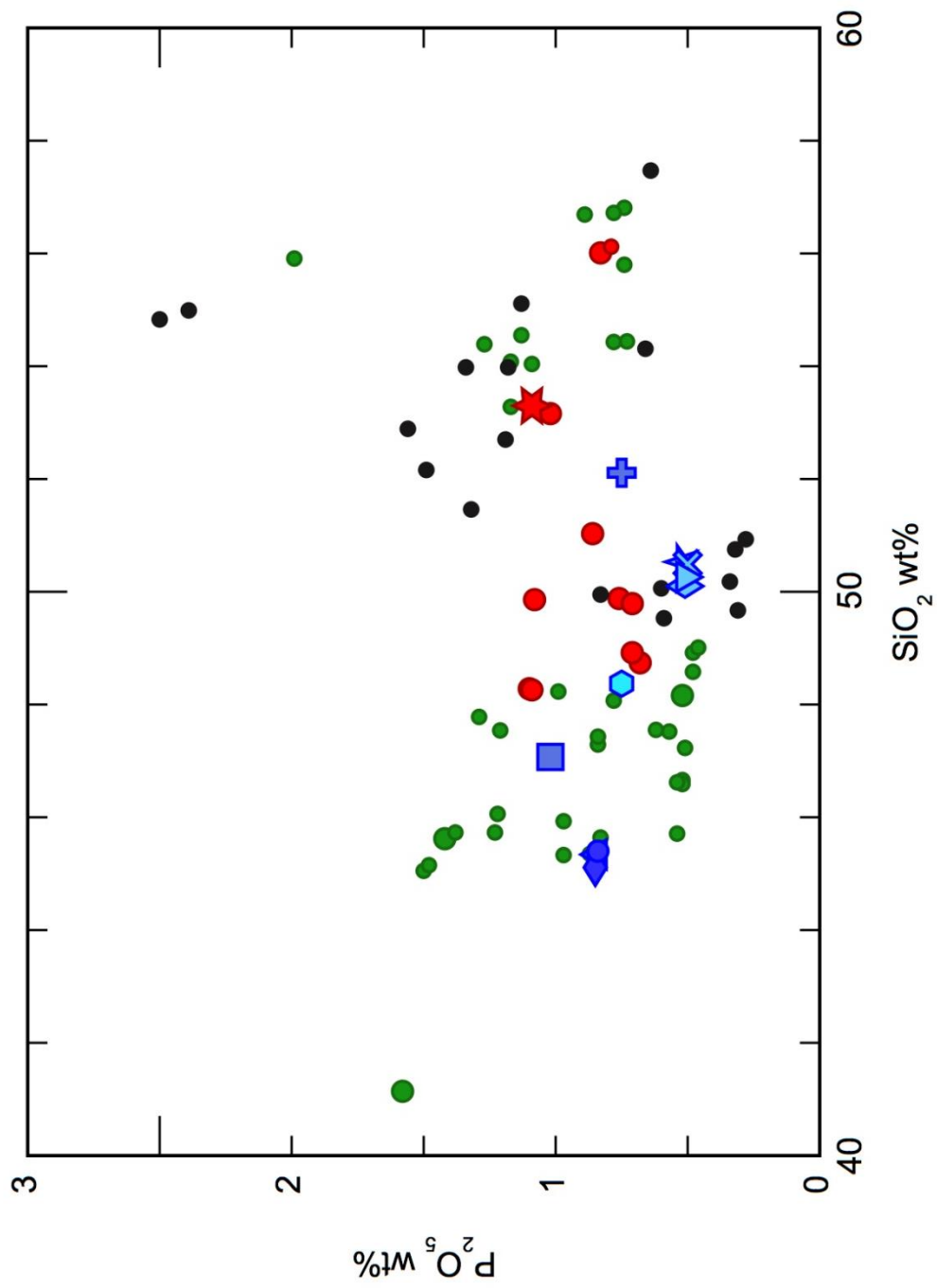


Figure 68. Harker diagram for CaO.

Figure 69. Harker diagram for Na₂O.

Figure 70. Harker diagram for K_2O .

Figure 71. Harker diagram for P_2O_5 .

Trace Elements

Normalized Multi-Element and REE Diagrams

All of the study samples are plotted with the comparison data on a multi-element diagram normalized to primitive mantle, following Sun and McDonough (1989), in Figure 72. In this diagram, the more mobile elements (Cs, Rb, Ba, U, K, Pb, and Sr) show a fair amount of spread, but this partly is the result of alteration. Once these elements are ignored, two clusters of points become quite apparent, one of which is defined by the Type III samples, with the other being defined by the Alamo Creek Basalt, Type I, and bomb samples. The Type III data show very little spread, even in the mobile elements, which is strong evidence that the Type III intrusive rocks represent a single, homogeneous mass of magma. This result is consistent with data from the Harker diagrams as well. The second cluster represented by the Alamo Creek Basalt, Type I, and bomb samples shows only a slight variation in the immobile elements, leading to the conclusion that all three of these units are petrogenetically closely related. The bombs typically show more separation in the mobile elements from the Alamo Creek Basalt and Type I samples, consistent with the results shown in the Hughes (1973) and Harker diagrams.

The pattern for the Ash Spring sample has a more fractionated pattern in Fig 72 than the other samples. This is expressed in its greater enrichment of the large-ion-lithophile elements in the left part of the diagram and the stronger depletion of Sr and Ti. These results are consistent with its more evolved major-element composition.

The Type III group shows a strong negative Nb-Ta anomaly. This result indicates that the Type III magma was derived from or interacted with a source region that was affected by subduction processes at some point in time and is consistent with the tectonic history of the Trans-Pecos Magmatic Province (see Chapter 2). The other samples show less variation in Nb

and Ta contents relative to adjacent elements. Comparison of Nb and Ta with U and K is not recommended in this case, because the latter two elements are mobile and have probably been altered in these samples. Therefore, Nb and Ta are compared to the nearest immobile elements on each side, which are La and Th. With this comparison, the Alamo Creek Basalt, Type I intrusion, and bomb samples show a very slight negative anomaly, the Ash Spring sample shows a slight negative anomaly, and the Type II sample shows no evidence of negative Nb and Ta anomalies.

The REE patterns for the samples from the study-area rocks as well as fields for the comparison data are shown in Figure 73. REE are generally immobile during low-temperature alteration, making them excellent for determining the degree of primary geochemical heterogeneity in the sample groups recognized in the previous diagrams.

All of the samples show LREE enrichment. The only sample that shows a negative Eu anomaly is the Ash Spring trachyandesite, indicative of feldspar fractionation during its petrogenesis. As in the normalized multi-element diagram, all of the Type III samples are effectively identical. The Alamo Creek Basalt, Type I, and bomb samples are also tightly clustered and show slightly lower HREE contents than the Type III and Type II samples.

This diagram confirms the results from the other diagrams that all the Type III samples are chemically very similar. Also, the tight grouping of the Alamo Creek Basalt, Type I, and bomb samples in terms of immobile element contents shows that these three units were likely derived from a single homogeneous batch of magma. The spread of the two bomb samples away from the Alamo Creek Basalt and Type I group in the Harker diagrams is most likely due to alteration of the bombs during or after phreatomagmatic explosive activity.

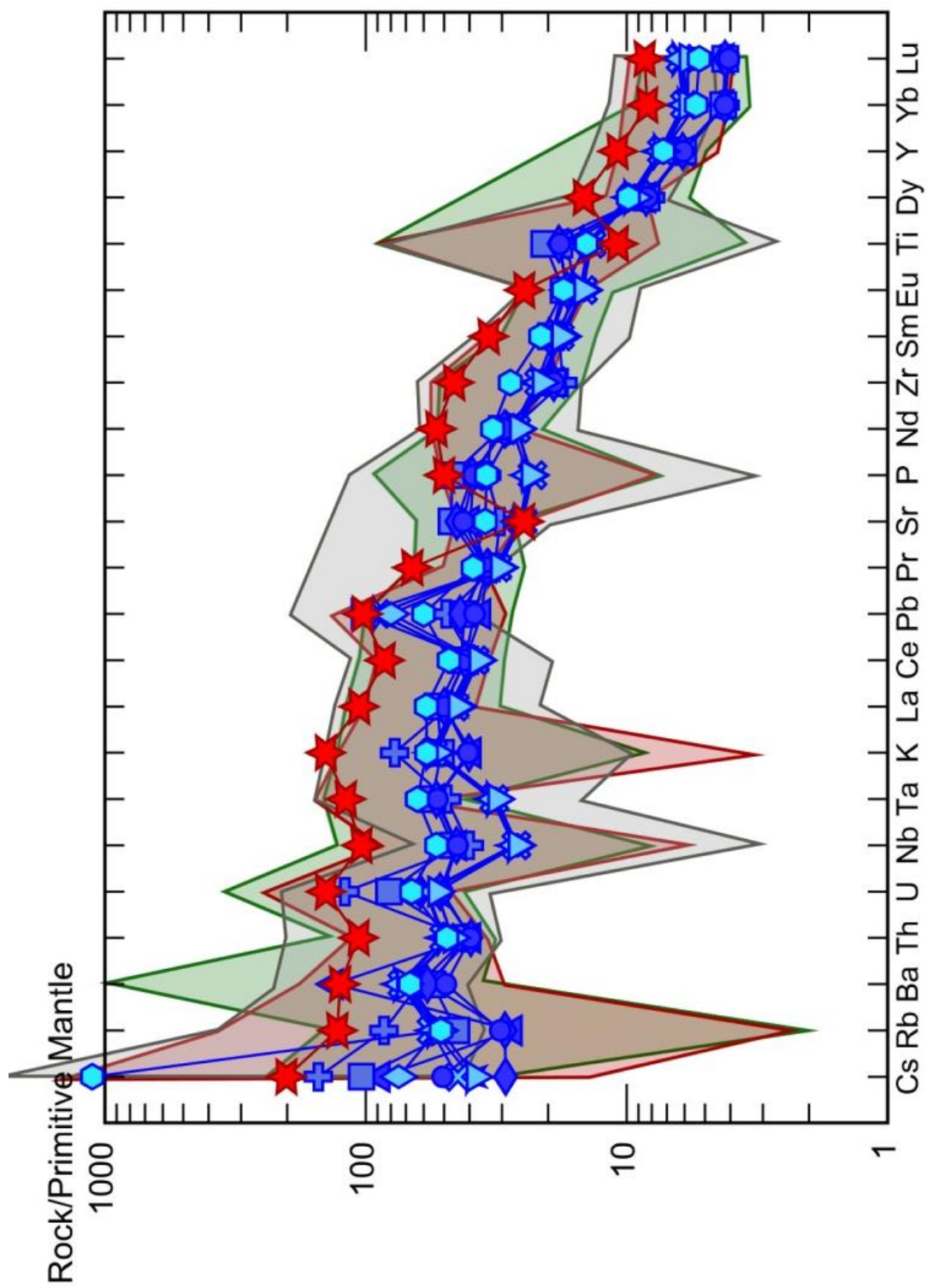


Figure 72. Multi-element diagram for study area samples with fields of comparison data; normalization values from Sun and McDonough (1989). Green field is Alamo Creek Basalt data, red is Ash Spring Basalt, grey is Bee Mountain Basalt.

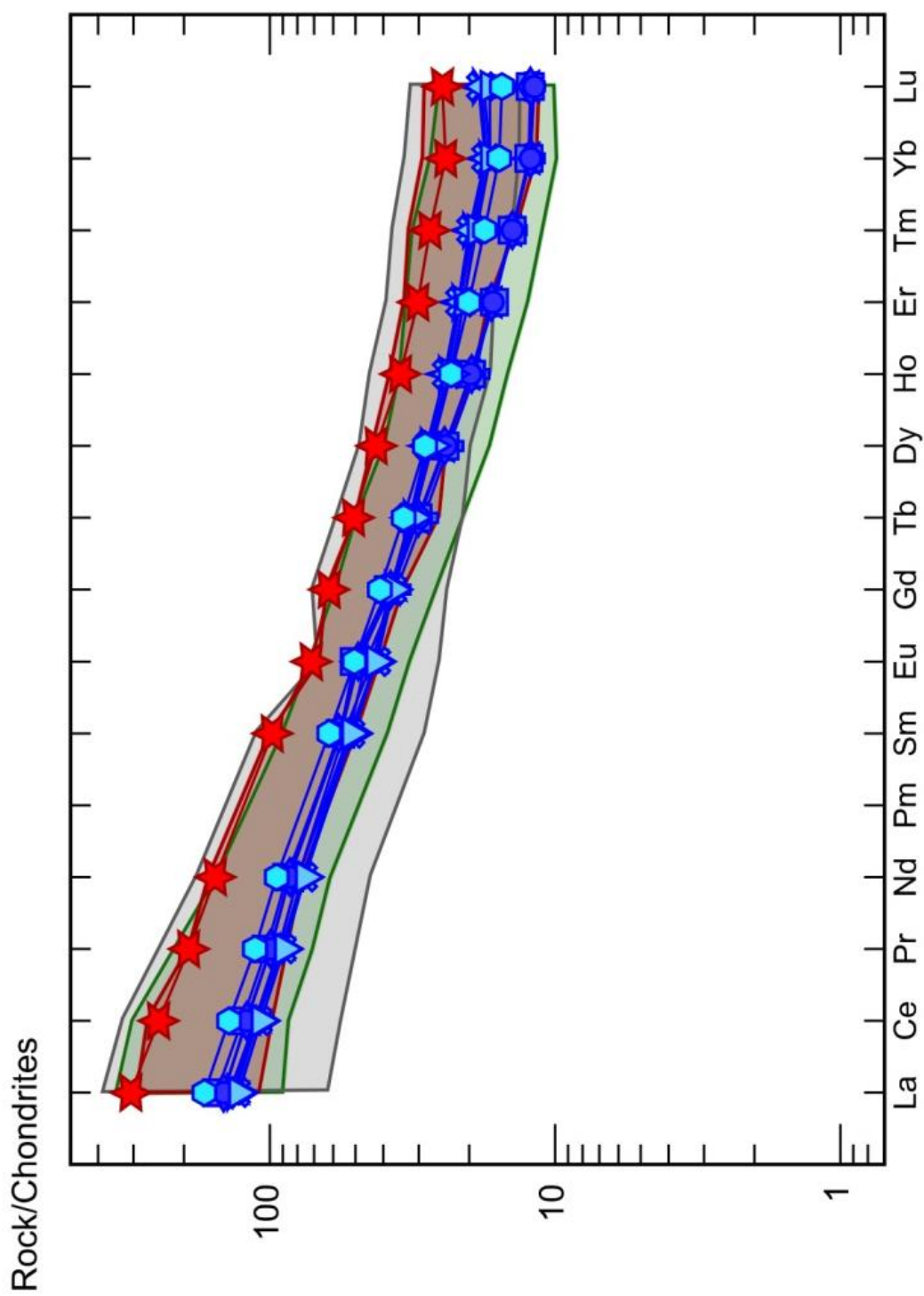


Figure 73. REE diagram for study area samples with fields of comparison data; normalization values from Sun and McDonough (1989). Green field is Alamo Creek Basalt data, red is Ash Spring Basalt, grey is Bee Mountain Basalt.

Trace-Element Discrimination Diagrams

The samples from the study area, as well as the comparison data sets, are plotted on a series of standard discrimination diagrams in Figures 74-79, which use immobile trace elements and are applicable to mafic rocks. In general, samples from the study area fall in within-plate fields. The only sample that does not follow this trend in all the diagrams is the Ash Spring sample. This is most likely because these diagrams are intended for basalts, while the Ash Spring sample has a more evolved composition.

The Type III samples fall in the subalkaline basalt or tholeiitic basalt fields in Figures 74, 78, and 79. The Type II sample as well as the group defined by the Alamo Creek Basalt, Type I intrusion, and bomb samples fall consistently within alkaline basalt fields in Figures 74 and 79, although Figure 78 places these samples in the transitional field between tholeiitic and alkaline basalts.

Interestingly, the Ash Spring and Type II samples fall within the cluster of data for the 43-42 Ma basaltic intrusive samples (Hanson, unpublished data). The group defined by the Alamo Creek Basalt, Type I intrusion, and bombs plot within the general range of data for Alamo Creek Basalt samples from other areas. Finally, the Bee Mountain Basalt data show far too much variation to form any viable conclusions about relationships to units in the study area.

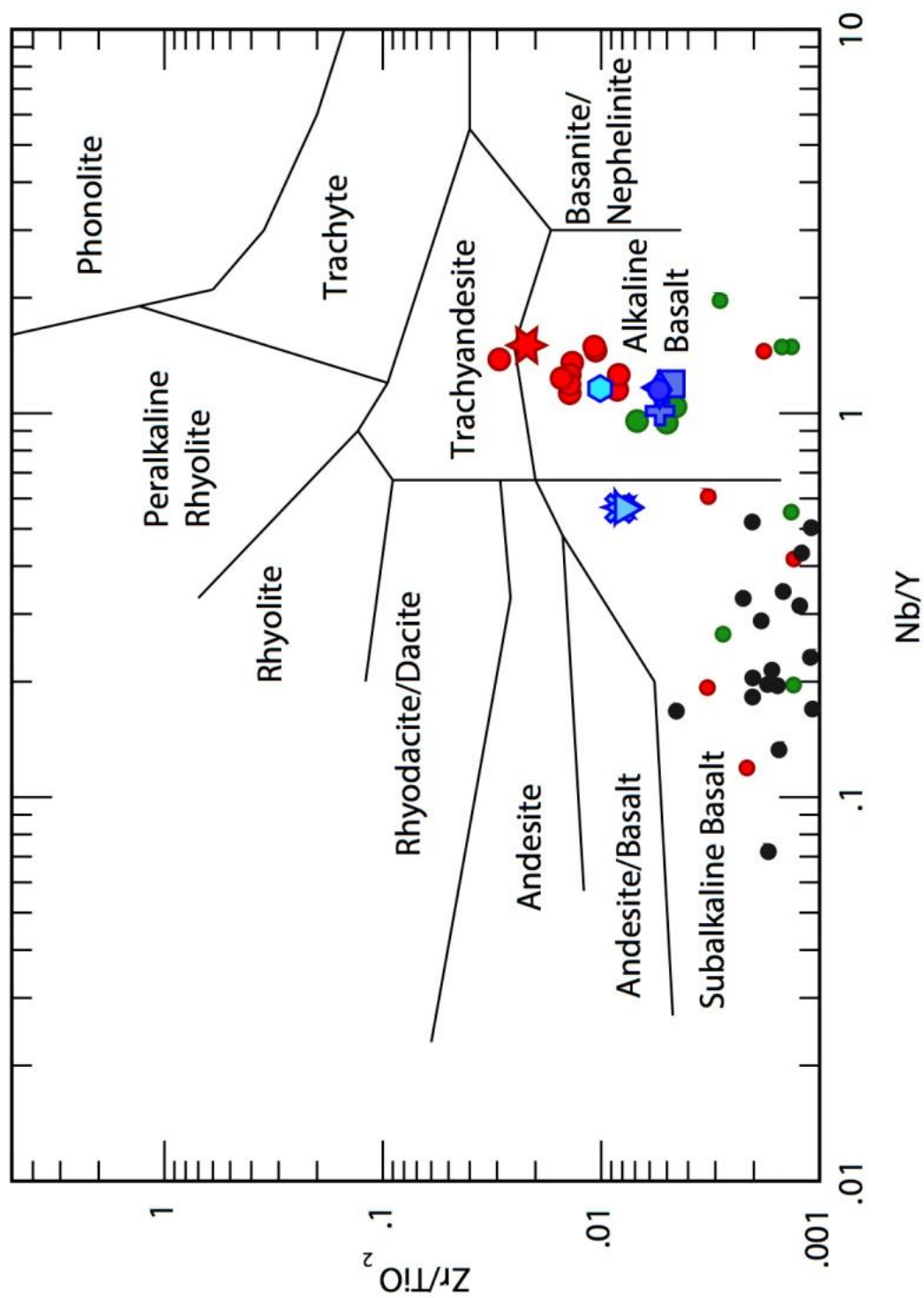


Figure 74. Discrimination diagram of Winchester and Floyd (1977).

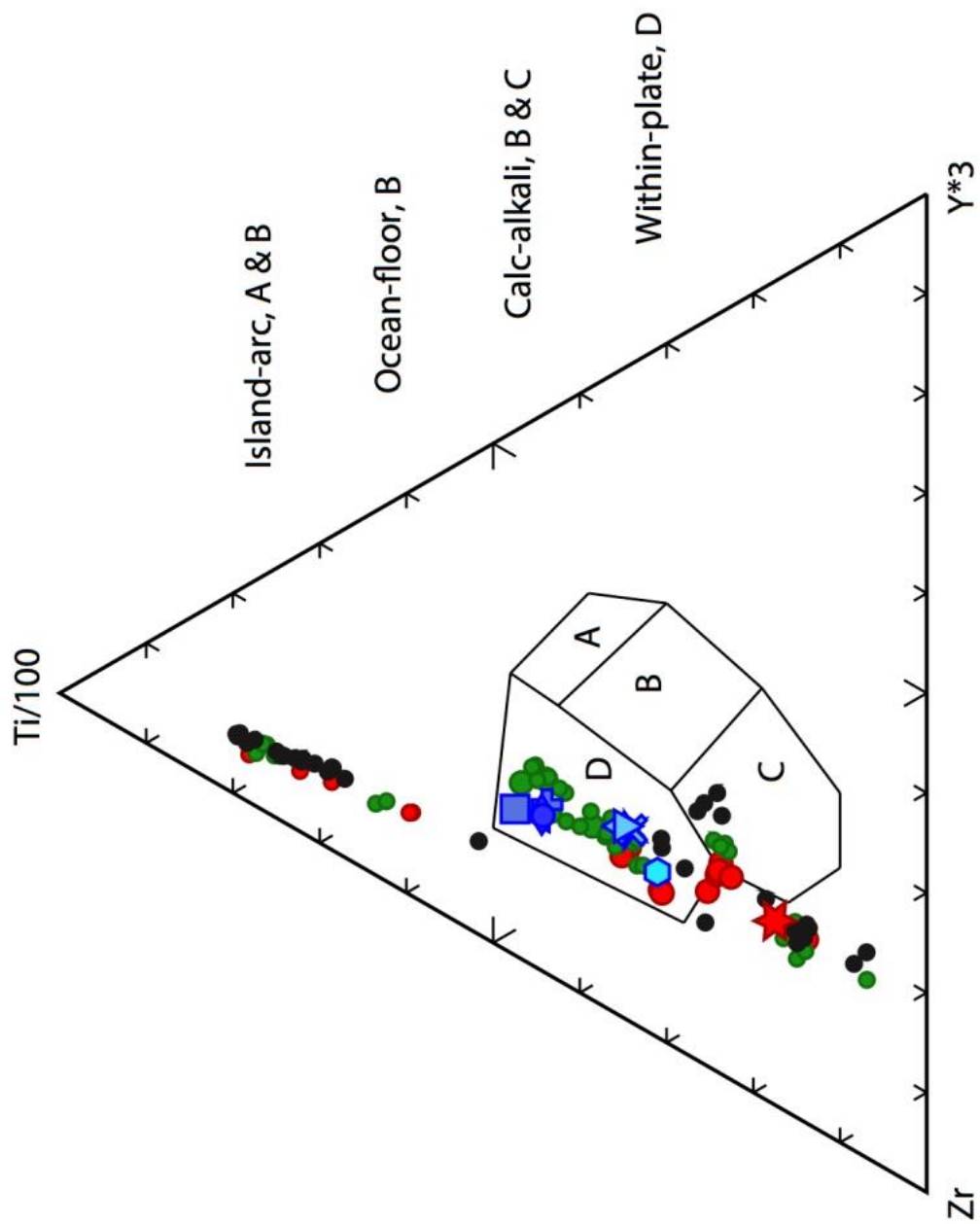


Figure 75. Zr-Ti-Y discrimination diagram of Pearce and Cann (1973).

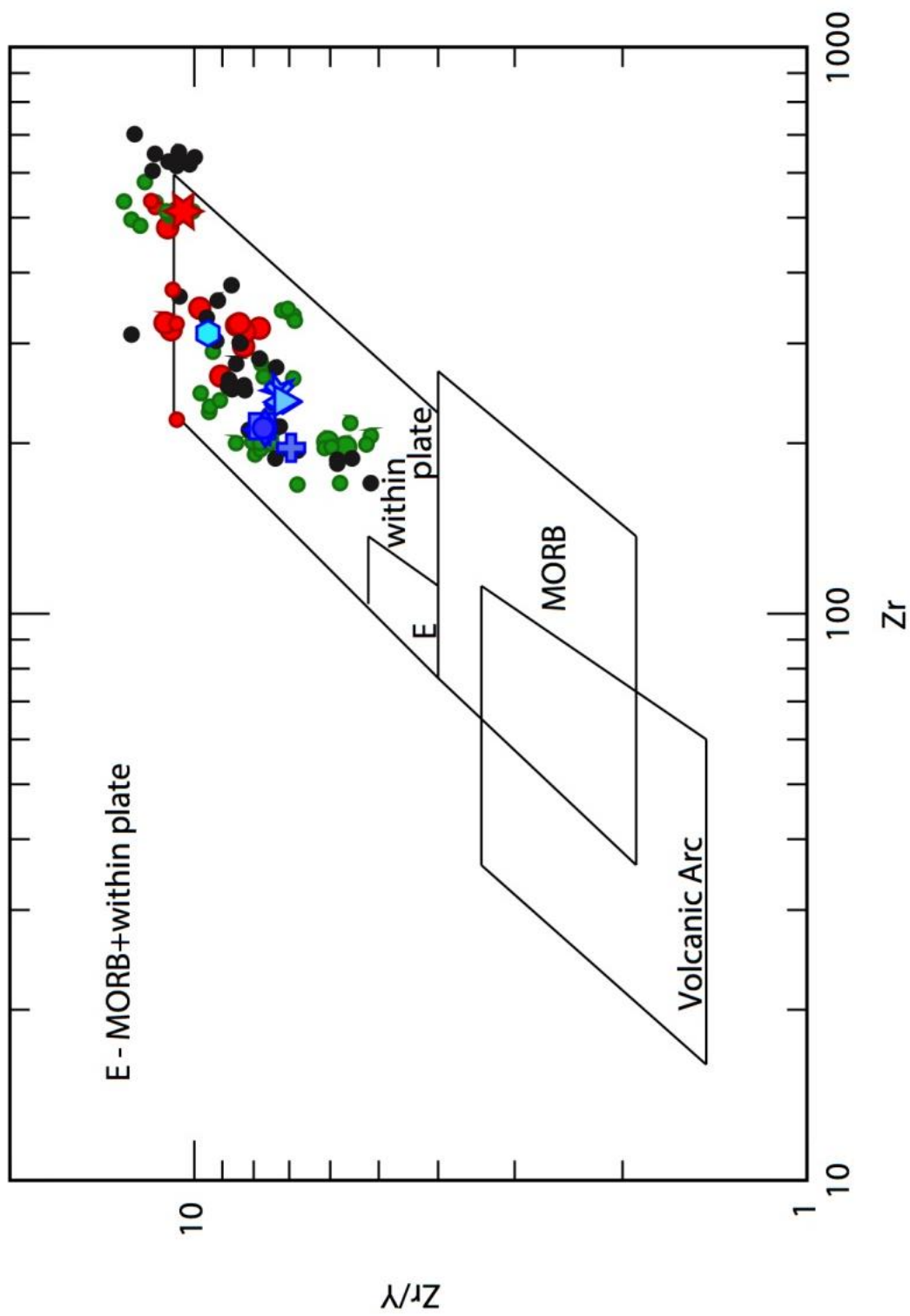


Figure 76. Zr/Y versus Zr discrimination diagram of Pearce and Norry (1979).

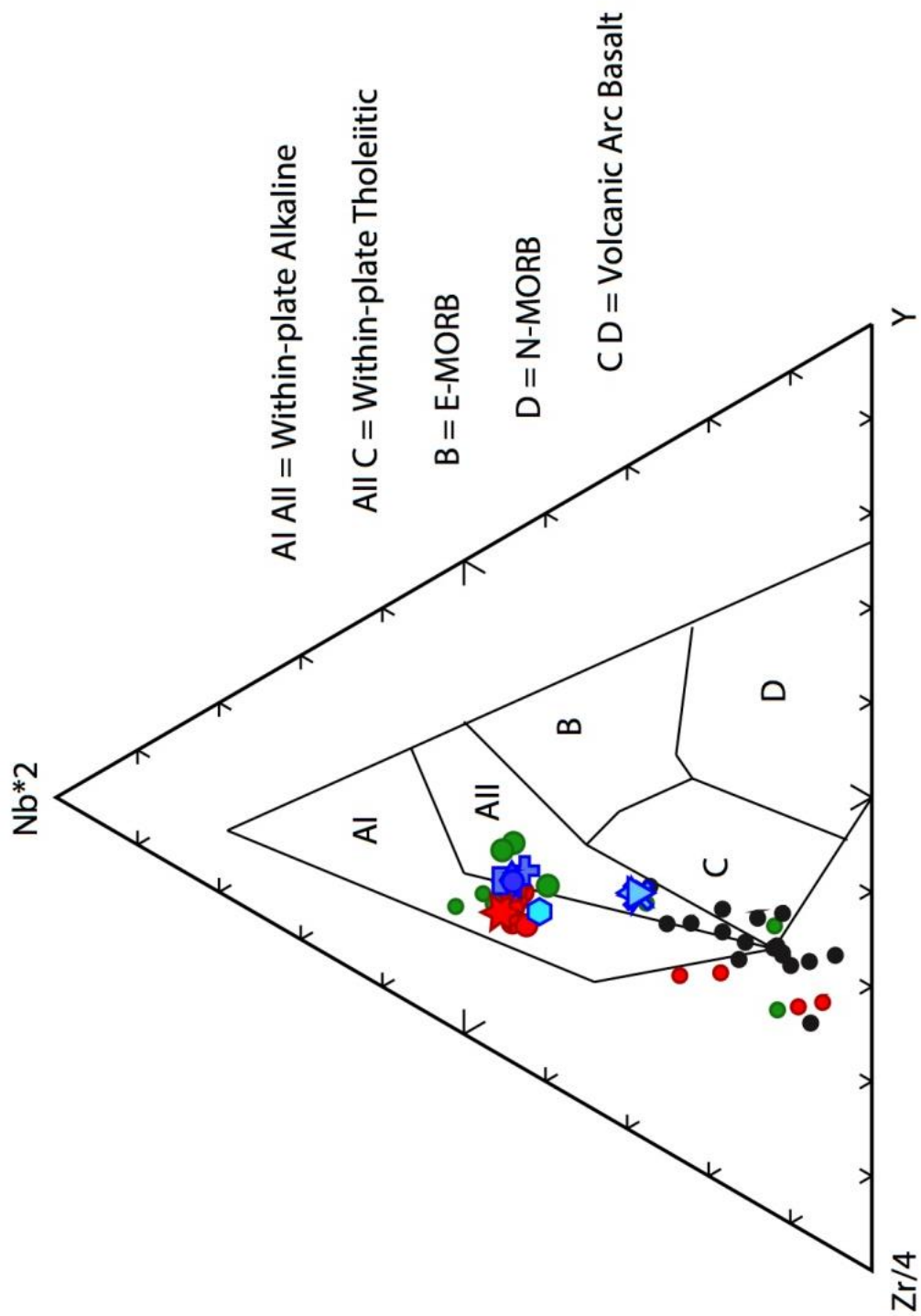


Figure 77. Zr/4-Nb*2-Y discrimination diagram of Meschede (1986).

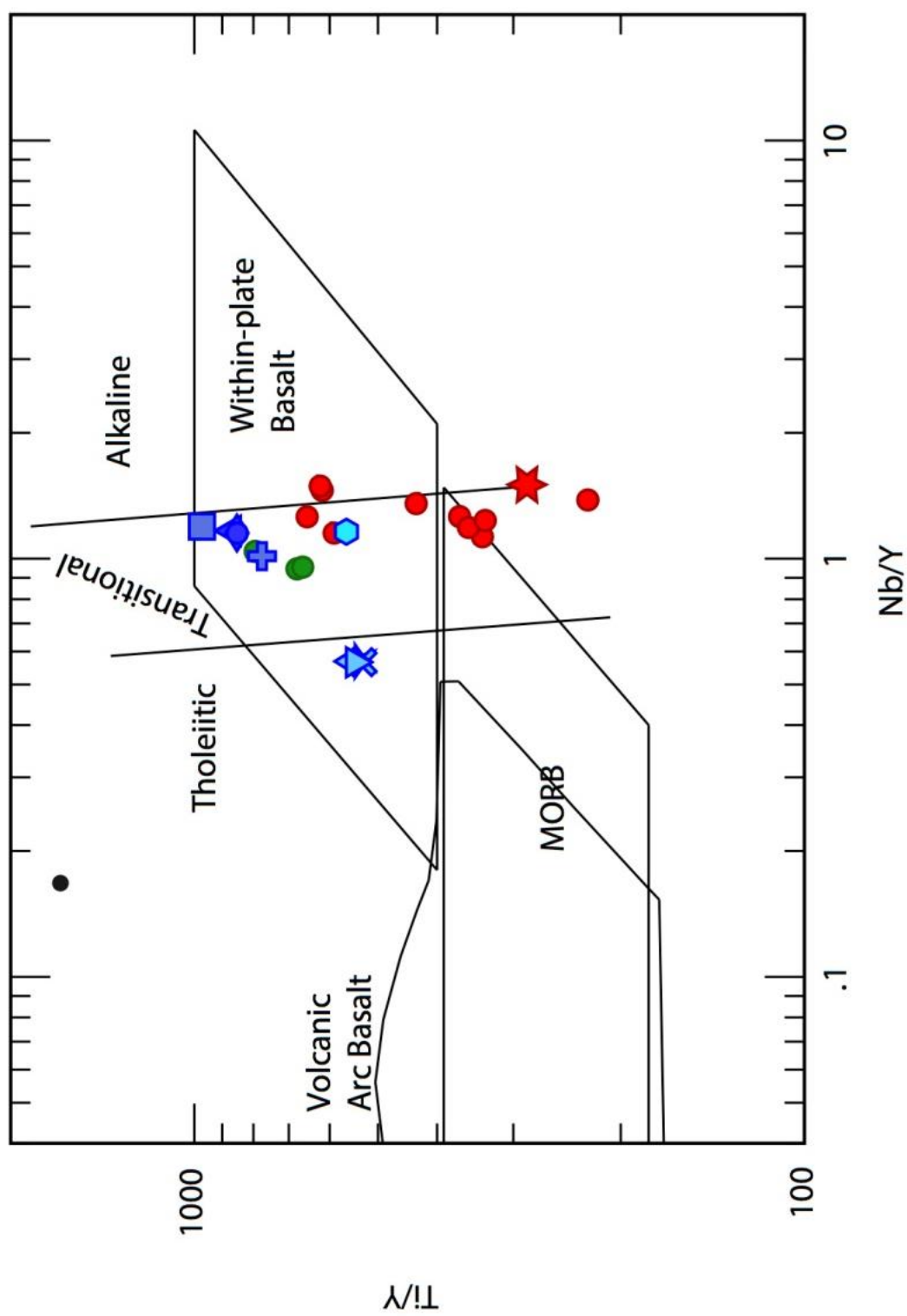


Figure 78. Ti/Y vs Nb/Y discrimination diagram of Pearce (1982).

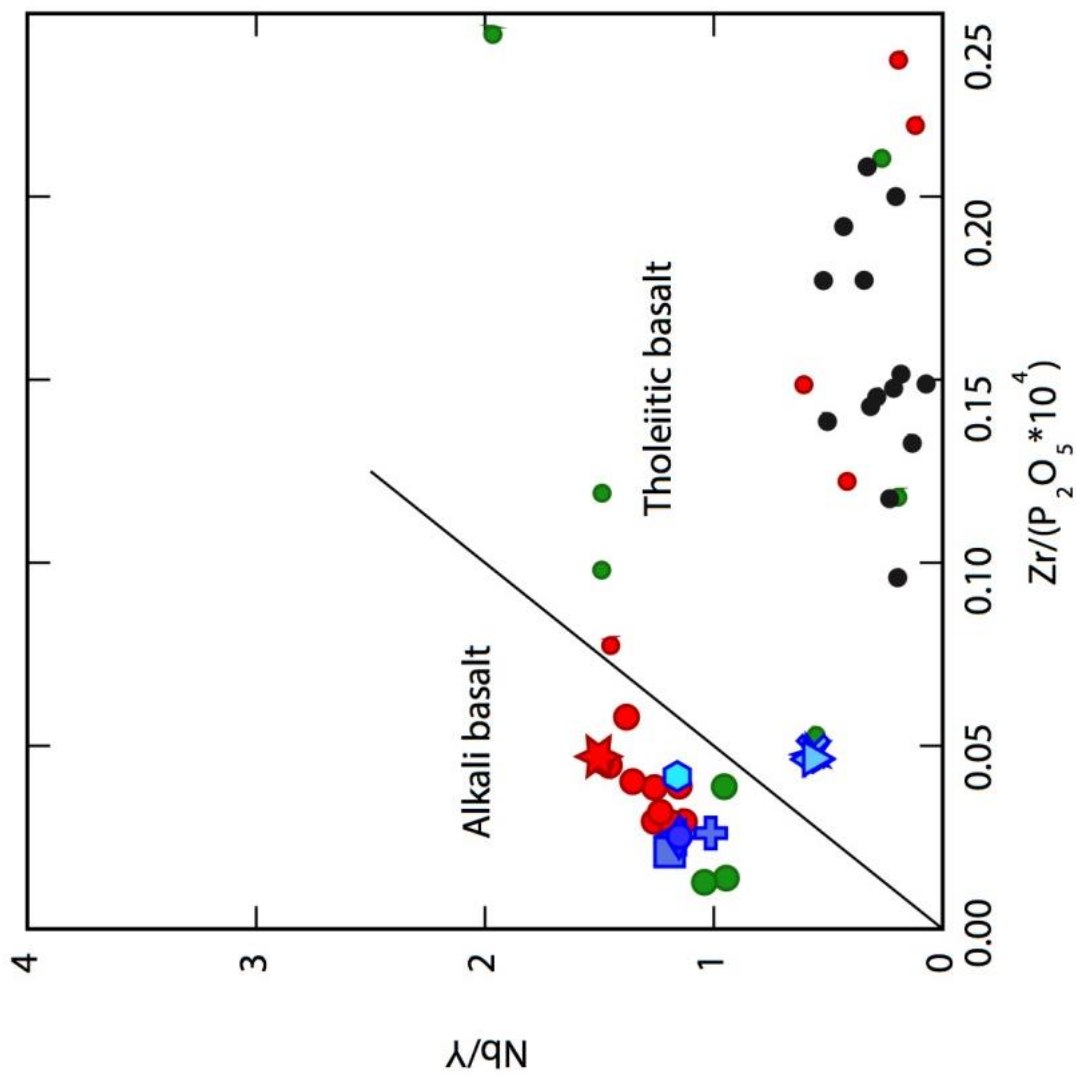


Figure 79. Nb/Y versus $Zr(P_2O_5 * 10^4)$ discrimination diagram of Floyd and Winchester (1975).

Geochemical Conclusions

Throughout Figures 63-79, the Type III samples plot almost on top of each other and the Alamo Creek Basalt, Type I, and bomb samples maintain a firm grouping when only the immobile elements are considered. Collectively, this solidifies the interpretation that the Type III intrusive material is compositionally homogeneous throughout the area. These results also show that the Alamo Creek Basalt, Type I, and phreatomagmatic bombs are quite similar in composition, and any variation in the data for the bombs is likely due to alteration. The Type II sample is consistently different from the other igneous groups in the study area, but show similarities to other basaltic intrusions in the Big Bend area that have yielded ages in the range of the Ash Spring Basalt. However, the Type II intrusion is geochemically distinct from the Ash Spring trachyandesite located nearby and cannot be directly related to that extrusive unit.

Geochronology

Four samples were taken for $^{40}\text{Ar}/^{39}\text{Ar}$ dating, one sample from Alamo Creek Basalt, one from a Type I intrusion, and two from the Type III intrusive diabase. The locations of the samples are shown in Plate I. All four samples were collected from locations which had experienced the least severe weathering, and chemical analyses for the samples are given in Table 1. Amygdules and other foreign material are possible sources for inaccuracy in $^{40}\text{Ar}/^{39}\text{Ar}$ dating, so special care was taken to extract any such materials by hand. Measurement of argon isotopic compositions was conducted at the $^{40}\text{Ar}/^{39}\text{Ar}$ Geochronology Laboratory at Oregon State University by Dan Miggins and coworkers. Groundmass concentrates were analyzed for each sample, and plagioclase was also analyzed in samples JH-54 and JH-58. The age spectra diagrams are shown in Figures 80-83. All four samples yielded good plateaus, and the weighted mean ages for the entire data set for each sample are shown in the figures. The data for the

groundmass concentrates show evidence of recoil in the lower temperature steps, as indicated by the higher age readings at the initial stages of argon release, in the far left of the figure (e.g., Hess and Lippolt, 1986). All of the plateau ages are within error margins of the inverse isochron ages, making it difficult to know which results to use. For consistency, the plateau ages for each sample will be discussed in the text, but the full data sets are in tables for each sample in Appendix I.

Sample JH-55 from the Alamo Creek Basalt in the study area yields a plateau age of 46.77 ± 0.36 Ma, consistent with published results from Alamo Creek flows in other areas (Turner et al., 2011). The Type 1 intrusion (JH-62) yields a plateau age of 46.71 ± 0.33 Ma. Together with the similarity in geochemical composition, the isotopic age data indicate that the Alamo Creek lava in the study area and the Type I intrusion are directly related. Samples JH-54 and JH-58 from the Type III intrusive rocks respectively yield plateau ages of 33.50 ± 0.27 Ma and 33.83 ± 0.31 Ma, consistent with other evidence that the Type III rocks represent a single, homogeneous mass of magma. The ages of these two samples place the Type III intrusive rocks within the timeframe of the Bee Mountain Basalt Member of the Chisos Formation (cf. Turner et al., 2011).

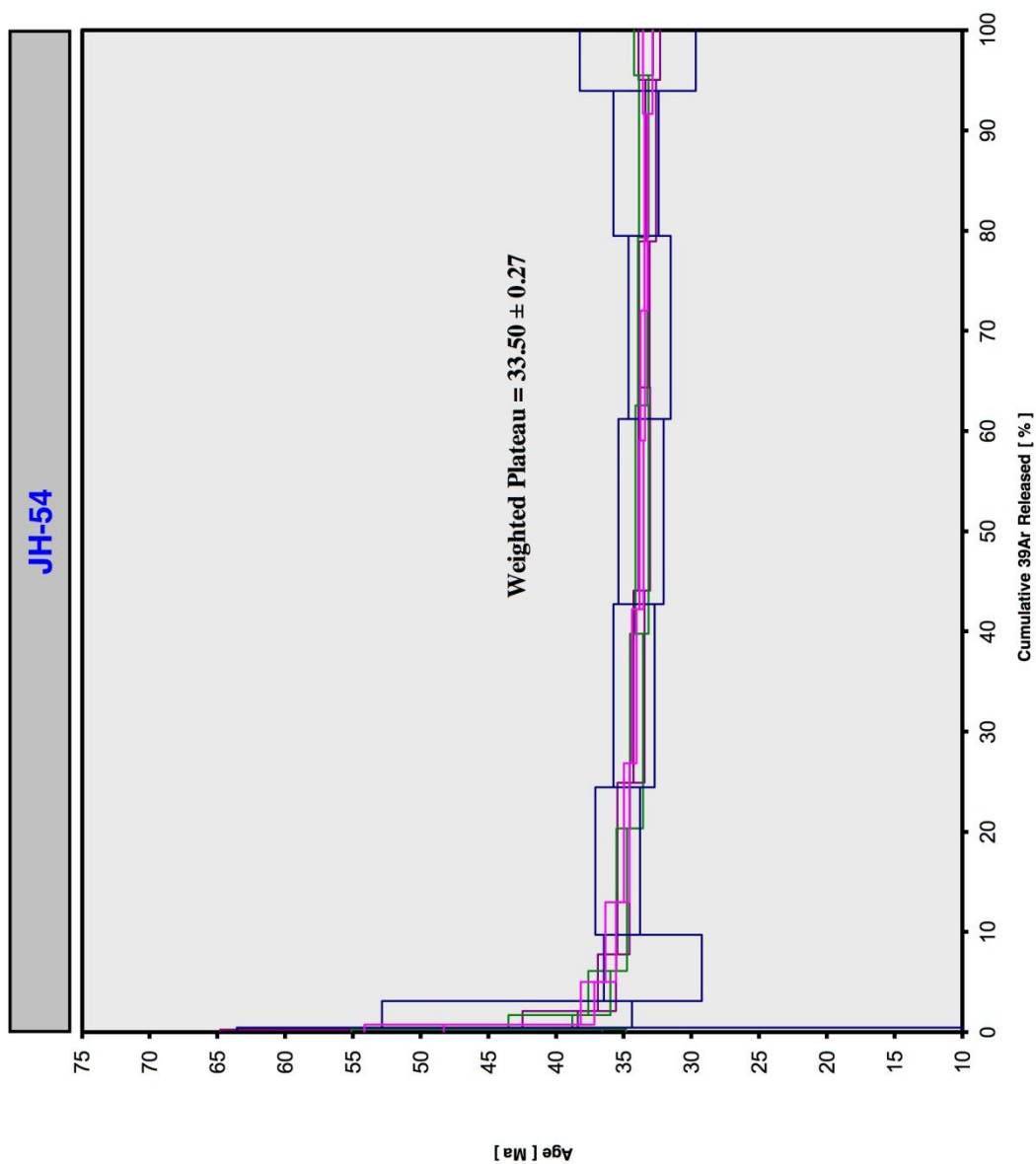


Figure 80. $^{40}\text{Ar}/^{39}\text{Ar}$ age spectra for one plagioclase (purple lines) and three groundmass concentrates for sample JH-54. Cited errors for dates indicated are $\pm 2\sigma$.

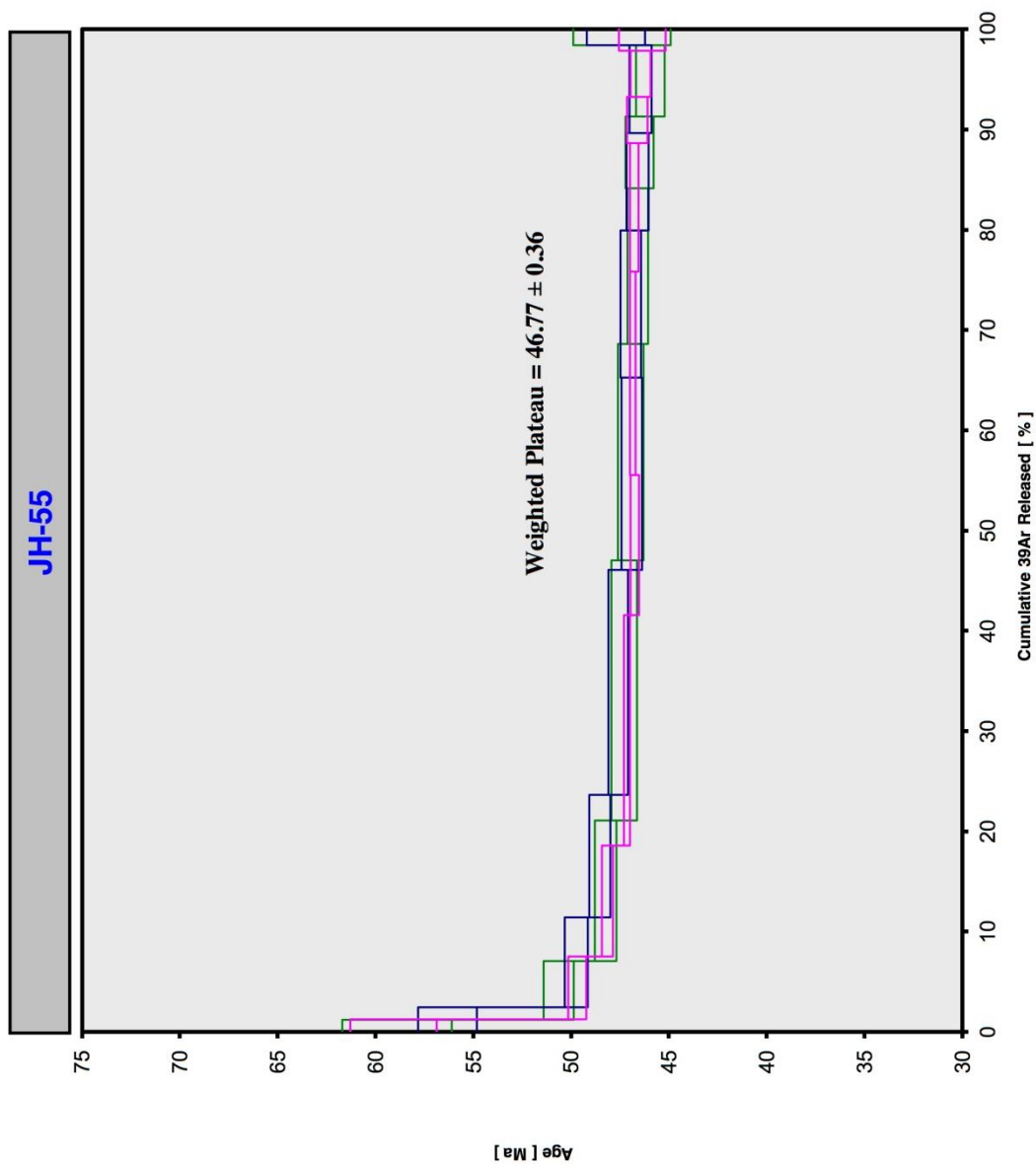


Figure 81. $^{40}\text{Ar}/^{39}\text{Ar}$ age spectra for three groundmass concentrates for sample JH-55. Cited errors for dates indicated are $\pm 2\sigma$.

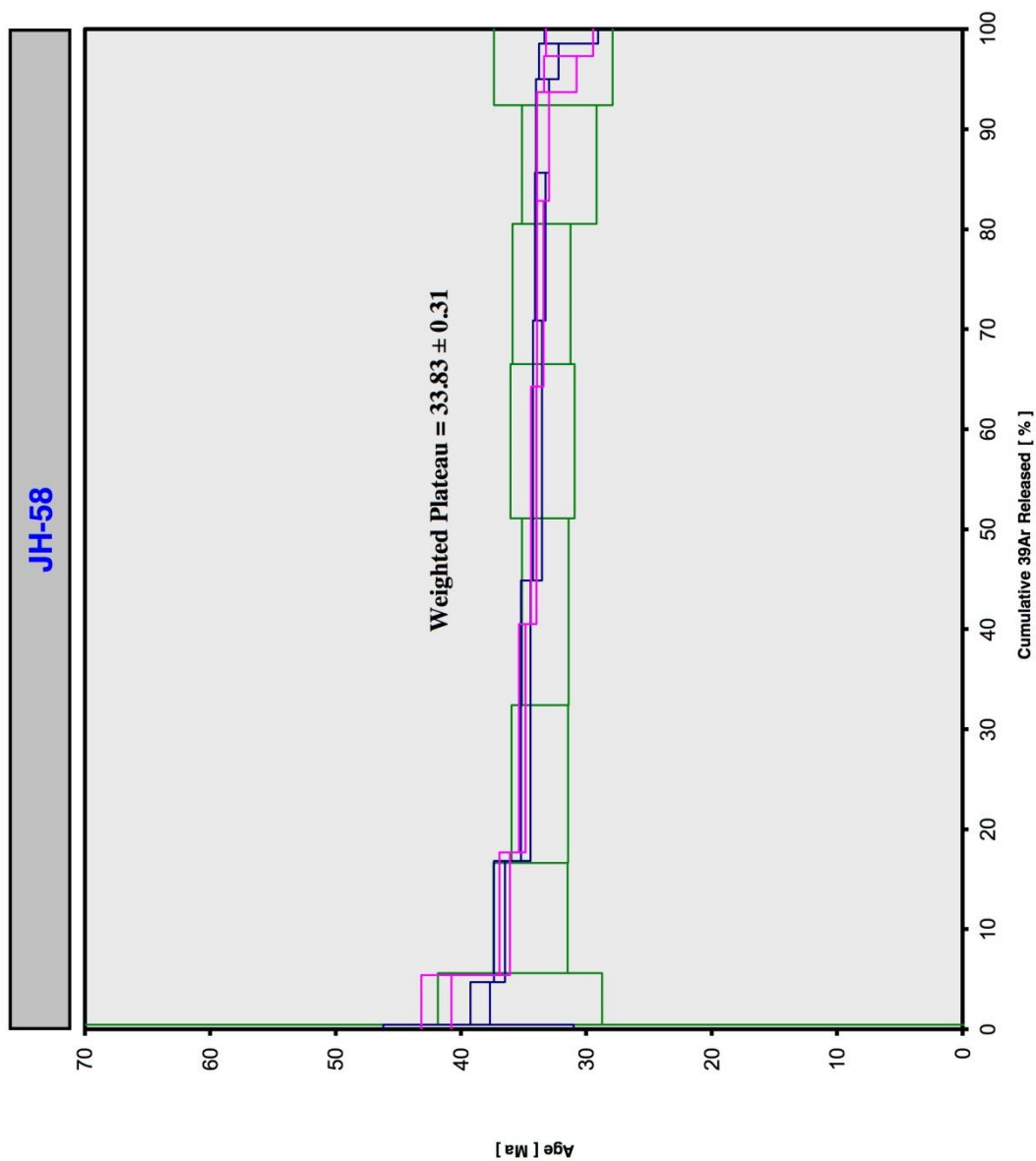


Figure 82. $^{40}\text{Ar}/^{39}\text{Ar}$ age spectra for one plagioclase (green lines) and two groundmass concentrates for sample JH-58. Cited errors for dates indicated are $\pm 2\sigma$.

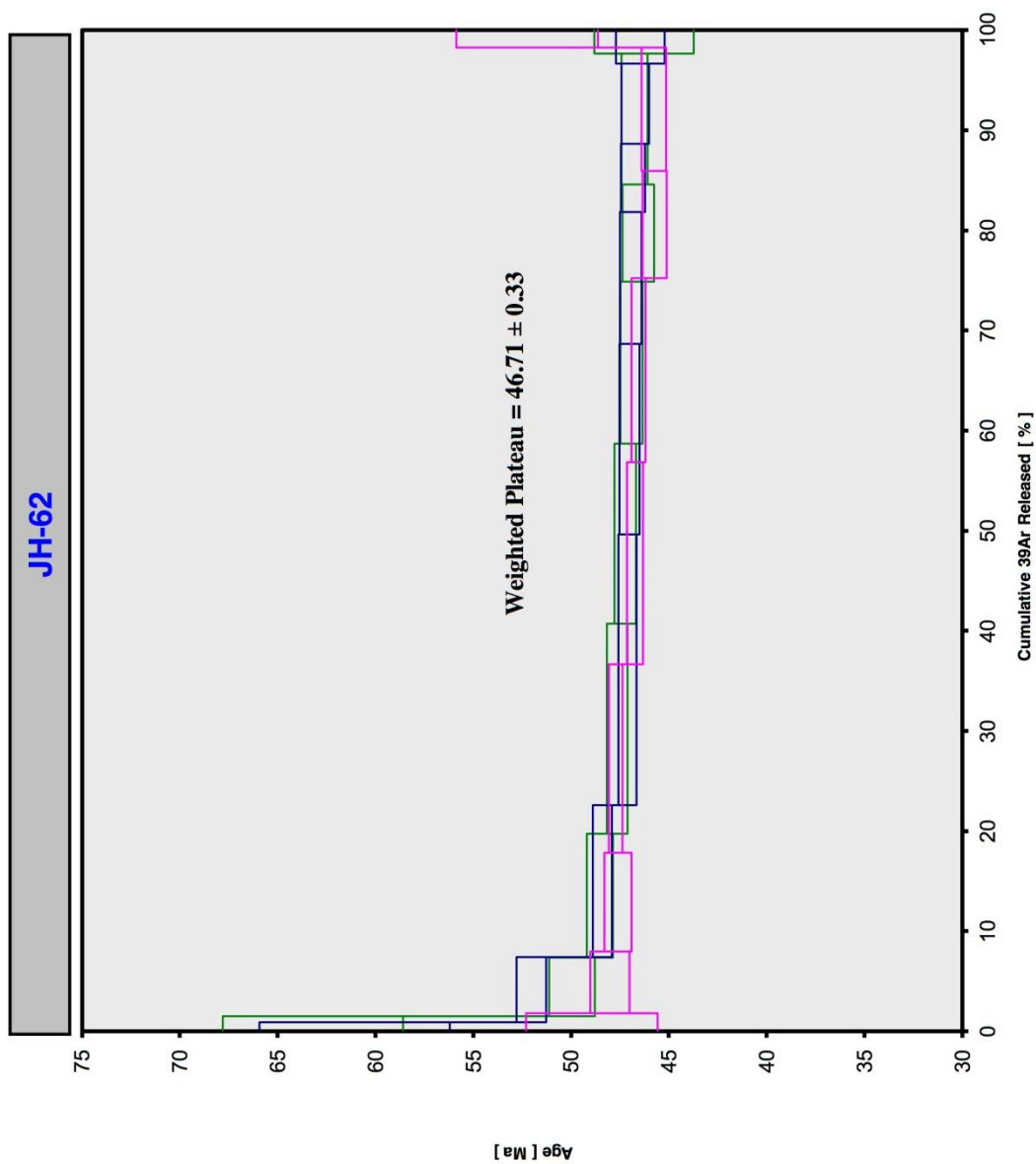


Figure 83. $^{40}\text{Ar}/^{39}\text{Ar}$ age spectra for three groundmass concentrates for sample JH-62. Cited errors for dates indicated are $\pm 2\sigma$.

Chapter 6: Conclusions

The detailed mapping done in the study area east of Peña Mountain has revealed a complex mass of intrusive material and two distinct outcrops of lava within sedimentary units. Three intrusive units were separated in the field through hand-sample examination. Contact relations along with geochemical analyses and $^{40}\text{Ar}/^{39}\text{Ar}$ dates have enabled a temporal context for the units in the study area to be established based on the studies detailed in the previous chapters.

After deposition of sediments of the Black Peaks Formation and subsequent erosion of said unit, igneous activity was initiated in the study area. A lava flow of Alamo Creek Basalt appears to have flowed through the study area in a river channel which was ~ 5 m deep. This river channel is inferred to have been sinuous, looping through the area in a manner which left lava deposits now exposed only at the northern and southern portions of the study area. The conglomeratic sandstone of the Chisos Formation was deposited after this, directly over the flow breccia on the upper margin of the Alamo Creek Basalt flow. At least some other Chisos strata were also deposited during the time before the next igneous activity in the study area: the Type I intrusions. This conclusion is supported by field relations of Type I outcrops. One intrusive tongue of Type I has a well-developed chilled margin against both Alamo Creek Basalt and Black Peaks strata, placing Type I activity after the lava flow cooled thoroughly. The largest outcrop of Type I is in intrusive contact with overlying, strongly baked Chisos strata. Thus, part of the Chisos strata in the study area must have been deposited between the lava flow and Type I intrusive activity. As an aside, the Chisos conglomeratic sandstone was most likely deposited by a river, which is suggestive of the presence of groundwater at relatively shallow levels.

At some point before Type I intrusive activity ceased, an episode of phreatomagmatism occurred, likely due to interaction of groundwater with the intruding magma. Geochemical analyses of two bombs sampled from within the vent-fill material and a sample of the Type I diabase, all of which correspond closely to each other. These samples also show strong geochemical similarities with the Alamo Creek Basalt samples from the study area. Since the outcrops of Alamo Creek Basalt are demonstrably lava flows, they would have been incapable of sourcing large volumes of vent-fill material, despite the vent-like appearance of the spiracle. On the other hand, the Type I diabase has been found intruding the present base of vent-fill outcrops, and the main Type I outcrop is quite close to vent-fill outcrop A, although the exact nature of the contact has been obscured by Type III material. Therefore, the most plausible conclusion is that Type I magma drove the phreatomagmatic episode and later intruded without explosive activity. This theory is corroborated by the $^{40}\text{Ar}/^{39}\text{Ar}$ dates for the Type I and Alamo Creek Basalt study area samples, which are both ~ 47 Ma. Additional support for this theory is found in the geochemical compositions of the samples, which overlap so closely that the best explanation for the correlation is a common magma source, tapped over a relatively short period of time to form the lava, vents, and intrusions.

The original geometry of the phreatomagmatic vents is unknown, due to the large amounts of intrusive rock which surround the vent-fill material. Despite this ambiguity, some deductions can be made about the nature of the phreatomagmatic vents. The close proximity of outcrops B and C, D and E, as well as F and G, respectively, lend themselves to the idea that the vents may have fed coalescing maars. On the other hand, the relatively linear pattern made by outcrops B, C, D, F, and G suggests formation by a phreatomagmatic fissure vent. Of course, the nature of the outcrops prevents confirmation of either theory.

Some time after explosive phreatomagmatism and Type I intrusive activity ceased, Type II intrusive activity is inferred to have occurred. The lack of $^{40}\text{Ar}/^{39}\text{Ar}$ dates for the Type II intrusive material prevents any firm conclusions about the exact timing of this unit, but physical relationships and geochemical evidence suggest that Type II postdates Type I. Physical relationships place Type II after Alamo Creek Basalt extrusion and deposition of some portion of Chisos strata, since Type II crops out at structurally higher levels, and Type III forms a definite chilled margin against Type II, showing that Type II had time to thoroughly cool before Type III intruded. The geochemical evidence is the similar compositions of the analyzed sample of Type II and the 43-42 Ma hypabyssal basaltic intrusions elsewhere in the Big Bend region (Befus et al., 2009; Hanson, unpublished data). Thus, it can be reasonably deduced that Type II is compositionally related to these intrusions and therefore falls into the same timeframe. However, Type II bears no lithological resemblance to the nearest exposure of Ash Spring lava, and in fact shows a less evolved geochemical composition. Therefore, it may be concluded that despite the overlapping timeframe, the Type II and other related intrusive activity were not sourced from the same magma batch as the Ash Spring lava sampled for this study or the comparison Ash Spring Basalt units.

Around 34 Ma, Type III material intruded the study area. This was quite some time after Type II emplacement had ceased, judging by the chilled margin on Type III. Interestingly, where Type II is present, it seems to have acted as an impenetrable cap, blocking the Type III magma from rising further and instead causing it to spread laterally. The surrounding Chisos sediments provided little resistance to the Type III intrusion, allowing it to form complex sheets and billowed margins. This indicates that the Chisos sediments were still poorly lithified at the time of the Type III intrusion. Despite their poorly lithified state, it is likely that there was relatively

little groundwater in the strata at this time, as evidenced by only sparse occurrences of peperite along Type III intrusive margins. The lack of any explosive interaction between Type III and the surrounding sediment lends credence to this supposition.

The exceptional degree of similarity in the geochemistry of all four samples of Type III material indicates a common source of magma and emplacement over a short period of time. This suggests a quick succession of intrusions from the same magma chamber or one large intrusion of magma. The large outcrop area and complexity of the Type III intrusive rocks seem to point to the former theory. However, no evidence of contacts between separate units of Type III rocks was found during the extensive mapping, despite the large amount of outcrop covered on foot. Also, the small-scale contortions of the Type III intrusions suggest that a larger scale complexity of the intrusions is not unrealistic. Thus, it is inferred that Type III represents a single, large, complex intrusive body of homogeneous diabase.

In the time since the intrusion of Type III, erosion and faulting have been the primary modifiers of the study area. Basin and Range faulting juxtaposed white Chisos strata against dark brown Alamo Creek Basalt and red-brown Black Peaks strata. These contacts were transformed into dramatic outcrops by the extensive erosion that took place in the study area. This erosion also unveiled the complex network of intrusions and vent-fill material which prompted the choice of the area east of Peña Mountain for this thesis.

Appendix I

$^{40}\text{Ar}/^{39}\text{Ar}$ Dating Techniques

Two different sample types (groundmass and plagioclase) were prepared for $^{40}\text{Ar}/^{39}\text{Ar}$ age analyses, each requiring a slightly different preparation. Preparation of the groundmass samples began by using a rock saw to remove visibly obvious alteration. Next, these samples were crushed using a porcelain jaw crusher and ground into different size fractions. Samples were cleaned and then run through a Frantz magnetic separator. The magnetic portions collected at each amperage setting were examined under a microscope and the best portions (based on sample purity) were cleaned by acid leaching. Lastly, the groundmass samples were hand-picked using a binocular microscope. Approximately 100-80 mg of groundmass material was collected from each sample for the $^{40}\text{Ar}/^{39}\text{Ar}$ dating. The plagioclase samples were separated into different fractions using the Frantz magnetic separator. The non-magnetic portion of the sample remaining after the magnet was run at its maximum amperage typically contained most of the unaltered plagioclase grains and was further cleaned by acid-leaching. Finally the samples were hand-picked to remove any altered feldspar grains or feldspar grains partly holding pieces of other minerals or groundmass. Approximately 100-30 mg of feldspar was collected from each sample.

Following sample preparation and hand-picking the samples were irradiated for 6 hours in the USGS TRIGA nuclear reactor in Denver, Colorado. The $^{40}\text{Ar}/^{39}\text{Ar}$ incremental heating age determinations were performed using a continuous 10W CO_2 laserprobe combined with a MAP-215/50 mass spectrometer at Oregon State University. Software allowed for scanning across samples in preset patterns with a defocused laser beam, to evenly heat the geological materials. All ages were calculated using the corrected Steiger and Jäger (1977) decay constant of $5.530 \pm 0.097 \times 10^{-10}$ 1/yr (2σ) as reported by Min *et al.* (2000). For a detailed description of the

analytical facility and the constants used in the age calculations, refer to Table 2 in Koppers *et al.* (2003). Incremental heating plateau ages and isochron ages were calculated using the Ar/ArCALC v2.5 software from Koppers (2002) that is available from the <http://earthref.org/tools/ararcalc.htm> website. All errors on the $^{40}\text{Ar}/^{39}\text{Ar}$ ages are reported at the 95% confidence level (2σ), unless otherwise indicated, including typical 0.3-0.5% uncertainties in the J-value. Total fusion ages were also calculated using the ArArCALC software. Plateau ages and isochrons with MSWD's higher than 1 were taken to indicate an increased scatter due to geological uncertainties beyond the precision of the individual increment ages themselves. In these cases, the reported analytical errors are multiplied by the $\sqrt{\text{MSWD}}$ (York 1969; Kullerud 1991).

⁴⁰Ar/³⁹Ar Data Tables

Table 2: ⁴⁰Ar/³⁹Ar incremental heating data for sample JH-54

Incremental Heating	36Ar(a) [V]	37Ar(ca) [V]	38Ar(cl) [V]	39Ar(k) [V]	40Ar(r) [V]	Age ± 2σ (Ma)	40Ar(r) (%)	39Ar(k) (%)	K/Ca ± 2σ
13C2954	0.0015815	0.0079136	0.0000000	0.0050635	0.084165	51.22 ± 2.93	15.26	0.23	0.275 ± 0.014
13C2956	0.0001244	0.0377674	0.0000118	0.0276276	0.336425	37.67 ± 0.50	90.09	1.27	0.315 ± 0.014
13C2957	0.0000464	0.0627542	0.0000191	0.0516030	0.599667	35.96 ± 0.38	97.68	2.38	0.354 ± 0.015
13C2959	0.0000333	0.1010801	0.0000252	0.0899805	1.010593	34.77 ± 0.19	98.95	4.15	0.383 ± 0.016
13C2960	0.0000253	0.1088773	0.0000223	0.0998384	1.103432	34.22 ± 0.17	99.24	4.60	0.394 ± 0.017
13C2962	0.0000240	0.1261235	0.0000382	0.1092295	1.188001	33.68 ± 0.16	99.31	5.04	0.372 ± 0.016
13C2963	0.0000266	0.1037263	0.0000349	0.0842326	0.913683	33.59 ± 0.15	99.06	3.88	0.349 ± 0.015
13C2965	0.0000424	0.2176256	0.0001242	0.1277817	1.376201	33.35 ± 0.11	99.01	5.89	0.252 ± 0.011
13C2967	0.0000325	0.1075359	0.0000591	0.0540877	0.580062	33.21 ± 0.35	98.28	2.49	0.216 ± 0.009
Σ	0.0036401	4.0297065	0.0030353	2.1682630	23.928298				

Sample = JH-54 HANSON GM 5C6-13

Material = Groundmass

Analyst = Julia Klath

Irradiation = OSU5C13

J = 0.00173264 ± 0.00000674

FCT-3 = 28.030 ± 0.003 Ma

Results	40(r)/39(k) ± 2σ	Age ± 2σ (Ma)	Σ	Σ	39Ar(k) (%·n)	K/Ca ± 2σ
Age Plateau Error Mean	10.81586 ± 0.03068 ± 0.28%	33.50 ± 0.27 ± 0.82%	2.05	72.34	0.040 ± 0.024	
	Minimal External Error Analytical Error	± 0.60 ± 0.09	1.63	21	2σ Confidence Limit Error Magnification	
Total Fusion Age	11.03570 ± 0.03101 ± 0.28%	34.17 ± 0.28 ± 0.82%	1.4335	36	0.231 ± 0.002	
	Minimal External Error Analytical Error	± 0.61 ± 0.10				

Plateau and Isochron ages:

Sample JH-54 GM Plateau Age: 33.40 +/- 0.36 Ma; Inverse Isochron Age: 34.69 +/- 1.51 Ma

Sample JH-54 GM Plateau Age: 33.61 +/- 0.20 Ma; Inverse Isochron Age: 33.48 +/- 0.36 Ma

Sample JH-54 GM Plateau Age: 33.48 +/- 0.31 Ma; Inverse Isochron Age: 34.52 +/- 1.03 Ma

Sample JH-54 Plagioclase Plateau Age: 34.05 +/- 0.71 Ma; Inverse Isochron Age: 35.51 +/- 0.65 Ma

Table 3: $^{40}\text{Ar}/^{39}\text{Ar}$ Ar incremental heating data for sample JH-55

Incremental Heating	$^{36}\text{Ar}(a)$ [V]	$^{37}\text{Ar}(ca)$ [V]	$^{38}\text{Ar}(cl)$ [V]	$^{39}\text{Ar}(k)$ [V]	$^{40}\text{Ar}(r)$ [V]	Age $\pm 2\sigma$ (Ma)	$^{40}\text{Ar}(r)$ (%)	$^{39}\text{Ar}(k)$ (%)	K/Ca $\pm 2\sigma$
13C2938	500 °C	0.0023515	0.0141511	0.0000164	0.0090729	0.171747	19.82	0.44	0.276 \pm 0.013
13C2940	600 °C	0.0001827	0.0529862	0.0000045	0.0457289	0.726080	93.02	2.21	0.371 \pm 0.016
13C2941	700 °C	0.0000840	0.0805793	0.0000056	0.0810349	1.246264	97.98	3.92	0.432 \pm 0.019
13C2943	800 °C	0.0001001	0.1814849	0.0000210	0.1676047	2.523853	98.78	8.10	0.397 \pm 0.017
13C2944	850 °C	0.0000457	0.1127223	0.0000064	0.1022651	1.526496	99.06	4.94	0.390 \pm 0.017
13C2946	950 °C	0.0000223	0.1619314	0.0000574	0.1481385	2.215994	99.64	7.16	0.393 \pm 0.017
13C2947	1050 °C	0.0000464	0.1080203	0.0000390	0.0933829	1.394690	98.96	4.52	0.372 \pm 0.016
13C2949	1150 °C	0.0000376	0.0454943	0.0000355	0.0338521	0.503846	97.78	1.64	0.320 \pm 0.014
13C2950	1250 °C	0.0000914	0.0622793	0.0000297	0.0334810	0.496670	94.78	1.62	0.231 \pm 0.010
13C2952	1400 °C	0.0000896	0.0412044	0.0000282	0.0156559	0.231720	89.69	0.76	0.163 \pm 0.007
Σ		0.0085929	2.7369592	0.0012148	2.0681115	31.368152			

Sample = JH-55 HANSON GM 5C4-13

Material = Groundmass

Analyst = Julia Klath

Irradiation = OSU5C13

J = 0.00175845 \pm 0.00000674FCT-3 = 28.030 \pm 0.003 Ma**Results****Age Plateau**
Error Mean14.93560 \pm 0.02852
 \pm 0.19%Minimal External Error \pm 0.83
Analytical Error \pm 0.0946.77 \pm 0.36
 \pm 0.78%1.02
43%
1.71
2 σ Confidence Limit
Error Magnification**Total Fusion Age**15.16753 \pm 0.03615
 \pm 0.24%Minimal External Error \pm 0.84
Analytical Error \pm 0.1147.49 \pm 0.38
 \pm 0.79%1.0114
28
0.325 \pm 0.003

Plateau and Isochron ages:

Sample JH-55 GM Plateau Age: 46.63 \pm 0.39 Ma; Inverse Isochron Age: 45.50 \pm 1.54 MaSample JH-55 GM Plateau Age: 46.83 \pm 0.38 Ma; Inverse Isochron Age: 47.89 \pm 1.39 MaSample JH-55 GM Plateau Age: 46.78 \pm 0.37 Ma; Inverse Isochron Age: 46.68 \pm 0.37 Ma

Table 4: $^{40}\text{Ar}/^{39}\text{Ar}$ Ar incremental heating data for sample JH-58

Incremental Heating	36Ar(a) [V]	37Ar(ca) [V]	38Ar(cl) [V]	39Ar(k) [V]	40Ar(r) [V]	Age (Ma)	Age $\pm 2\sigma$ (Ma)	40Ar(r) (%)	39Ar(k) (%)	K/Ca	$\pm 2\sigma$
13C2969	650 °C	0.0020940	0.0309455	0.0000099	0.0201924	0.268429	41.97 \pm 1.20	30.25	1.71	0.281	\pm 0.012
13C2971	750 °C	0.0000233	0.0559835	0.0000069	0.0456923	0.527342	36.49 \pm 0.42	98.63	3.87	0.351	\pm 0.015
13C2972	850 °C	0.0000117	0.0881416	0.0000130	0.0850120	0.943341	35.10 \pm 0.25	99.54	7.19	0.415	\pm 0.018
13C2973	950 °C	0.0000213	0.0935925	0.0000247	0.0883010	0.954471	34.20 \pm 0.22	99.25	7.47	0.406	\pm 0.017
13C2975	1050 °C	0.0000236	0.1028155	0.0000526	0.0692402	0.736468	33.66 \pm 0.26	98.97	5.86	0.290	\pm 0.012
13C2976	1150 °C	0.0000250	0.0910685	0.0000579	0.0403782	0.426782	33.45 \pm 0.48	98.21	3.42	0.191	\pm 0.008
13C2978	1250 °C	0.0000398	0.0397027	0.0000189	0.0134406	0.136195	32.08 \pm 1.30	91.97	1.14	0.146	\pm 0.006
13C2979	1400 °C	0.0000715	0.0553444	0.0000295	0.0100561	0.099470	31.32 \pm 1.88	82.40	0.85	0.078	\pm 0.003
Σ		0.0036178	2.7266123	0.0018658	1.1821015	12.920157					

Sample = JH-58 GM 5C3-13

Material = Groundmass

Analyst = Trevor Smith

Irradiation = OSU5CT13

J = 0.00177058 \pm 0.00000674FCT-3 = 28.030 \pm 0.003 Ma

Results	40(r)/39(k) $\pm 2\sigma$	Age $\pm 2\sigma$ (Ma)	MSW \square	39Ar(k) (%,n)	K/Ca	$\pm 2\sigma$
Age Plateau	10.69234 \pm 0.05520	33.83 \pm 0.31	1.82	56.65	0.035	\pm 0.014
Error Mean	\pm 0.52%	\pm 0.91%	3%	15		
	Minimal External Error	\pm 0.62	1.76	2 σ Confidence Limit		
	Analytical Error	\pm 0.17	1.3506	Error Magnification		
Total Fusion Age	10.92982 \pm 0.04516	34.58 \pm 0.30		26	0.186	\pm 0.002
	\pm 0.41%	\pm 0.86%				
	Minimal External Error	\pm 0.62				
	Analytical Error	\pm 0.14				

Plateau and Isochron ages:

Sample JH-58 GM Plateau Age: 33.76 \pm 0.30 Ma; Inverse Isochron Age: 34.07 \pm 0.25 MaSample JH-58 GM Plateau Age: 33.92 \pm 0.50 Ma; Inverse Isochron Age: 35.14 \pm 1.50 MaSample JH-58 Plagioclase Plateau Age: 33.45 \pm 0.96 Ma; Inverse Isochron Age: 30.78 \pm 7.65 Ma

Table 5: $^{40}\text{Ar}/^{39}\text{Ar}$ Ar incremental heating data for sample JH-62

Incremental Heating	36Ar(a) [V]	37Ar(ca) [V]	38Ar(cl) [V]	39Ar(k) [V]	40Ar(r) [V]	Age $\pm 2\sigma$ (Ma)	40Ar(r) (%)	39Ar(k) (%)	K/Ca $\pm 2\sigma$
13C3980	500 °C	0.0004431	0.0160348	0.0000109	0.151596	48.94 \pm 3.36	53.64	0.65	0.188 \pm 0.009
13C3982	600 °C	0.0001338	0.0392070	0.0000232	0.500874	48.01 \pm 1.01	92.64	2.20	0.259 \pm 0.012
13C3983	700 °C	0.0000809	0.0528069	0.0000369	0.0379150	47.61 \pm 0.69	97.04	3.52	0.309 \pm 0.014
13C3985	800 °C	0.0000440	0.0934669	0.0000620	1.522225	47.72 \pm 0.36	99.11	6.72	0.333 \pm 0.015
13C3986	900 °C	0.0000489	0.0882912	0.0000917	1.600007	46.73 \pm 0.41	99.06	7.21	0.378 \pm 0.017
13C3988	1000 °C	0.0000504	0.0934158	0.0001022	1.449404	46.54 \pm 0.36	98.94	6.56	0.325 \pm 0.014
13C3989	1100 °C	0.0000658	0.0908255	0.0000769	0.829680	45.73 \pm 0.61	97.66	3.82	0.195 \pm 0.009
13C3991	1250 °C	0.0001073	0.2300769	0.0001260	0.0473126	45.77 \pm 0.63	96.74	4.40	0.088 \pm 0.004
13C3993	1400 °C	0.0000420	0.0450015	0.0000160	0.0067527	52.25 \pm 3.62	108.59	0.63	0.065 \pm 0.003
	Σ	0.0081031	2.1002528	0.0007707	1.0763425				

Sample = JH-62 GM 6C9-13

Material = Groundmass (<180)

Analyst = Julia Klath

Irradiation = OSU6C13

J = 0.00127308 \pm 0.00000345FCT-3 = 28.030 \pm 0.003 Ma

Results	40(r)/39(k) $\pm 2\sigma$	Age $\pm 2\sigma$ (Ma)	$\frac{M}{\Sigma W}$	39Ar(k) (% n)	K/Ca $\pm 2\sigma$
Age Plateau	20.60250	46.71	2.14	66.20	0.078 \pm 0.037
Error Mean	± 0.09608 $\pm 0.47\%$	± 0.33 $\pm 0.71\%$	1%	15	
	Minimal External Error ± 0.81 Analytical Error ± 0.22		1.76	2 σ Confidence Limit Error Magnification	
Total Fusion Age	20.91512	47.41	1.4643	27	0.220 \pm 0.003
	± 0.05783 $\pm 0.28\%$	± 0.28 $\pm 0.60\%$			
	Minimal External Error ± 0.80 Analytical Error ± 0.13				

Plateau and Isochron ages:

Sample JH-62 GM Plateau Age: 46.38 \pm 0.52 Ma; Inverse Isochron Age: 47.12 \pm 0.48 MaSample JH-62 GM Plateau Age: 47.00 \pm 0.35 Ma; Inverse Isochron Age: 47.07 \pm 0.37 MaSample JH-62 GM Plateau Age: 46.97 \pm 0.42 Ma; Inverse Isochron Age: 47.06 \pm 0.43 Ma

References

- Barker, D.S., 1977, Northern Trans-Pecos magmatic province: Introduction and comparison with the Kenya rift: *Geological Society of America Bulletin*, 88: 1421-1427.
- Barker, D.S., 1987, Tertiary alkaline magmatism in Trans-Pecos Texas, *in* Fitton, J.G., and Upton, B.G.J., eds., *Alkaline Igneous Rocks*: Geological Society, London, Special Publication, 30: 415-431.
- Befus, K.S., Hanson, R.E., Lehman, T.M., and Griffin, W.R., 2008, Cretaceous basaltic phreatomagmatic volcanism in West Texas: Maar complex at Peña Mountain, Big Bend National Park: *Journal of Volcanology and Geothermal Research*, 173: 245-264.
- Befus, K.S., Hanson, R.E., Miggins, D.P., Breyer, J.A., and Busbey, A.B., 2009, Nonexplosive and explosive magma/wet-sediment interaction during emplacement of Eocene intrusions into Cretaceous to Eocene strata, Trans-Pecos igneous province, West Texas: *Journal of Volcanology and Geothermal Research*, 181: 155-172.
- Breyer, J.A., Busbey, A.B., III, Hanson, R.E., Befus, K.E., Griffin, W.R., Hargrove, U.S., and Bergman, S.C., 2007, Evidence for Late Cretaceous volcanism in Trans-Pecos Texas: *Journal of Geology*, 115: 243-251.
- Carman, Jr., M.F., Stewart, R.M., and Casey, J.F., 2003, Characterization of the Alamo Creek Basalt, Big Bend National Park, Texas: *Texas Journal of Science*, 55: 99-128.
- Cas, R.H.F., and Wright, J.V., 1987, *Volcanic Successions: Modern and Ancient*: London: Allen & Unwin, 528 p.
- Deitz, J.E., Hanson, R.E., Miggins, D.P., and Winkler, C.E., 2010, Eocene(?) basaltic dike-sill network and phreatomagmatic vents emplaced into unlithified Cretaceous to Paleocene strata, Study Butte area, Big Bend National Park, West Texas: *Geological Society of America Abstracts with Programs*, 42: 106.
- English, J.M., Johnston, S.T., and Wang, K., 2003, Thermal modelling of the Laramide orogeny: testing the flat-slab subduction hypothesis: *Earth and Planetary Science Letters*, 214: 619-632.
- Erdlac Jr., R.J., 1990, A Laramide-age push-up block: The structures and formation of the Terlingua-Solitario structural block, Big Bend region, Texas: *Geological Society of America Bulletin*, 102: 1,065-1,076.
- Floyd, P.A., and Winchester, J.A., 1975, Magma type and tectonic setting discrimination using immobile elements: *Earth and Planetary Science Letters*, v. 27, p. 211-218.
- Gilmer, A.K., Kyle, J.R., Connelly, J.H., Mathur, R.D., and Henry, C.D., 2003, Extension of Laramide magmatism in southwestern North America into Trans-Pecos Texas: *Geology*, 31: 447-450.
- Hanson, R.E. and Elliot, D.H., 1996, Rift-related Jurassic basaltic phreatomagmatic volcanism in the central Transantarctic Mountains: Precursory stage to flood-basalt effusion, *Bulletin of Volcanology*, 58: 327-347.

- Henry, C.D., and Davis, L.L., 1996, Tertiary volcanic, volcanoclastic, and intrusive rocks adjacent to the Solitario, *in* Henry, C.D., and Muehlberger, W.R., eds., *Geology of Solitario Dome, Trans-Pecos Texas*: University of Texas at Austin: Bureau of Economic Geology Report of Investigations no. 240, 81-105.
- Henry, C.D., and McDowell, F.W., 1986, Geochronology of magmatism in the Tertiary volcanic field, Trans-Pecos Texas, *in* Price, J.G., Henry, C.D., Parker, D.F., and Barker, D.S., eds., 1986, *Igneous Geology of Trans-Pecos Texas, Field Trip Guide and Research Articles*: The University of Texas at Austin, Bureau of Economic Geology, Guidebook 23: 99-122.
- Henry, C.D., and Price, J.G., 1986, Early basin and range development in Trans-Pecos Texas and adjacent Chihuahua: Magmatism and orientation, timing, and style of extension: *Journal of Geophysical Research*, 91: 6,213-6,224.
- Henry, C.D., Price, J.G., and James, E.W., 1991, Mid-Cenozoic stress evolution and magmatism in the southern Cordillera, Texas and Mexico: Transition from continental arc to intraplate extension: *Journal of Geophysical Research*, 96: 13,545-13,560.
- Hess, J.C., and Lippolt, H.J., 1986, Kinetics of Ar isotopes during neutron irradiation: ^{39}Ar loss from minerals as a source of error in $^{40}\text{Ar}/^{39}\text{Ar}$ dating: *Chemical Geology, Isotope Geoscience Section*, 59:223-236.
- Hill, J.A., Hanson, R.E., Miggins, D.P., Deitz, J.E., Befus, K.S., and Winkler, C.E., 2012, Magma plumbing systems for Eocene basaltic maar volcanoes and phreatomagmatic fissure vents in the Trans-Pecos igneous province, West Texas: Abstracts, Hopi Buttes Volcanic Field Workshop, Arizona, October 21-27 (sponsored by the International Association of Sedimentologists and the International Association of Volcanology and Chemistry of the Earth's Interior), p. 63.
- Hooten, J.A., and Ort, M.H., 2002, Peperite as a record of early-stage phreatomagmatic fragmentation processes: An example from the Hopi Buttes volcanic field, Navajo Nation, Arizona, USA: *Journal of Volcanology and Geothermal Research*, 114: 95-106.
- Hughes, C.J., 1973, Spilites, keratophyres, and the igneous spectrum: *Geological Magazine*, 109.6: 513-527.
- James, E.W. and Henry, C.D., 1991, Compositional changes in Trans-Pecos Texas magmatism coincident with Cenozoic stress realignment: *Journal of Geophysical Research*, 96: 13,561-13,575.
- Keating, G.N., Valentine, G.A., Krier, D.J., and Perry, F.V., 2008, Shallow plumbing systems for small-volume basaltic volcanoes: *Bulletin of Volcanology*, 70: 563-582.
- Kokelaar, B.P., 1982, Fluidization of wet sediments during the emplacement and cooling of various igneous bodies: *Journal of the Geological Society of London*, 139: 21-33.
- Koppers, A.A.P., 2002, ArArCALC; software for $^{40}\text{Ar}/^{39}\text{Ar}$ age calculations: *Computers & Geosciences*, 28.5: 605-619.
- Koppers, A.A.P., Staudigel, H., and Duncan, R.A., 2003, High-resolution $^{40}\text{Ar}/^{39}\text{Ar}$ dating of the oldest oceanic basement basalts in the western Pacific basin: *Geochemistry, Geophysics, Geosystems*, 4.11: 1-20.

- Krynauw, J.R., Behr, H.-J., and van den Kerkhof, A.M., 1994, Sill emplacement in wet sediments: fluid inclusion and cathodoluminescence studies at Grunehogna, western Dronning Maud Land, Antarctica: *Journal of the Geological Society, London*, 151: 777-794.
- Kullerud, L., 1991, On the calculation of isochrons: *Chemical Geology; Isotope Geoscience Section*, 87.2: 115-124.
- Lawton, T.F., and McMillan, N.J., 1999, Arc abandonment as a cause for passive continental rifting: Comparison of the Jurassic Mexican Borderland rift and the Cenozoic Rio Grande rift: *Geology*, 27: 779-782.
- Le Bas, M.J., LeMaitre, R.W., Streckeisen, A., and Zanettin, B., 1986, A chemical classification of volcanic rocks based on the total alkali silica diagram: *Journal of Petrology*, v. 27, p. 745-750.
- Lehman, T.M., 1985, Stratigraphy, sedimentology, and paleontology of Upper Cretaceous (Campanian-Maastrichtian) sedimentary rocks in Trans-Pecos Texas: University of Texas at Austin: Ph.D. dissertation, 299 p.
- Lorenz, V., 1986, On the growth of maars and diatremes and its relevance to the formation of tuff rings: *Bulletin of Volcanology*, 48: 265-274.
- Lorenz, V., 1987, Phreatomagmatism and its relevance: *Chemical Geology*, 62: 149-156.
- Lorenz, V., 2003, Maar-diatreme volcanoes, their formation, and their setting in hard-rock or soft-rock environments: *GeoLines*, 15: 72-83.
- Lorenz, V., and Kurszlaukis, S., 2007, Root zone process in the phreatomagmatic pipe emplacement model and consequences for the evolution of maar-diatreme volcanoes: *Journal of Volcanology and Geothermal Research*, 159: 4-32.
- Lorenz, V., Zimanowski, B., and Buettner, R., 2002, On the formation of deep-seated subteranean peperite-like magma-sediment textures: *Journal of Volcanology and Geothermal Research*, 114: 107-118.
- Maxwell, R.A., Lonsdale, J.T., Hazzard, R.T., and Wilson, J.A., 1967, *Geology of Big Bend National Park, Brewster Country, Texas*: The University of Texas at Austin: Bureau of Economic Geology Publication 6,711, 320 p.
- McClintock, M., and White, J.D.L., 2006, Large phreatomagmatic vent complex at Coombs Hills, Antarctica: Wet, explosive initiation of flood basalt volcanism in the Ferrar-Karoo LIP: *Bulletin of Volcanology*, 68: 215-239.
- Meschede, M., 1986, A method of discriminating between different types of mid-ocean basalts and continental tholeiites with the Nb–Zr–Y diagram: *Chemical Geology*, v. 56, p. 207-218.
- Miggins, D.P., 2009, Temporal and geochemical insights related to volcanic and plutonic activity within Big Bend National Park, Texas: University of Texas at El Paso: Ph.D dissertation, 310 p.

- Min, K., Mundil, R., Renne, P.R., and Ludwig, K.R., 2000, A test for systematic errors in $^{40}\text{Ar}/^{39}\text{Ar}$ geochronology through comparison with U/Pb analysis of a 1.1-Ga rhyolite: *Geochimica et Cosmochimica Acta*, 64.1: 73-98.
- Muehlberger, W.R., and Dickerson, P.W., 1989, A tectonic history of Trans-Pecos Texas, *in* Muehlberger, W.R., and Dickerson, P.W., eds., *Structure and Stratigraphy of Trans-Pecos Texas: International Geological Congress, 28th, Field Trip Guidebook T317*: 35-54.
- Németh, K., and Martin, U., 2007, Shallow sill and dyke complex in western Hungary as a possible feeding system of phreatomagmatic volcanoes in "soft-rock" environment: *Journal of Volcanology and Geothermal Research*, 159: 138-152.
- Németh, K., and White, J.D.L., 2003, Reconstructing eruption processes of a Miocene monogenetic volcanic field from vent remnants: Waipiata Volcanic Field, South Island, New Zealand: *Journal of Volcanology and Geothermal Research*, 124: 1-21.
- Page, W.R., Turner, K.J., and Bohannon, R.G., 2008, Tectonic history of Big Bend National Park, *in* Gray, J.E., and Page, W.R., eds., *Geological, geochemical, and geophysical studies by the U.S. Geological Survey in Big Bend National Park, Texas: U.S. Geological Survey Circular 1327*.
- Parker, D.F., Ren, M., Adams, D.T., Tsai, H., and Long, L.E., 2012, Mid-Tertiary magmatism in western Big Bend National Park, Texas, U.S.A.: Evolution of basaltic source regions and generation of peralkaline rhyolite: *Lithos*, 144-145: 161-176.
- Pearce, J.A., 1982, The role of subcontinental lithosphere in magma genesis at destructive plate margins, *in* Hawksworth C.J., and Norry, M.J., eds., *Continental Basalts and Mantle Xenoliths*, p. 230-249.
- Pearce, J.A., and Cann, J.R., 1973, Tectonic setting of basic volcanic rocks determined using trace element analysis: *Earth and Planetary Science Letters*, v. 19, p. 290-300.
- Pearce, J.A., and Norry, M.L., 1979, Petrogenetic implications of Ti, Zr, Y, and Nb variations in volcanic rocks: *Contributions to Mineralogy and Petrology*, v. 69, p. 33-47.
- Poole, F.G., Perry, W.J., Jr., Madrid, R.J., and Amaya-Martinez, R., 2005, Tectonic synthesis of the Ouachita-Marathon-Sonora orogenic margin of southern Laurentia-- Stratigraphic and structural implications for timing of deformational events and plate tectonic model, *in* Anderson, T.H., Nourse, J.A., McKee, J.W., and Steiner, M.B., eds., *The Mojave-Sonora megashear hypothesis--Development, assessment, and alternatives: Geological Society of America Special Paper 393*: 543-596.
- Price, J.G., Henry, C.D., Barker, D.S., and Parker, D.F., 1987, Alkalic rocks of contrasting tectonic settings in Trans-Pecos Texas, *in* Morris, E.M., Pasteris, J.D. eds., *Mantle metasomatism and alkaline magmatism: Geological Society of America Special Paper*, 215: 335-346.
- Ross, P.-S., and White, J.D.L., 2006, Debris jets in continental phreatomagmatic volcanoes: A field study of their subterranean deposits in the Coombs Hills vent complex, Antarctica: *Journal of Volcanology and Geothermal Research*, 149: 62-84.

- Ross, P.-S., and White, J.D.L., 2012, Quantification of vesicle characteristics in some diatreme-filling deposits, and the explosivity levels of magma-water interactions within diatremes: *Journal of Volcanology and Geothermal Research*, 245-246: 55-67.
- Shepard, T.M., and Walper, J.L., 1982, Tectonic evolution of Trans-Pecos Texas: *Gulf Coast Association of Geological Societies Transactions*, 32: 165-172.
- Sheridan, M.F., and Wohletz, K.H., 1981, Hydrovolcanic explosions: The systematics of water-pyroclast equilibration: *Science*, 212: 1,387-1,389.
- Steiger, R.H., Jäger, E., 1977, Subcommittee on geochronology: Convention on the use of decay constants in geo- and cosmochronology: *Earth and Planetary Science Letters*, 36: 359-362.
- Sun, S.S., and McDonough, W.F., 1989, Chemical and isotopic systematics of oceanic basalts; implications for mantle composition and process, in Saunders, A.D., and Norry M.J., eds., *Magmatism in the Ocean Basins*, Geological Society of London Special Publications, v. 42, p. 313-345.
- Turner, K.J., Berry, M.E., Page, W.R., Lehman, T.M., Bohannon, R.G., Scott, R.B., Miggins, D.P., Budahn, J.R., Cooper, R.W., Drenth, B.J., Anderson, E.D., and Williams, V.S., 2011, *Geologic Map of Big Bend National Park, Texas*: U.S. Geological Survey Scientific Investigations Map 3142, scale 1:75,000, pamphlet 84 p.
- Valentine, G.A., 2012, Shallow plumbing systems for small-volume basaltic volcanoes, 2: Evidence from crustal xenoliths at scoria cones and maars: *Journal of Volcanology and Geothermal Research*, 223-224: 47-63.
- Valentine, G.A., and White, J.D.L., 2012, Revised conceptual model for maar-diatremes: Subsurface processes, energetics, and eruptive products: *Geology*, 40: 1,111-1,114.
- White, J.C., Benker, S.C., Ren, M., Urbanczyk, K.M., and Corrick, D.W., 2006, Petrogenesis and tectonic setting of the peralkaline Pine Canyon caldera, Trans-Pecos Texas, USA: *Lithos*, 91: 74-94.
- White, J.D.L., 1996, Impure coolants and interaction dynamics of phreatomagmatic eruptions: *Journal of Volcanology and Geothermal Research*, 74: 155-170.
- White, J.D.L., and Ross, P.-S., 2011, Maar-diatreme volcanoes: A review: *Journal of Volcanology and Geothermal Research*, 201: 1-29.
- Winchester, J.A., and Floyd, P.A., 1977, Geochemical discrimination of different magma series and their differentiation products using immobile elements: *Chemical Geology*, v. 20, p. 325-343.
- Winkler, C.E., Hanson, R.E., and Miggins, D.P., 2009, A newly discovered Eocene(?) basaltic phreatomagmatic vent complex in Big Bend National Park, Trans-Pecos Texas: *Geological Society of America Abstracts with Programs*, 41: 10-11.
- Wohletz, K., 2002, Water/magma interaction: Some theory and experiments on peperite formation: *Journal of Volcanology and Geothermal Research*, 114: 19-35.
- Wohletz, K., and Heiken, G., 1992, *Volcanology and Geothermal Energy*: Berkeley: University of California Press, 432 p.

Wohletz, K.H., and Sheridan, M.F., 1983, Hydrovolcanic explosions II. Evolution of basaltic tuff rings and tuff cones: *American Journal of Science*, 283: 385-413.

York, D., 1969, Least squares fitting of a straight line with correlated errors: *Earth and Planetary Science Letters*, 5: 320-324.

VITA

Personal

Jenni Hill
Born in Dallas, Texas

Education

Texas Christian University, Fort Worth, TX
Masters of Science in Geology, August 2014
Bachelor of Science in Geology, December 2011

Collin County Community College, McKinney, TX
Associate of Science, Associate of Arts

Experience

Urban Oil & Gas Group
Geology Intern, July 2013 - Present

TCU Geology Department, Fort Worth, TX
Teaching Assistant:
Mineralogy and Petrology Labs, August 2012 – May 2013
Introduction to Geology Lab, August 2011 – May 2012

Yale University, New Haven, CT
Paleomagnetic Laboratory Researcher, June - July 2012

Exotic Critters, Anna, TX
Exotic Animal Trainer and Caretaker, 2002 - 2009

Fieldwork

Thesis research (Texas Christian University), Big Bend National Park, TX
Fieldcamp, (Florida State University), New Mexico and Colorado

Honors and Awards

Texas Christian University Teaching Assistantship, 2011, 2012
Leroy Gideon Award for Excellence in Geology - academic achievement, 2011
Texas Christian University Scholarship - Transfer Student scholarship, 2009
National Society of Collegiate Scholars - academic achievement, 2010
Presidential Scholarship, Guilford College – academic achievement, 2009
Phi Theta Kappa - academic achievement, 2005
Collin College Dean's List - academic achievement, 2006, 2007, 2008
Collin College President's List - academic achievement, 2005, 2006, 2007

Professional Membership

Dallas Geological Society, Student Member, since 2014
American Association of Petroleum Geologists, since 2013
Geological Society of America, Student Member, since 2011

Academic Organizations

Sigma Gamma Epsilon, Texas Christian University, 2012, 2013
Geology Club, Texas Christian University, 2011

ABSTRACT

COMPLEX EOCENE-OLIGOCENE HYPABYSSAL INTRUSIVE SYSTEMS ASSOCIATED WITH BASALTIC PHREATOMAGMATIC VENTS IN THE AREA EAST OF PEÑA MOUNTAIN, BIG BEND NATIONAL PARK, WEST TEXAS

Jennifer Anne Hill, M.S., 2014
School of Geology, Energy and the Environment
Texas Christian University

Thesis Advisor: Dr. Richard Hanson, Professor of Geology

An episode of explosive Eocene basaltic phreatomagmatic volcanism has recently been discovered within the Trans-Pecos Magmatic Province in west Texas. The study area focuses on basaltic rocks formed partly during this episode east of Peña Mountain, within Big Bend National Park. Hypabyssal systems consisting of three units of diabase, Type I, II, and III, as well as outcrops of the regional Alamo Creek Basalt are present in the study area. Phreatomagmatic vent-fill outcrops are intruded by diabase and contain bombs geochemically related to the Type I intrusion and the Alamo Creek Basalt, which have $^{40}\text{Ar}/^{39}\text{Ar}$ dates of ~ 47 Ma. The Type II intrusion has not been dated, but is geochemically similar to other intrusive basalts in the region with ages of ~ 43-42 Ma. The voluminous Type III intrusion, with $^{40}\text{Ar}/^{39}\text{Ar}$ dates of ~ 34 Ma, has partly obscured the phreatomagmatic vents and was not involved in explosive volcanism.